UNIVERSITY OF CALIFORNIA,
IRVINE

Understanding the Role of the Ocean in a Changing Climate through Model Hierarchies

DISSERTATION

submitted in partial satisfaction of the requirements
for the degree of

DOCTOR OF PHILOSOPHY

in Earth System Science

by

Tien-Yiao Hsu

Dissertation Committee:
Professor Gudrun Magnusdottir, Co-Chair
Professor Francois Primeau, Co-Chair
Professor Paul Kushner

2022

DEDICATION

To my parents and sisters who give me the opportunity to explore
this amazing world, and the resources and wisdom to navigate through the unpredictable life.

To my animal friends, Fefe, Jazz, Mocha, and Peter, whose merely existence heals my broken soul.

To Gregory Kraus, who came into my life with joyful rainbows and left me with love.

To myself, who was always with me no matter it shines or storms, no matter what happened, did not happen, might have happened, and what is going to happen.

TABLE OF CONTENTS

LIST OF FIGURES

LIST OF TABLES

ACKNOWLEDGMENTS

I would like to thank Professor Gudrun Magnusdottir and Professor Francois Primeau for their input and support in the research. I also want to thank the Earth System Science's cohorts, staff members, and colleagues that effectively form a safe and open environment for me.

I want to thank my parents, sisters, and animal friends Fefe, Jazz, Mocha, and peter who support me without doubt. I also want to thank my extended family and friends across Long Beach, Orange County, and Palm Spring, including the country line dancing family, Orange County gay men's chorus family.

I want to thank my friends Carlos and Greg, Gregory Kraus, Jamie Cooper, Emilio Mozo, Erick McCray, Jessie, David Huge and Earm, Pete, Stoner Steve, Armando, Leo Tsoi, Russ, Christopher Corder and Curtis, Scott, Maxx and Day, Rovinson, Richard and Hugh, Stacey, Juliette Chu, Shih-Wei and Mark, Endora and Tony in Anchor Line (old Main Street) in Laguna Beach, I-Tsung Lu, Alf Li, Cracky Chen, Stacey, Juliette Chu.

I want to thank academic family including my cohorts (i.e. Joanna, Matt, Stanley, Hyunjin, Shane and John), Fancois Primau, Gudrun Magusdottir, Paul Kushner, Young-Oh Kwon, Shih-Wei Fang, Yu-Chiao, Yi Liu, Ting-Wei, Cameron, Elliot, Melanie, Bao, coffee hour people (especially the hosts: Marina, Megan, many others), and cleaning staffs.

I want to thank performers Endora and Tony in Anchor Line (old Main Street) in Laguna that brought so much joy for me. I want to thank Executive Suite that provides Kareoke and Country Sunday.

I want to thank Den Cafe in Costa Mesa and DTSA, Patch Coffee in Lakeforest, and Hot Java in Long Beach that provide me a place to study and do research.

I would not have survived the tough life without any of your support.

VITA

Tien-Yiao Hsu

EDUCATION

Doctor of Philosophy in Earth System Science **2022**
University of California, Irvine *Irvine, CA, United States*

Master of Science in Atmospheric Science **2015**
National Taiwan University *Taipei, Taiwan*

Bachelor of Science in Chemistry **2013**
National Taiwan University *Taipei, Taiwan*

RESEARCH EXPERIENCE

Teaching Assistant **2018–2020**
University of California, Irvine *Irvine, CA, United States*

Graduate Research Assistant **2015–2016**
National Taiwan University *Taipei, Taiwan*

TEACHING EXPERIENCE

Teaching Assistant **2009–2010**
University of California, Irvine *Irvine, CA, United States*

REFEREED JOURNAL PUBLICATIONS

A Hierarchy of Global Ocean Models Coupled to CESM1 **2022**
Journal of Advances in Modeling Earth Systems

SOFTWARE

EMOM https://github.com/meteorologytoday/EMOM
The Ekman mixed-layer model (EMOM) used in the publication.

ABSTRACT OF THE DISSERTATION

Understanding the Role of the Ocean in a Changing Climate through Model Hierarchies

By

Tien-Yiao Hsu

Doctor of Philosophy in Earth System Science

University of California, Irvine, 2022

Professor Gudrun Magnusdottir, Co-Chair
Professor Francois Primeau, Co-Chair

Due to the growing complexity of climate models, model hierarchies are becoming important in understanding climate dynamics. In this dissertation, I build two hierarchies of ocean models to study the ocean's role in a changing climate.

In chapter 2, I develop a hierarchy of simplified ocean models for the coupled ocean, atmosphere, and sea ice climate simulations using the Community Earth System Model version 1 (CESM1). The hierarchy has four members: a slab ocean model (SOM), a mixed-layer model (MLM) with entrainment and detrainment, an Ekman mixed-layer model (EMOM), and an ocean general circulation model (OGCM). Flux corrections of heat and salt are applied to the simplified models ensuring that all hierarchy members have the same climatology. I diagnose the needed flux corrections from auxiliary simulations in which I restore the temperature and salinity to the daily climatology obtained from a target CESM1 simulation. The resulting three-dimensional corrections contain the interannual variability fluxes that maintain the correct vertical gradients of temperature and salinity in the tropics. I find that the inclusion of mixed-layer entrainment and Ekman flow produces sea surface temperature and surface air temperature fields whose means and variances are progressively more similar to those produced by the target CESM1 simulation.

To illustrate the usefulness of the hierarchy, I revisit the ITCZ problem. The position of ITCZ is controlled by the interhemispheric energy imbalance. The ITCZ problem involves determining mechanisms responsible for reducing the shift of ITCZ in fully coupled climate models compared to those that couple the atmosphere to a simple SOM. In this dissertation, I tackle this problem in the context of the loss of Arctic sea ice. In the absence of dynamic ocean circulation, energy-balance considerations require the ITCZ to shift northward so that the expansion of the southern Hadley cell produces a southward energy transport. This transport eliminates the interhemispheric energy imbalance caused by the reduced northern hemisphere albedo. Two processes present in OGCMs but absent in the SOM have been proposed to explain this difference — the Atlantic meridional overturning circulation (AMOC) and the wind-driven Ekman flow. Using my hierarchy, I confirm that AMOC strongly inhibits the shift in the position of the ITCZ by producing a strong southward anomalous heat transport in the ocean. This heat transport eliminates the need for the atmosphere to respond to the interhemispheric energy imbalance.

I also show that Ekman flow does not damp the ITCZ shift as previously suggested. The explanation for this surprising result is that at the equator, the vanishing of the Coriolis parameter leads to a frictionally driven overturning cell with northward surface flow. This cell produces a northward heat transport that reinforces the interhemispheric energy imbalance, thus contradicting the original hypothesis that a northward shift of the ITCZ would drive a southward surface Ekman flow across the equator. Overall, with my hierarchy I find that it is the change in the AMOC in response to Arctic sea ice loss that is responsible for preventing the ITCZ from shifting northward.

In chapter 3, I use my hierarchy to elucidate the differing influences of Ekman and frictional flows on the deep-tropical contraction phenomenon. I study this issue in the context of the equilibrium climate response to an abrupt quadrupling of atmospheric CO_2 concentration in CESM1. I find that the atmospheric model coupled to the ocean model that includes

the dynamic Ekman flow, i.e., EMOM, can replicate the deep-tropical contraction simulated in comprehensive models. I demonstrate that the differences between atmospheric models coupled to EMOM and OGCM are due to the different penetration depth of the oceanic vertical motion and the differences in the subsurface horizontal diffusivity of temperature near the equator. Furthermore, I demonstrate that the frictional Ekman flow contributes at least 50% of the increased ocean heat convergence in the equatorial Pacific and Atlantic Oceans. This shows that the frictional flow must be included in any explanation of the deep-tropical contraction.

In chapter 4, I develop a hierarchy of intermediate meridional overturning circulation models to explore the zonal asymmetry of freshwater forcing as a stability threshold that controls the existence of multiple equilibria of the overturning circulation. I developed two new models to build a hierarchy. The first one is the zonally averaged two-slabs ocean model (ZATOM) that explicitly resolves zonal buoyancy gradients. The second one is an extension of the Stommel two-box model to include the effect zonal asymmetry of freshwater forcing. I found that the zonal asymmetry of freshwater forcing strongly determines the regimes with the multiple equilibria of the overturning circulation. I show that changing the strength of hydrological forcing has a different effect on the overturning circulation depending on zonal asymmetry of freshwater forcing. Thus, the zonal asymmetry of freshwater forcing controls the subsequent strengthening or weakening of the overturning circulation. I also use this result to explain the emergence of multiple equilibria in an oceanic general circulation model in Dijkstra and Weijer (2003).

In conclusion, I have built two hierarchies of ocean models to study the ocean's role in a changing climate. I use these hierarchies to advance our understanding of the tropical air-sea coupling and the control of zonal asymmetry of freshwater forcing on the existence of AMOC's multiple equilibria in the context of climate change.

Chapter 1

Introduction

One of the challenges of climate research is understanding how the atmospheric and oceanic circulation respond to the rapid increase of greenhouse gas that forces the ongoing global warming (e.g. B. Fox-Kemper et al., 2021). The warming has driven substantial reduction in the Arctic sea ice (Serreze and Stroeve, 2015; Andersen et al., 2020) and increase in the frequency of heavy precipitation and drought events (B. Fox-Kemper et al., 2021). Due to the complexity of the climate system, we often resort to numerical climate models to predict future climate, forming collaborative modeling projects such as the Coupled Model Intercomparison Projects (CMIPs) 1–6, Polar Amplification Model Intercomparison Project (PAMIP; Doug M Smith, Screen, et al., 2019), and Ocean Model Intercomparison Project (OMIP; Griffies et al., 2016). These projects have greatly enhanced our understanding of future climate projections. However, the simulated climate sensitivities that measure the global surface temperature response to radiative forcing have a large spread among climate models (e.g. Meehl et al., 2020; B. Fox-Kemper et al., 2021), directly impacting the assessment of future climate and climate policies.

The large intermodel spread of estimated climate sensitivities is associated with the biases

in cloud feedback (Bony et al., 2015; Zelinka et al., 2020; Myers et al., 2021). The biases, however, can be a consequence of air-sea coupling because clouds are highly interactive with the ocean. In climate simulations free of anthropogenic forcing, the double-ITCZ bias among climate models (Tian and X. Dong, 2020) is an outstanding problem that needs to be resolved. In climate simulations with increasing greenhouse emissions, the warming pattern of sea surface temperature (SST) is found to be a factor determining the climate sensitivity (e.g. Rose, Armour, et al., 2014; Y. Dong et al., 2020; Xie, 2020). The SST warming pattern can be modulated by changes in ocean circulation and ocean heat uptake (England et al., 2020). Issues where the air-sea coupling cannot be ignored in a warming climate include the shift in the intertropical convergence zone (ITCZ; e.g. Kang, Held, et al., 2008; T. Schneider et al., 2014; Tomas et al., 2016; T. Schneider, 2017; Green, J. Marshall, and Campin, 2019; S. Yu and Pritchard, 2019; Kang, 2020; Hsu et al., 2022) and the deep-tropical contraction phenomenon (e.g. Vecchi and Soden, 2007; Chemke and Polvani, 2018; Zhou et al., 2019).

Similarly, the Atlantic meridional overturning circulation (AMOC) has many aspects that contribute to the large intermodel spread of the climate sensitivity through its significant heat transport (Trenberth and Fasullo, 2017) and ability to take up the heat (Kostov et al., 2014; D. P. Marshall and Zanna, 2014; Trenberth, Fasullo, and Balmaseda, 2014; Von Schuckmann et al., 2016; Lewis and Curry, 2018; Hu et al., 2020). First, the strength and temporal variability of AMOC have large intermodel spreads among climate models (Weijer, Cheng, Garuba, et al., 2020). Second, the existence of tipping points of AMOC to produce a catastrophic shutdown in climate models remains undetermined (Weijer, Cheng, Drijfhout, et al., 2019). Therefore, we cannot fully trust the simulated AMOC heat transport in a warming climate. These uncertainties eventually propagate to the discrepancy in climate sensitivities among climate models.

There are some notable techniques that can extract physical information from intermodel spreads. These include the intermodel empirical orthogonal function (IEOF) analysis (e.g.

Li and Xie, 2012; Huang and Ying, 2015) and emergent constraint (e.g. P. M. Cox et al., 2018; Thackeray and Hall, 2019; Doug M Smith, Eade, et al., 2022). These techniques have successfully determined the scientific focus with the existing simulations. However, while the realism of physical processes in climate models has increased significantly, the growing complexity of interactions in the models obscures the underlying mechanisms, preventing us from fully understanding the simulated climate. At the same time, as newer climate models with higher resolution are developed, the increasing computational cost outpaces our ability to perform a large number of simulations, further limiting us from determining the robustness of future climate projections.

The framework of model hierarchies is ideal for developing an understanding of the mechanisms that produce climate phenomena (Claussen et al., 2002; Held, 2005; Jeevanjee et al., 2017; G. K. Vallis et al., 2018; Maher et al., 2019, e.g.). In particular, model hierarchies that progressively include physical processes allow us to better understand the climate mechanisms and to determine the robustness of climate projections. They isolate the effects of particular processes, allowing us to gain physical understanding by varying the model complexity. Additionally, the simpler models at the base of the the hierarchy are typically computationally cheaper than comprehensive models, allowing us to perform more ensemble simulations to determine the robustness of the outcome.

Here I illustrate how model hierarchies help enhance the physical understanding of the ITCZ shift problem mentioned above (e.g. Kang, 2020; Hsu et al., 2022). The latitudinal location of ITCZ is sensitive to interhemispheric imbalance because its location determines the cross-equatorial energy transport in the atmosphere that should compensate non-zero energy budget in equilibrium (T. Schneider et al., 2014), which neatly explains the northward ITCZ shift in response to the forced Arctic warming in atmosphere models coupled to an SOM (Kang, Held, et al., 2008). However, the participation of the ocean processes damps the extent of the shifting (Tomas et al., 2016). The modulation may come from the wind-driven

Ekman heat transport (Green and J. Marshall, 2017; T. Schneider, 2017), the AMOC (Chiang and Bitz, 2005; S. Yu and Pritchard, 2019), or both (Green, J. Marshall, and Campin, 2019). Very often, these processes are entangled in comprehensive models, so it is hard to isolate their independent contribution. Thus in chapter 2, I construct a new hierarchy that can isolate the effect of wind-driven Ekman flow, which further indirectly allows me to isolate the effect of AMOC. Through this hierarchy, I confirm the importance of AMOC in damping the ITCZ shift. Surprisingly, through this hierarchy I also show that the wind-driven Ekman flow does not damp the ITCZ shift as previously suggested. Instead, the hierarchy shows an important role of wind-driven frictional flows that amplifies the cross-equatorial ocean heat transport. We further find that the convergence of ocean heat transport associated with frictional Ekman flow has a large contribution to the deep-tropical contraction in the quadrupling CO_2 simulations. While detailed discussions are documented in chapters 2 and 3, an important message here is that model hierarchies can test proposed dynamics and trigger new scientific ideas.

Model hierarchies can also help us bridge the gaps in the physical understanding between simple conceptual ideas and their realism in comprehensive models. The example here is the problem in regards to determining the existence of multiple equilibria of AMOC in climate models, as briefly mentioned in earlier text (see Weijer, Cheng, Drijfhout, et al., 2019, for comprehensive reviews). Among many possible aspects, a fundamental gap is that the dynamics of meridional overturning circulation is three-dimensional while most of our scientific discussion and elaborations are in the context of two-dimensional models (Jochem Marotzke et al., 1988; Stocker et al., 1992; Vellinga, 1996), or even simply Stommel two-box model (Stommel, 1961). How these discussions in lower degrees of freedom system are related back to comprehensive ocean models is unclear. Because of this distinct gap, the construction of an intermediate model by Callies and Marotzke (2012) is an important development because this model resolves the coarse zonal structure of the overturning circulation. In chapter 4, I construct a hierarchy of ocean models by including two extended models based on

Callies and Marotzke (2012) and Stommel two-box model. By showing similarities between regimes with multiple equilibria of each hierarchy member, I conclude that these models share the same physics to produce the multiple equilibria of the overturning circulation. Moreover, I find that the zonal asymmetry of freshwater forcing has a fundamental role in controlling where in parameter space we have regime with multiple equilibria. I also find that this qualitative result can explain the bifurcation diagram constructed by Dijkstra and Weijer (2003) in which they discussed the emergence of the multiple equilibria of AMOC under various strengths of background hydrological forcing. Most importantly, I want to point out that the ability to verify a physical idea across model complexity is another important function of model hierarchies.

The usage of model hierarchies has grown since Held (2005) was published. Recently, the Model Hierarchy Workshop, so far has been held in 2016 and 2022, is a community effort to advocate the usage of model hierarchies in climate studies. The ongoing development of Community Earth System Model version 3 (CESM3) will also provide various models with different model complexity to lower the threshold of using model hierarchies. Therefore, my dissertation can be seen as a scientific creation aligned with these efforts.

Chapter 2

A Hierarchy of Global Ocean Models Coupled to CESM1

2.1 Motivation

Model hierarchies contribute to improved understanding of the climate response to external forcing by isolating the influence of various physical processes (e.g., Claussen et al., 2002; Held, 2005; Jeevanjee et al., 2017; G. K. Vallis et al., 2018; Maher et al., 2019). Simplified global ocean models that have been used to study the climate system consist of models with mixed-layer acting independently in each water columns (e.g., David et al., 1999; Dommenget and Latif, 2002; Cassou et al., 2007; Hirons et al., 2015) and models with Ekman flows coupling the water columns (Codron, 2012). With the exception of Hirons et al. (2015), all these models used a strong-restoring to a reference temperature and salinity profile with a timescale of less than 20 years to achieve a realistic climate state. As such, these models can be used to study high-frequency climate variability, but not variability on decadal and longer time scales. The mixed-layer model developed by Hirons et al. (2015) is exceptional because

it avoids the weak-restoring term by prescribing a three-dimensional time-dependent flux correction. This has the advantage of not damping the low-frequency variability. We build on these previous studies by formulating an ocean model that includes a mixed-layer and Ekman flow. We adopt the strategy of Hirons et al. (2015) by prescribing a three-dimensional time-dependent flux correction to achieve a target climate. We include weak-restoring terms to the temperature and salinity equations, but we choose a restoring time scale of 100 year so that we can study decadal climate variability. Furthermore, by switching off particular processes, this model can form an ocean-model hierarchy to complement the ocean general circulation model (OGCM) in the Community Earth System Model version 1 (CESM1; Hurrell et al., 2013). This hierarchy can be applied to study climate response to external forcing such as Arctic sea-ice loss or an increase in greenhouse gas.

Simplifications of ocean processes in climate models for studies that focus primarily on the atmosphere response to external forcing typically consist of the following options: (i) prescribing the sea surface temperature (SST) (e.g., Magnusdottir and Saravannan, 1999), (ii) a single, static layer, known as a slab ocean model (SOM), that can take up heat from the atmosphere, store it, and release it back to the atmosphere (e.g., Kiehl et al., 2006), and (iii) a full OGCM (e.g., POP2; R. Smith et al., 2010). Unlike option (i), the SOM accounts for the finite thermal inertia of the upper ocean. The OGCM, in turn, accounts for the three-dimensional transport of heat by ocean currents that respond dynamically to surface fluxes of heat, freshwater, and momentum. Because the gap between options (ii) and (iii) is decidedly large, our goal is to formulate two simplified ocean models that narrow the gap between the SOM and the OGCM.

The first model beyond the SOM is the mixed-layer model. We construct it by diagnosing the time-dependent mixed-layer thickness from a climate simulation using the OGCM. Then, we prescribe high vertical diffusivity above the base of the diagnosed mixed-layer. This time-dependence, which we diagnose from the climatological seasonal cycle in a climate simulation

using the OGCM, allows the model to store heat anomalies in the seasonal thermocline where they can be re-entrained into the mixed-layer in the following year which is called the re-emergence mechanism. The re-emergence of these heat anomalies creates winter-to-winter SST correlations that are particularly important in the North Atlantic and North Pacific Oceans. The re-emergence mechanism primarily operates on interannual timescale and has the potential to influence the Pacific Decadal Oscillation (PDO) (M. A. Alexander and Clara Deser, 1995; M. A. Alexander, Clara Deser, and Timlin, 1999; M. A. Alexander, Scott, and Clara Deser, 2000; N. Schneider and Cornuelle, 2005; Kwon et al., 2011; M. Newman et al., 2016).

In the second model, we add dynamic wind-driven Ekman flows to the previously added time dependence of the mixed-layer depth. The upwelling and downwelling generated by the divergence of these flows provide an additional pathway for the atmosphere to interact with the subsurface ocean. In addition, the Ekman flows contribute to the horizontal transport of heat, which is particularly important in the tropical ocean where it dominates the oceanic heat transport (OHT) (Lee and Jochem Marotzke, 1998; Held, 2001). The response of Ekman OHT to changes in surface winds has been shown to be particularly important for damping shifts of the Inter-tropical Convergence Zone (ITCZ) when the Earth is forced with an extra-tropical thermal forcing (Green and J. Marshall, 2017; T. Schneider, 2017; Kang, Y. Shin, and Codron, 2018; Kang, Y. Shin, and Xie, 2018; Green, J. Marshall, and Campin, 2019).

Despite the relative simplicity of our two new models, we need to address several complications: (i) The linear momentum balance equations used to compute the Ekman flows are singular at the equator. To eliminate the singularity we introduce a Rayleigh friction term. Choosing an appropriate value for the friction coefficient is the first complication. (ii) The simplified model with Ekman flow produces a pronounced equatorial rainfall anomaly that originates from a runaway coupled mode along the equator that needs to be damped using

an explicit horizontal eddy diffusivity (a mechanistic explanation for this coupled mode is provided in Section 2.2.6). Choosing an appropriate value for this lateral diffusivity is the second complication that we must address. (3) Finally, because the simplified models neglect many oceanic processes that influence the exchange of heat between the atmosphere and ocean, we need to include prescribed fluxes of heat and moisture in our simplified ocean models to prevent the coupled climate from drifting to unrealistic states. Diagnosing these fluxes is the third complication. We address these complications in Section 2.

In this paper, we illustrate the use of the hierarchy by studying the importance of different ocean processes in the response of the climate system to the loss of Arctic sea-ice. Many factors can influence the response, including the background state, wave mean flow interactions in the atmosphere, sea-ice physics, and the exchange of heat with the ocean (, and references therein Blackport and Kushner, 2018; Screen et al., 2018; Sun, M. Alexander, et al., 2018; D. M. Smith et al., 2022). Of particular importance for motivating our work is the study of Tomas et al. (2016) that identified the importance of oceanic heat transport for modulating the response of the atmosphere to sea ice loss by comparing simulations performed with an OGCM to simulations with an SOM.

The paper is structured as follows: In Section 2.2, we introduce the model formulation and solutions to the challenges described above. In Section 2.3, we investigate the modulating effect of ocean processes on (i) climate variability and (ii) the atmospheric response to the loss of Arctic sea ice. In Section 2.4, we present concluding remarks.

2.2 Methods

2.2.1 Hierarchy of ocean models within CESM1

Our hierarchy of climate models is constructed using the Community Earth System Model version 1 (CESM1; Hurrell et al., 2013) by replacing, the standard Parallel Ocean Program version 2 (POP2, henceforth OGCM; R. Smith et al., 2010; Gokhan Danabasoglu et al., 2012), in turn with three simplified ocean models. These simplified ocean models, which are generated from a unified numerical code written in Julia (https://github.com/meteorologytoday/EMOM), consist of a SOM, a mixed-layer model (MLM), and an Ekman mixed-layer ocean model (EMOM). A Julia interface exchanges the surface fluxes with the Fortran CESM1 coupler.

The other components of the climate model consist of the Community Atmosphere Model version 4 (CAM4; Neale et al., 2013), the Los Alamos Sea Ice Model version 4 (Hunke et al., 2010), Community Land Model version 4 (D. M. Lawrence et al., 2011), and the River Transport Model (as part of Community Land Model). This configuration of the climate model is equivalent to the Community Climate System Model 4 (CCSM4; P. R. Gent, Gokhan Danabasoglu, et al., 2011).

All the simulations are run with nominally $1^\circ \times 1^\circ$ horizontal resolution: The atmosphere and land models have 192 and 288 points in latitude and longitude on a Gaussian grid (also termed f09 in CESM1). The ocean and sea-ice models have 384 and 320 points in latitude and longitude with a displaced-pole grid (also termed g16 in CESM1).

2.2.2 Oceanic general circulation model (OGCM)

The Parallel Ocean Program version 2 (POP2) used in our study has a nominal horizontal resolution of about $1^\circ \times 1^\circ$. However, the meridional resolution between 10°S and 10°N — the range within which ITCZ shifts occur — is better than 0.27° of latitude. Furthermore, the grid's "North Pole" is displaced to sit in Greenland, thus avoiding any polar coordinate singularity in the ocean (R. Smith et al., 2010). In the vertical, the model has 60 levels with separation ranging from 10 m in the top 160 m of the water column, increasing monotonically from 10m to 250 m in the depth range between 160 m, and 3500 m, and is fixed at 250 m down to the maximum ocean depth of 5500 m. The model's mixed-layer dynamics are governed by the K-profile parameterization (KPP) vertical-mixing scheme (Large et al., 1994). The model also uses the P. R. Gent and McWilliams (1990) isopycnal mixing scheme.

2.2.3 Ekman mixed-layer ocean model (EMOM)

The unified code for our hierarchy of simplified ocean models is called EMOM. We show the physical processes that are represented by EMOM in schematic form in Figure 2.1. EMOM is coupled to the other climate model components through the CESM coupler. EMOM has 33 vertical layers identical to the top 33 layers of the POP2 configuration. These 33 layers cover a total depth ≈ 503.7 m and range in thickness from 10 m to 48 m. EMOM solves the following equations governing the time-evolution of temperature, T, and salinity, S,

$$\frac{\partial T}{\partial t} + \vec{\mathbf{v}}_H \cdot \nabla_H T + w\frac{\partial T}{\partial z} = \frac{\partial}{\partial z}\left(K_V \frac{\partial T}{\partial z}\right) + \nabla_H \cdot (K_H \nabla_H T) - \frac{1}{\rho c_p}\frac{\partial F_T}{\partial z} - \frac{1}{t_R}(T - T_{\text{clim}}) - \frac{\Lambda}{\tau_{\text{FRZ}}}(T - T_{\text{FRZ}}) + \frac{Q_T}{\rho c_p}, \tag{2.1a}$$

$$\frac{\partial S}{\partial t} + \vec{\mathbf{v}}_H \cdot \nabla_H S + w\frac{\partial S}{\partial z} = \frac{\partial}{\partial z}\left(K_V \frac{\partial S}{\partial z}\right) + \nabla_H \cdot (K_H \nabla_H S) - \frac{\partial F_S}{\partial z} - \frac{1}{t_R}(S - S_{\text{clim}}) + Q_S, \tag{2.1b}$$

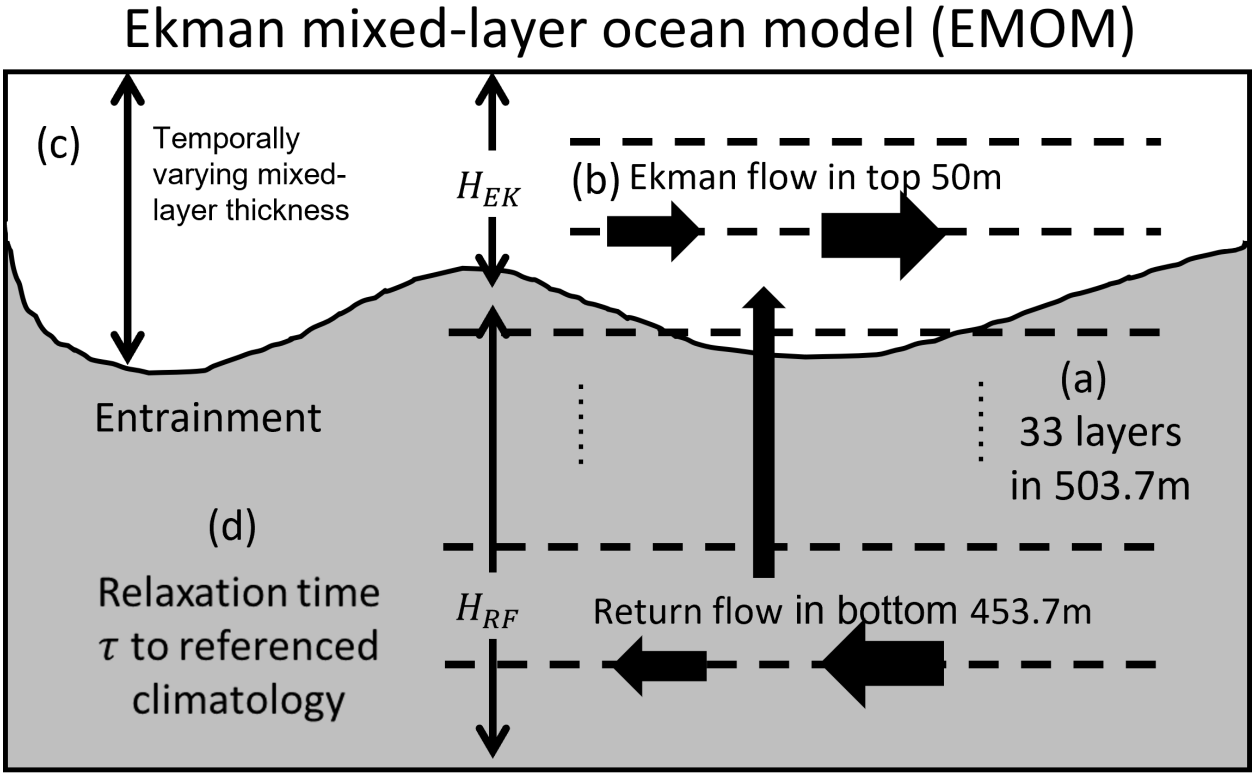

Figure 2.1: Schematic diagram of EMOM architecture. (a) EMOM has 33 vertical layers whose total depth is ≈ 503.7 m and range in thickness from 10 m to 48 m. (b) The Ekman and return flow layers have thicknesses of 50 m and 453.7 m. (c) EMOM has a time-varying mixed-layer thickness to capture the effect of seasonal entrainment and detrainment. (d) The ocean temperature and salinity are relaxed toward a reference three-dimensional profile with a 100-year timescale.

where $\rho = 1026$ kg/m^3 and $c_p = 3996$ J/K/kg are the density and heat capacity of seawater, F_T is the energy flux consisting of radiation, sensible, and latent heat fluxes, F_S is the virtual salt flux to account for evaporation minus precipitation, runoff, sea-ice melting and brine injection, $\vec{\mathbf{v}}_H$ is the horizontal velocity, w is the vertical velocity component, Q_T and Q_S are heat and salt flux correction terms, ∇_H is the horizontal gradient or divergence operator, K_H is the horizontal diffusivity. K_H depends on latitude according to

$$K_H = K_0 + (K_1 - K_0) \exp\left(-\frac{\phi^2}{2\sigma_K^2}\right) \exp\left(\frac{z}{H_K}\right) \tag{2.2}$$

with ϕ is the latitude in radians, $K_0 = 5.0 \times 10^3$ m^2/s, $K_1 = 2 \times 10^4$ m^2/s, $\sigma_K = 2\pi/36$ $(= 10^\circ)$ and $H_K = 100$ m. The value of K_0 is referenced from Nummelin et al. (2021) in which the SST diffusivity is diagnosed (see their Figure 2). The values of K_1 and σ_K are chosen to prevent the spurious rainfall pattern mentioned in the introduction and further discussed in Section 2.2.6. K_V is the vertical diffusivity that depends on the mixed-layer thickness h and vertical gradient of buoyancy, b. Explicitly,

$$K_V = \begin{cases} 1 \text{ m}^2/\text{s} & \text{if } -h < z < 0 \text{ or } \frac{\partial b}{\partial z} < 0, \\ 1 \times 10^{-4} \text{ m}^2/\text{s}, & \text{otherwise.} \end{cases} \tag{2.3}$$

The short-wave radiative heating is divided into two components and each follows an exponential depth profile with a constant e-folding depth. The parameters are selected according to Type I water in Table 2 of Paulson and Simpson (1977). The remaining surface heat fluxes and virtual salt fluxes are implemented as interior sources in the top 10-meter-thick layer of the model so that Equations (2.1a) and (2.1b) can be solved subject to no-flux boundary conditions.

To compute the buoyancy, we approximate the density using a third-order polynomial approximation for the equation of state as described in K. Bryan and M. D. Cox (1972). In the numerical implementation, K_V is specified at the interface between the grid boxes. The

effective mixed-layer thickness must therefore coincide with the discrete depths of the interfaces between the grid boxes. T_{clim} and S_{clim} are the 50-year reference monthly climatological profiles that the entire ocean is weakly restored to with a timescale $t_R = 100$ years. With this choice of t_R, we refer to this term as the "weak-restoring" term. To take into account the latent heat exchanges associated with the transformation of water between the liquid and solid phases, we introduce the parameters $\tau_{\text{FRZ}} = 1\,\text{day}$ and $T_{\text{FRZ}} = -1.8°\text{C}$ as the freezing timescale and freezing point of ocean water. Λ is the Heavyside step function, i.e.,

$$\Lambda = \begin{cases} 1 & \text{if } T < T_{\text{FRZ}}, \\ 0 & \text{otherwise.} \end{cases}$$

This design switches on the freezing process so that ocean temperature is forced to be above the freezing point. The latent heat released is sent to the coupler so that sea ice may grow. For simplicity, we prescribe the space and time dependence of h. We considered adopting a dynamic mixing layer model such as the KPP scheme (Large et al., 1994) as used in the POP2 model or a Niiler-Kraus type bulk formulation (Niiler, 1977; Gaspar, 1988). However, the former needs as input the vertical sheer, which is not available in our simplified model, and the latter, which we implemented and tested, produces a mean mixed-layer thickness that is substantially different than the one in the parent simulation. This difference in the mean state complicates the interpretation of our experiments. For these reasons, we focus here on the simplified models with a prescribed time-dependence for the mixed-layer thickness.

As for the velocity field, we use the same formulation as Codron (2012) in which the Ekman velocity is assumed uniform within the Ekman layer and is diagnosed from the instantaneous wind-stress using a linear momentum balance:

$$\vec{\mathbf{v}}_{\text{EK}} = \frac{1}{\rho H_{\text{EK}}(\epsilon^2 + f^2)} \left(f\tau^y + \epsilon\tau^x, -f\tau^x + \epsilon\tau^y \right) \tag{2.4}$$

where $H_{\text{EK}} = 50\,\text{m}$ is the Ekman layer thickness, f the latitude-dependent Coriolis param-

eter, and $\vec{\boldsymbol{\tau}} = (\tau^x, \tau^y)$ is the surface wind stress, ϵ the Rayleigh friction coefficient that removes the signularity of Ekman solution at the equator. The Ekman layer whose thickness varies spatially does not coincide with mixed layer. Two possible choices for the Ekman thickness are the Laminar and turbulent Ekman length scales given by $\sqrt{2\nu/f}$ and u^*/f, respectively, where ν is the momentum diffusivity and u^* is the frictional velocity (Deusebio et al., 2014). However, neither of these choices is appropriate for equatorial regions because of the singularity at the equator. For simplicity, we choose a constant Ekman layer thickness. The value of ϵ is set to $\epsilon = 1.4 \times 10^{-5}$ s^{-1} (see Section 2.2.4 for detail) so that the Rayleigh friction dominates over the Coriolis force in a narrow band between 5.5°S and 5.5°N. At the equator $\vec{\mathbf{v}}_{\mathrm{EK}}$ becomes aligned with the direction of surface wind stress. We will call the part of $\vec{\mathbf{v}}_{\mathrm{EK}}$ that is proportional to $\epsilon\vec{\tau}$ the frictional Ekman flow.

Two alternative parameterizations have been proposed for removing equatorial Ekman-balance singularity. In terms of the cross-equatorial ocean heat transport, these parameterizations produce a better agreement between the OGCM and the simplified ocean model. However, there are other problems with these alternative parameterizations. The parameterization of Kang, Y. Shin, and Codron (2018) drops the ϵ term in the numerator of the second component of Equation (2.4). Unfortunately, this simplification cannot be justified from the original momentum equation. In order to drop the ϵ dependence in the numerator of the meridional component of Equation (2.4), the Rayleigh friction term in the zonal momentum equation must vanish, but without it, the zonal component of Equation (2.4) would still be singular at the equator. Afargan-Gerstman and Adam (2020) proposed a parameterization in the context of an aqua-planet simulation where the zonal symmetry causes the mean meridional wind component to vanish so that only the meridional Ekman flow needs to be considered. For this special case, the Ekman-balance singularity can be eliminated by retaining the latitudinal-dependence of the Coriolis parameter, i.e. the β effect, and noting that in the absence of friction the meridional Ekman flow is proportional to the curl of the wind stress divided by β. No such balance is available for the zonal Ekman flow, which will still

be singular if it is present. Because we are considering a realistic continental configuration, we decided to adopt Codron's original formulation, i.e. Equation (2.4).

As in Codron (2012), we assume that (i) the return flow occurs directly below the Ekman layer, (ii) the return flow is uniformly distributed in a layer of constant thickness, and (iii) there is no accumulation of water mass in any water column. Therefore, the resulting return flow is given as

$$\vec{\mathbf{v}}_{\mathrm{RF}} = -\frac{H_{\mathrm{EK}}}{H_{\mathrm{RF}}}\vec{\mathbf{v}}_{\mathrm{EK}}, \tag{2.5}$$

where $H_{\mathrm{RF}} \approx 453.7\,\mathrm{m}$ is the thickness of the return flow so that the resulting thickness conveniently coincides with OGCM grid. Thus, the horizontal velocity is $\vec{\mathbf{v}}_{\mathrm{EK}}$ $z \in (-H_{\mathrm{EK}},0]$ and $\vec{\mathbf{v}}_{\mathrm{RF}}$ for $z \in (-(H_{\mathrm{EK}}+H_{\mathrm{RF}}), -H_{\mathrm{EK}}]$. We acknowledge the ad-hoc nature of the formulation of the return flow. Its virtue is that it is easily implemented and its use has precedence in the work of Codron (2012).

The resulting Ekman OHT is easy to diagnose given the temperature profile in each water column. For any given water column, Ekman OHT is given by

$$\begin{aligned}
\mathrm{OHT}_{\mathrm{EK}} &= \rho_0 c_p \int_{z=-(H_{\mathrm{EK}}+H_{\mathrm{RF}})}^{0} v_{\mathrm{EK}} T \,\mathrm{d}z \\
&= \rho_0 c_p \left(H_{\mathrm{EK}} v_{\mathrm{EK}} T_{\mathrm{EK}} + H_{\mathrm{RF}} v_{\mathrm{RF}} T_{\mathrm{RF}}\right) \\
&= c_p \Delta T \left(\frac{-f\tau^x + \epsilon\tau^y}{\epsilon^2 + f^2}\right)
\end{aligned} \tag{2.6}$$

where

$$T_{\mathrm{EK}} = \frac{1}{H_{\mathrm{EK}}}\int_{-H_{\mathrm{EK}}}^{0} T\,\mathrm{d}z, \text{ and } \quad T_{\mathrm{RF}} = \frac{1}{H_{\mathrm{RF}}}\int_{-(H_{\mathrm{EK}}+H_{\mathrm{RF}})}^{-H_{\mathrm{EK}}} T\,\mathrm{d}z \tag{2.7}$$

are the mean temperatures over the Ekman and return-flow layers, and

$$\Delta T \equiv T_{\mathrm{EK}} - T_{\mathrm{RF}} \tag{2.8}$$

is the difference between the mean temperatures defined above. In going from the second to the third line of Equation (2.6), we used Equation (2.5). Given typical tropical wind stress $(\tau^x, \tau^y) = (0.01, 0)\mathrm{N/m}^2$ at latitude 5.5°N where $\epsilon = f$ (Section 2.4 shows how we pick ϵ), the computed zonally integrated ($2\pi \cos 5.5° \times$ (Radius of earth) $\approx 4 \times 10^7$m) meridional OHT is about 0.06 PW per °C change of ΔT.

EMOM is discretized using Arakawa C-grid. The model exchanges surface fluxes with the atmosphere every 24 hours. The time step is set to three hours. Advection and horizontal diffusion are implemented using the QUICKEST scheme (upwind, second-order accuracy; Leonard, 1979). Finally, the vertical diffusion, weak-storing, and freezing process are solved using the implicit Euler backward method.

All the members of our hierarchy except for the OGCM can be recovered from the same code base. To recover the MLM, we simply set $\vec{\mathbf{v}} = 0$. To recover the SOM, we (i) set $\vec{\mathbf{v}}_H = \mathbf{0}$, (ii) set the mixed-layer thickness of each grid point to its time-averaged value, and (iii) replace the topography mask to match the time-averaged mixed-layer thickness. With these settings, $w_e = 0$ and $K_v = 1$ m^2/s everywhere, which makes our model equivalent to a well-mixed slab.

There are three major differences between CESM1-SOM and our SOM. First, CESM1-SOM sets the horizontal diffusivity K_H to zero while our SOM has non-zero spatially varying K_H given by Equation (2.2). This choice simplifies the task of comparing the output of the different models of our hierarchy. Second, the CESM1-SOM uses the boundary layer depth output from POP2 (variable `HBLT`) instead of mixed-layer depth (variable `HMXL`), which we use in EMOM, for the mixed-layer thickness. The boundary layer depth and the mixed-

layer thickness are equal when they are at their maximum, but otherwise the boundary layer is thinner than the mixed-layer. Past studies have shown that a shallower annual-mean mixed-layer thickness leads to colder SSTs, which tends to increase the albedo through cloud-radiative feedback processes (Donohoe et al., 2014; Zaiyu Wang et al., 2019). However, the flux corrections that are applied to our simplified models will generally eliminate this effect on the mean climate. The choice of thickness would most likely also affect the climate variability, but the above mentioned studies do not offer any specific recommendation as to which choice is preferable in a SOM. We, therefore, chose to set h to `HMXL`. Third, in CESM-SOM, the prescribed ocean velocity derived from the referenced OGCM is sent to the coupler. In our SOM, we set the ocean velocity sent to the coupler to be zero in SOM (also MLM and EMOM) to simplify the dynamics. Thus, the rates of heat and momentum exchanges between air-sea and ocean-sea-ice interface are different between CESM-SOM and SOM.

The full OGCM completes our hierarchy as the most realistic ocean model. Thus, the resulting hierarchy of ocean models from simplest to most complex are: the SOM, the MLM, the EMOM, and the OGCM. As we progress up the hierarchy the MLM includes entrainment, which is absent in the SOM, the EMOM includes Ekman transport, which is absent in the MLM and the OGCM includes everything else (i.e. gyres, overturning circulation, waves, etc.)

2.2.4 Estimation of Rayleigh Friction ϵ in Equation (2.4)

To avoid the singularity of the Ekman flow solution at the equator, we introduced a Rayleigh friction term in the horizontal momentum equations used to derive Equation (2.4). To determined the value of ϵ, we minimized the sum of the squared differences between the vertical velocities computed by the OGCM and those computed from the divergence of

$\vec{\mathbf{v}}_{\mathrm{EK}}(\epsilon)$ integrated from the surface, assumed flat and rigid, down to a depth of $H = 50$ m in the latitude band between 10°S–10°N. Explicitly,

$$\epsilon = \underset{\epsilon}{\operatorname{argmin}} \sum_{i \in \mathcal{X}} \left| w^i_{\mathrm{OGCM}} - w^i_{\mathrm{EK}}(\epsilon) \right|^2 \tag{2.9}$$

where

$$w^i_{\mathrm{EK}}(\epsilon) = H \nabla \cdot \vec{\mathbf{v}}_{\mathrm{EK}}(\epsilon), \tag{2.10}$$

and $\mathcal{X}$ denotes the set of mesh points between 10°S and 10°N.

The solution to the above non-linear least-squares problem yielded a value of $\epsilon = 1.4 \times 10^{-5}$ s^{-1}. With this choice for ϵ, Rayleigh friction dominates over the Coriolis force between 5.5°S–5.5°N. Thus within 5° of the equator, the Ekman flow is more parallel than perpendicular to the direction of the wind stress. At the equator, the Ekman flow is exactly aligned with the wind stress.

2.2.5 Derivation of correction flux

For the simulations that use SOM, MLM, and EMOM, we apply flux corrections to force the simulated climates towards the one simulated using CESM1 (i.e. CTL_OGCM; see Section 2.2.7). The flux corrections make up for the mean heat and freshwater transports captured by the full OGCM but not explicitly represented in our simplified models. These flux corrections include rectification effects due to interannual variability. For example, if we decompose the variables in Equation (2.1a) into a mean annual cycle plus anomaly, i.e. $(\,\cdot\,) = \overline{(\,\cdot\,)} + (\,\cdot\,)'$,

and then apply the averaging operator $\overline{(\cdot)}$, we obtain

$$\frac{\partial \overline{T}}{\partial t} + \overline{\vec{\mathbf{v}}}_{\mathrm{EK}} \cdot \nabla_H \overline{T} + \overline{w}_{\mathrm{EK}} \frac{\partial \overline{T}}{\partial z} = \frac{\partial}{\partial z}\left(K_V \frac{\partial \overline{T}}{\partial z}\right) + \nabla_H \cdot \left(K_H \nabla_H \overline{T}\right) - \frac{1}{\rho c_p}\frac{\partial \overline{F}_T}{\partial z} - \frac{1}{t_R}\left(\overline{T} - T_{\mathrm{clim}}\right)$$
$$-\frac{\overline{\Lambda}}{\tau_{\mathrm{FRZ}}}\left(\overline{T} - T_{\mathrm{FRZ}}\right) + \left[\frac{\overline{Q}_T}{\rho c_p} - \overline{\vec{\mathbf{v}}'_{\mathrm{EK}} \cdot \nabla_H T'} - \overline{w'_{\mathrm{EK}} \frac{\partial T'}{\partial z}} + \overline{K'_V \frac{\partial^2 T'}{\partial z^2}} - \frac{\overline{\Lambda' T'}}{\tau_{\mathrm{FRZ}}}\right]. \tag{2.11}$$

The terms in the square bracket correspond the flux corrections needed to reproduce the mean annual cycle. In addition to the effect of missing processes, $\overline{Q_T}$, the bracket includes anomaly-product terms. Some of the interannual variability that produces the anomalies that contribute to these product terms will be generated spontaneously by the simplified models. Their effects do not need to be included in the flux correction. However, some of the interannual anomalies originate from processes that can only be simulated using the full OGCM and will, therefore, be absent in our simplified climate models. As a prominent example, the El Niño-Southern Oscillation (ENSO), which dominates in the tropics, cannot be captured in our simplified models. Its effect on the annual mean fluxes must be included as part of the flux correction. Without it, our models cannot reproduce the correct vertical temperature gradient. There is, however, a potential risk of double-counting the effect of anomalies that can be simulated in the simplified coupled climate models.

To derive the flux correction given by the terms in the square bracket of Equation (2.11), we first use the 50-year daily climatology of temperature and salinity (T_{clim} and S_{clim}) from the end of a 1000-year spin-up run of the OGCM. Then, for each model, we temporarily set $t_R = 15\,\mathrm{days}$ in the simplified model and run the resulting coupled climate model for 20 years. We then record the monthly mean values of the restoring term for the last 19 years. Finally, we average each month to produce a three-dimensional flux correction that is periodic with a period of one year.

2.2.6 Importance of large K_H near the equator

Without explicit horizontal diffusion, EMOM produces a persistent band of excessively strong equatorial precipitation in the Central Pacific (Figure S1a, 150-170°W with the zonal mean shown in Figure S1b).

In a narrow band along the equator where the frictional force dominates over the Coriolis, convergent surface winds (Figure S1b, red dashed line) above a warm SST anomaly (Figure S1c, black solid line) also drive convergent ocean currents that suppress upwelling (Figure S1c, red dashed line). Off the equator, where the Coriolis force dominates over the friction force the wind-driven currents are divergent and drive upwelling. Further examination of the meridional wind stress τ^y and ocean 50-m vertical velocity $w_{50\mathrm{m}}$ reveals that this is a consequence of the following coupled positive feedback. Since our Rayleigh friction dominates over the Coriolis force within 5.5° of the equator, anomalous wind convergence drive anomalous SST convergence near the equator. The resulting warming of the sea surface acts to reinforce the convection in the overlying atmosphere. Furthermore, the upwelling of cold waters in regions straddling the center of atmospheric convection induces locally descending motion in the atmosphere, which acts to further reinforce the the convergent winds and atmospheric convection.

In the real ocean, the generation of the strong temperature gradients seen in Figure S1c would lead to a baroclinic instability that would generate a vigorous eddy field. The diffusive fluxes generated by these eddies would come to balance the advective flux due to the mean flow. By positing a balance between the advective and diffusive fluxes, we can estimate an appropriate value of K_H so that we can suppress the spurious rain band in EMOM,

$$K_H \frac{\partial^2 T}{\partial y^2} = -v \frac{\partial T}{\partial y} \tag{2.12}$$

$$\Rightarrow K_H \approx |v \Delta y| \tag{2.13}$$

where Δy is the meridional length scale. From Figure S1 we estimate that $\Delta y \approx 400\,\mathrm{km}$, and that the maximum meridional ocean Ekman flow is about $\max(|\tau^y|)/(\rho_0 \epsilon\, 50\,\mathrm{m}) \approx 0.028\,\mathrm{m\,/\,s}$. From these scales, we estimate $K_H = |v\Delta y| = 1.12 \times 10^4\,\mathrm{m^2\,/\,s}$. Thus, to ensure the suppression of coupled positive feedback, we set K_1 in Equation (2.2) to be $2 \times 10^4\,\mathrm{m^2\,/\,s}$.

2.2.7 Simulation design

Since we want to test how ocean processes modulate climate variability and the response to Arctic sea-ice loss, it is necessary to have a set of control runs where all hierarchy members produce the same climate.

The control runs are initialized with the January-mean fields from the end of the 1000-year spin-up simulation of the full OGCM. They are performed with the necessary correction fluxes derived in Section 2.2.5 and are labeled as CTL_[MODEL] where [MODEL] can be one of SOM, MLM, EMOM, or OGCM. The CTL simulations are run for 120 years and the last 100 years are analyzed. The biases of each model are defined as the deviations from the CTL_OGCM simulation as opposed to the observed mean state. The biases of mean climate states are generally small and are reported in the Supplementary Text S1.

The perturbation runs are performed with projected Arctic sea-ice loss such that sea-ice thickness matches the mean sea-ice thickness of the year 2081–2100 of RCP8.5 simulation. The details of how the forcing is applied are explained in 2.A. As we did for the CTL runs, the sea-ice-loss runs are denoted by SIL_[MODEL]. Also, we denote the entire set of sea-ice-loss runs as SIL and define RESP_[MODEL] := SIL_[MODEL] − CTL_[MODEL].

SIL is run for 180 years. The mean ocean temperature of the top 503.7 m ocean of SIL_SOM quickly reaches equilibrium within 50 years whereas the rest of the models adjust quickly in the first 80 years and drift slowly afterward (Figure S2a). The common globally integrated

drift for SIL_OGCM, SIL_EMOM and SIL_MLM is due to the weak background vertical diffusion. However, regionally the drift pattern is not the same across the hierarchy and the magnitudes are weaker in simplified models (Figure S3). In SIL_OGCM, the AMOC weakens during the first 30 years followed by a recovery during the next 50 years, and then stabilizes (Figure S2b). Therefore, we analyze years 81–180 and use this period to represent the decadal and centennial adjustment of the climate system.

2.3 Results

2.3.1 The impact of ocean processes on variability

Even though hierarchy members produce a similar climate mean states (see Supplementary Text S1), their variability may differ. Here, we define "variability" as the standard deviation of the anomaly time series of the given variable. The anomaly is the deviation from its climatology (monthly, seasonally, or annually depending on the context).

We also examine the "re-emergence" of SST anomaly (SSTA). It refers to the 12-month lag correlation of SSTA in winter (M. A. Alexander, Scott, and Clara Deser, 2000). This memory effect is a consequence of seasonal mixed-layer entrainment, which leads to enhanced predictability.

Variability of SST and surface air temperature

Because our simplified models cannot generate most of the tropical variability due to the lack of Kelvin and Rossby waves dynamics, direct comparison between full OGCM with the simplified models would be harder to interpret. Thus, we define CTL_OGCM* as the filtered CTL_OGCM in which we subtract out the projection of the variability on the first empirical

orthogonal function of the monthly SSTA between 20°S–20°N.

In general, the SST variability is similar to that of CTL_OGCM*, with higher variability along the storm track (Figure 2.2). We also notice that SST variability decreases by about 10˜30% in CTL_MLM and CTL_EMOM compared to CTL_SOM (Figure 2.2) even though they have similar atmospheric variability (sea-level pressure, not shown). Since CTL_SOM does not have mixed-layer entrainment, it highlights the importance of the seasonal entrainment in winter that acts to dampen the stochastic atmospheric forcing. We further verify that mixed-layer entrainment can effectively reduce the SST variability by constructing a stochastic one-dimensional mixed-layer model in 2.B.

The inclusion of Ekman flow improves the shape of SST variability in certain parts of the mid-high latitude ocean (Figure 2.2). These regions are Northern Pacific (box A), Northern Atlantic (box B), and Pacific-Atlantic sector of Southern Ocean (box C). In particular, the tongue-shaped SST variability pattern extending eastward from Japan (box A) in CTL_EMOM resembles the pattern of PDO SST variability. Since we cannot observe this in CTL_SOM and CTL_MLM, it shows that Ekman is an essential process in reshaping the SST variability pattern. This is consistent with M. A. Alexander and Scott (2008) and Miller and N. Schneider (2000) that a portion of PDO SST variability originates from the coupled effect of the weather noise with Ekman flow. Our hierarchy demonstrates this effect. However, the magnitude of the SST variability in box A is not as strong as the variability in CTL_OGCM*, implying that the Kuroshio Extension variability, which is not captured in our simplified models, is an important contributor to SST variability in the North Pacific. In summery, as we move up the hierarchy, the SST variability gets closer to the variability in the OGCM. But, disappointingly, this trend does not translate into the surface-air-temperature variability (Figure 2.3).

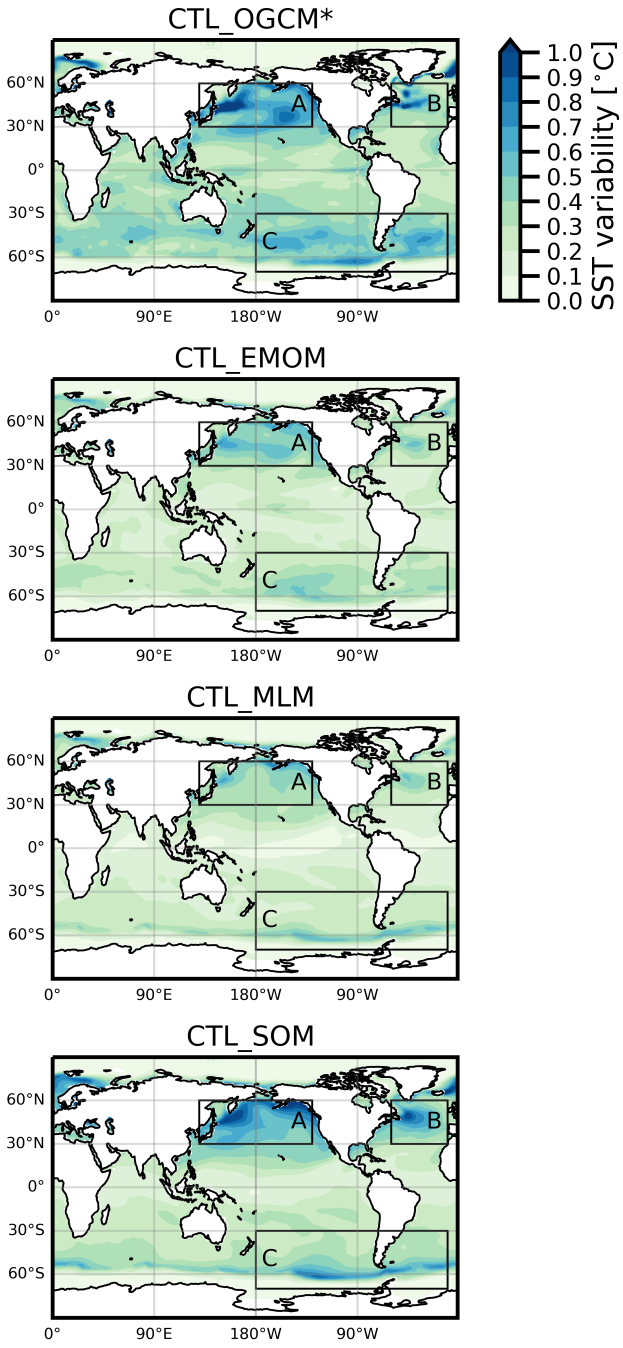

Figure 2.2: The annual mean SST variability (standard deviation of SSTA) of CTL run. The variability in CTL_OGCM* is computed by removing the anomalies that are correlated with the time series of the first empirical orthogonal function of monthly SSTA between 20°S–20°N. Boxes A, B, and C show the regions that have the biggest differences.

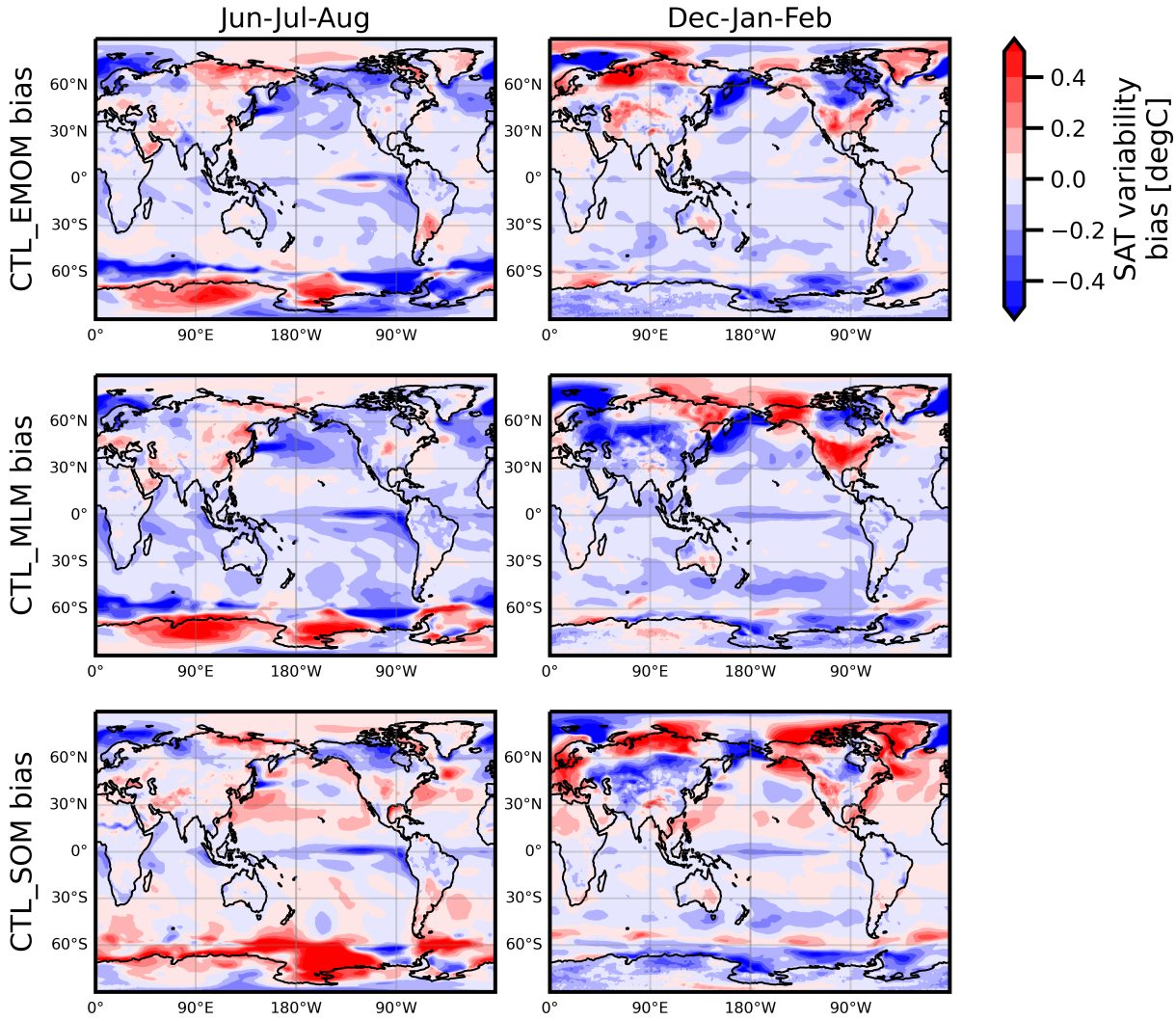

Figure 2.3: The Jun-Jul-Aug and Dec-Jan-Feb mean SAT variability bias (standard deviation of CTL_[member] - standard deviation of CTL_OGCM*). See the caption for Figure 2.2 for the definition of CTL_OGCM*.

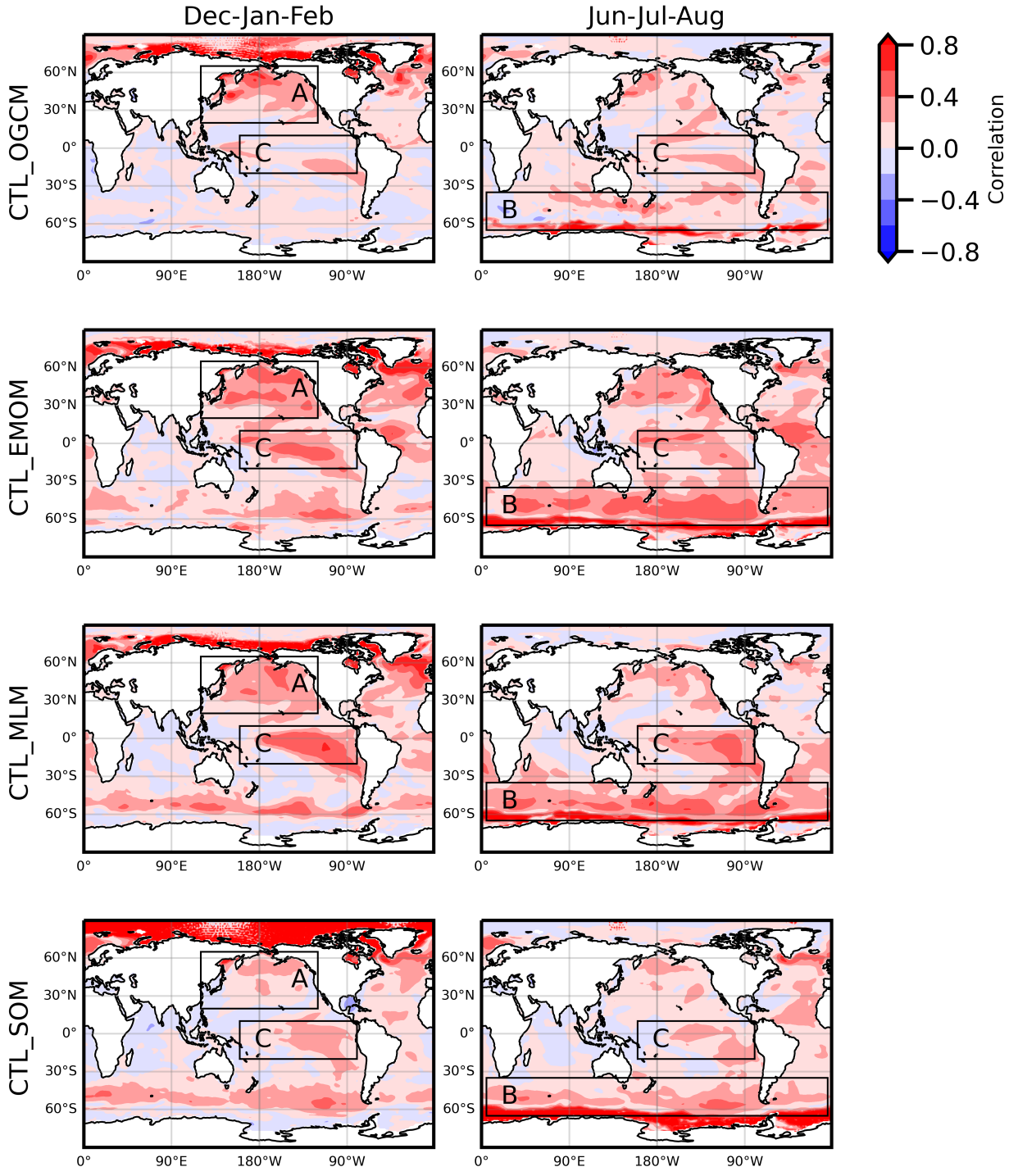

Figure 2.4: SSTA winter-to-winter correlation. Here Dec-Jan-Feb and Jun-Jul-Aug are winters in northern and southern hemispheres, respectively. Box A shows the improvement over the Northern Pacific as more ocean processes are included. Boxes B and C show that there are major processes not captured in simplified models that removes the memory. In box B, we speculate these are the northward transport of the subducted Antarctic Intermediate Water and the diffusive effect of eddies. In box C, horizontal currents and wave dynamics might act to dampen the SSTA efficiently.

SSTA re-emergence improvement

In CTL_OGCM, we find stronger re-emergence signals in higher latitudes during winter, specifically in the North Pacific (Figure 2.4 box A) and Southern Ocean (Figure 2.4 box B). While the re-emergence bias is reduced in the North Pacific (box A), it is too strong in the Southern Ocean (box B). We speculate that in the Southern Ocean, the northward transport of the subducted Antarctic Intermediate Water and diffusive effect of eddies remove much of the signal that leads to low winter-to-winter correlation in the CTL_OGCM. Without these processes, winter-to-winter correlation will be too strong.

In all simplified models, a strong winter-to-winter correlation is present in the tropical Eastern Pacific while there is none in CTL_OGCM (Figure 2.4 box C). Although we are unsure for the causes to the low winter-to-winter correlation in CTL_OGCM, we speculate that it is due to the presence of the horizontal currents and wave dynamics that may act to damp the temperature anomalies.

The Ekman flow is important for decadal frequency of PDO

To better understand how various ocean processes contribute to SST variability in the North Pacific, we compare the spatial PDO pattern and the spectrum of the PDO index across the hierarchy. Here the PDO is defined as the first empirial orthogonal function (EOF) of the SST over the North Pacific (20°N to 70°N, e.g. M. Newman et al., 2016) and the PDO index is the associated principle component. Figure 2.5 shows the PDO patterns for the hierarchy. The patterns are the generally the same among the members of the hierarchy. Still, the tongue-shaped pattern extending from Japan eastward is better simulated in CTL_EMOM than in CTL_SOM and CTL_MLM, underscoring the importance of Ekman coupling for modifying the PDO pattern.

The periodogram of the PDO index shows more pronounced differences (Figure 2.6). The target model, CTL_OGCM, has a peak at about 5 years which is missing in other models due to the absence of ENSO in the simplified models as expected. Interestingly, CTL_OGCM also has a peak between 20–50 years which is present in CTL_EMOM but not others. The low-frequency variability for CTL_MLM is generally weaker than other models. These differences suggest that mixed-layer entrainment tends to damp the PDO's low-frequency variability while Ekman flow tends to enhance it. CTL_SOM has a 20-year peak which is somewhat shorter than the peaks seen in other models. While it is not surprising that SOM is capable of generating decadal variability, it is an artifact because this signal is eliminated once the seasonal entrainment is included.

2.3.2 Response to sea-ice loss

This section presents the analysis of the climate response during year 81–180 to Arctic sea-ice loss. The experiment detail is documented in Section 2.2.7.

Roles of entrainment and AMOC slowdown in ocean heat uptake

All the models in the hierarchy show a significant SST warming in the northern hemisphere due to Arctic sea-ice loss forcing (Figure 2.7), whereas the southward extent of the warming gets weaker as more ocean processes are included. In the North Pacific, the southward extent of the warming in RESP_EMOM is similar to RESP_OGCM, especially the warm SST tongue in the central North Pacific. In contrast, in the North Atlantic the SST cooling in RESP_OGCM, also known as the "SST warming hole", is not simulated in any of the simplified models. The warming hole in RESP_OGCM seems to reduce the latitudinal warming extent across the North Pacific as well.

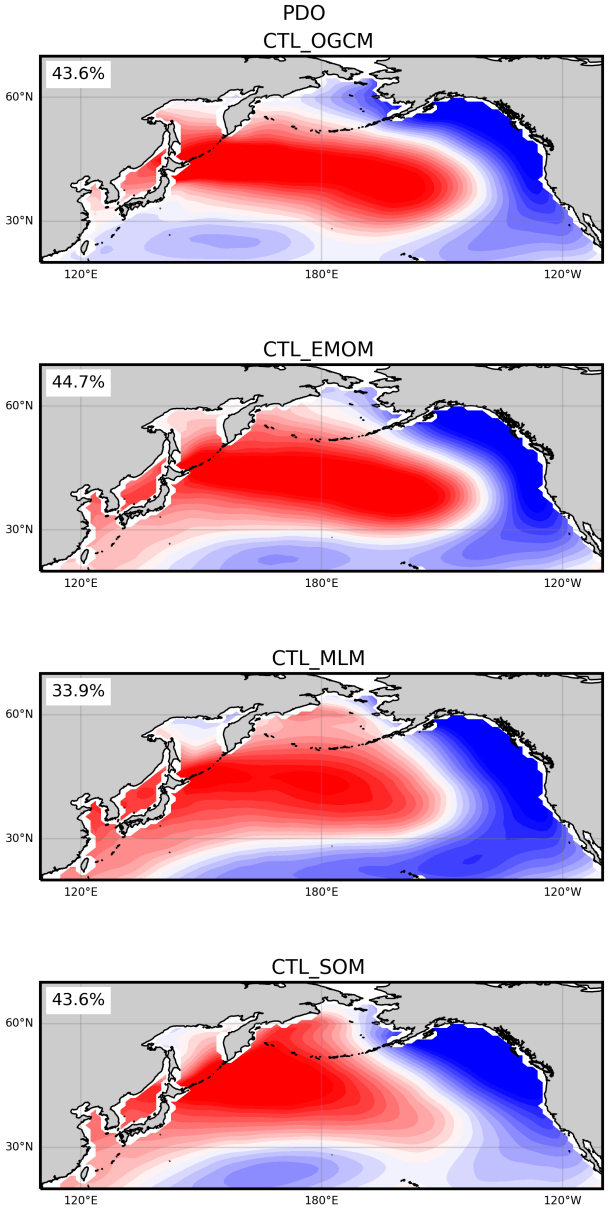

Figure 2.5: The PDO of each member in CTL. Positive and negative values are shown in red and blue shading, respectively. The PDO is defined as the first empirical orthogonal function (EOF) of monthly SST anomaly in the boxed region in 115°E–75°W and 20°N–65°N. The PDO patterns are largely the same across the model hierarchy with a prominent negative region extending from Japan eastward, showing the pattern is controlled by atmospheric processes. However, the more extended negative anomaly (blue patch) from Japan eastward in CTL_EMOM compared to CTL_SOM and CTL_MLM is consistent with CTL_OGCM, showing that coupled Ekman flow enhances the PDO pattern.

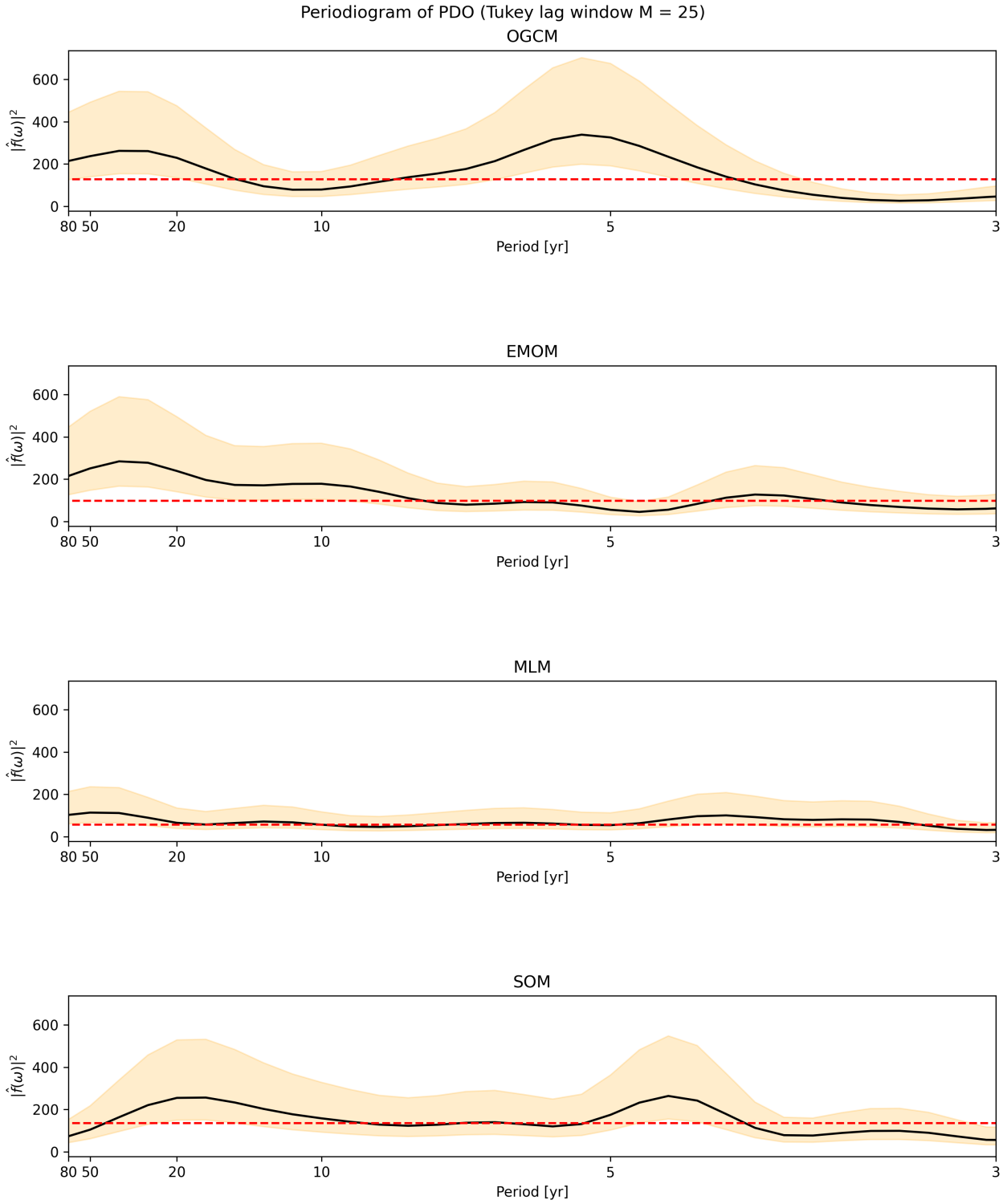

Figure 2.6: The periodogram of PDO index. PDO index is defined as the projected value of monthly SST anomaly onto PDO patterns shown in Figure 2.5 in CTL runs. The black line is the spectrum applied with Tukey window $M = 25$ where the orange shading is the 90% confidence level (see Chapter 7 of Chatfield, 2003) and red dashed line is the white noise (average of the spectrum).

The warming extent of SST in SOM is the largest, which is consistent with the fact that the SOM traps the heat in the ocean surface layer. Furthermore, including mixed-layer entrainment and Ekman flow is insufficient to reproduce the reduced extent of warming and the warming hole in the North Atlantic as seen in RESP_OGCM. The SST warming is better captured in the North Pacific than in the North Atlantic in our simplified models. Since AMOC responds strongly to sea-ice loss (Figure S2b), we speculate that AMOC in the OGCM efficiently removes the anomalous heat after being transferred to the subsurface in the Atlantic. The role of the AMOC slowdown can be understood from the rough alignment of the anomalous AMOC upwelling (Figure 2.8) with the latitudinal location of the SST warming hole in RESP_OGCM (Figure 2.7) between 40°N–60°N. The slowdown of AMOC creates an anomalous heat flux divergence between 40°N–60°N that removes the anomalous heat entrained from the surface. Thus, the efficient ocean heat uptake in RESP_OGCM is a combined effect of entrainment and AMOC slowdown.

The response of the position of westerly jet is sensitive to ocean heat uptake

The atmospheric zonal mean temperature response to Arctic sea-ice loss aligns latitudinally with the warming response in the ocean in all the models (Figure 2.9). The horizontal and vertical extent of the warming decreases as we include more ocean processes. Since the response follows the thermal wind relation (not shown), we can use the resulting different meridional gradients of the zonal mean temperature to explain the mean jet response. For example, we see that in RESP_SOM, the atmospheric warming is so extensive that it reduces the meridional temperature gradients on both sides of the westerly jet, resulting in an overall weakening of the jet. The gradients in RESP_MLM and RESP_EMOM over the northern edge of the jet decrease much more than to the south, which weakens the westerly jet and shifts it southward. Furthermore, in RESP_OGCM the temperature gradient is decreased to the north but increased to the south in the tropical upper troposphere such that the jet is

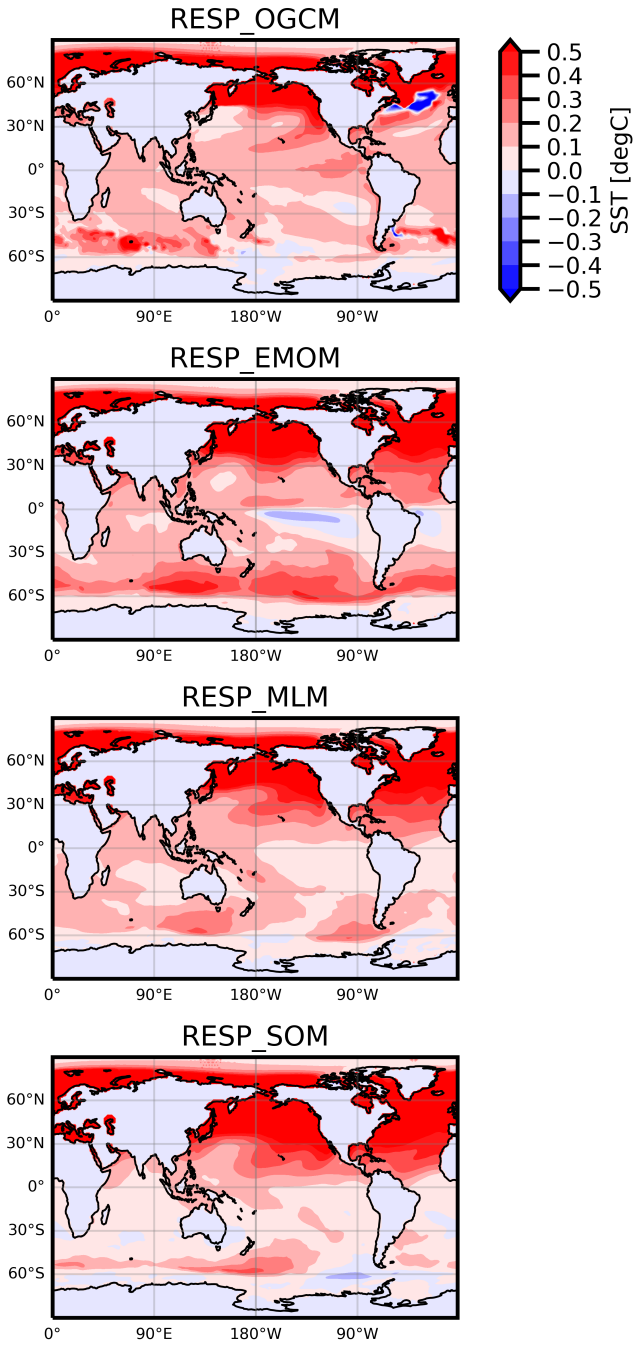

Figure 2.7: The annual mean SST response to Arctic sea-ice loss. The response is defined as RESP_[member] := SIL_[member] - CTL_[member]. As we move up the hierarchy, the extent of SST warming decreases, demonstrating the ocean's improved ability to buffer the effect of the warming as more processes are included.

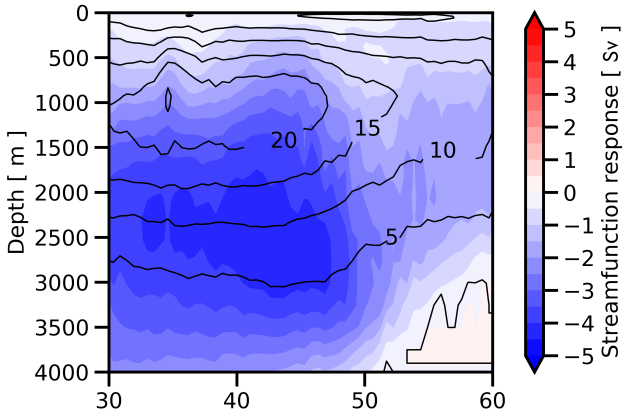

Figure 2.8: The AMOC streamfunction in CTL_OGCM (contours, in Sv) and its response to the loss of Arctic sea-ice in RESP_OGCM (shading). The anomalous upwelling that removes the entrained heat from the surface is located between 40°N–60°N. The heat removal creates the warming hole over the North Atlantic, as seen in Figure 2.7.

shifted rather than weakened. We conclude that the response of the westerly jet to sea-ice loss is sensitive to ocean processes that take up the heat.

The response of ITCZ position is sensitive to ocean processes

The response of tropical precipitation to Arctic sea-ice loss highlights the connection between sea-ice loss and ITCZ shifts (Figure 2.10). The ITCZ shifts northward, into the warmed hemisphere, in all models but with various extents and shapes. In RESP_SOM, there is a significant northward shift of ITCZ across the globe and this signal is reduced in RESP_MLM and amplified in RESP_EMOM. Note that RESP_OGCM shows a moderate ITCZ shift in the Atlantic Ocean and mostly a narrowing of the rainband towards the equator in other basins.

The shift in the ITCZ is a consequence of the excessive energy that is injected into the Arctic and transported across the equator into the southern hemisphere. This anomalous planetary heat transport (PHT) is partitioned into atmosphere heat transport (AHT) and OHT. The ITCZ shift is correlated with the anomalous AHT (T. Schneider et al., 2014). Here, we

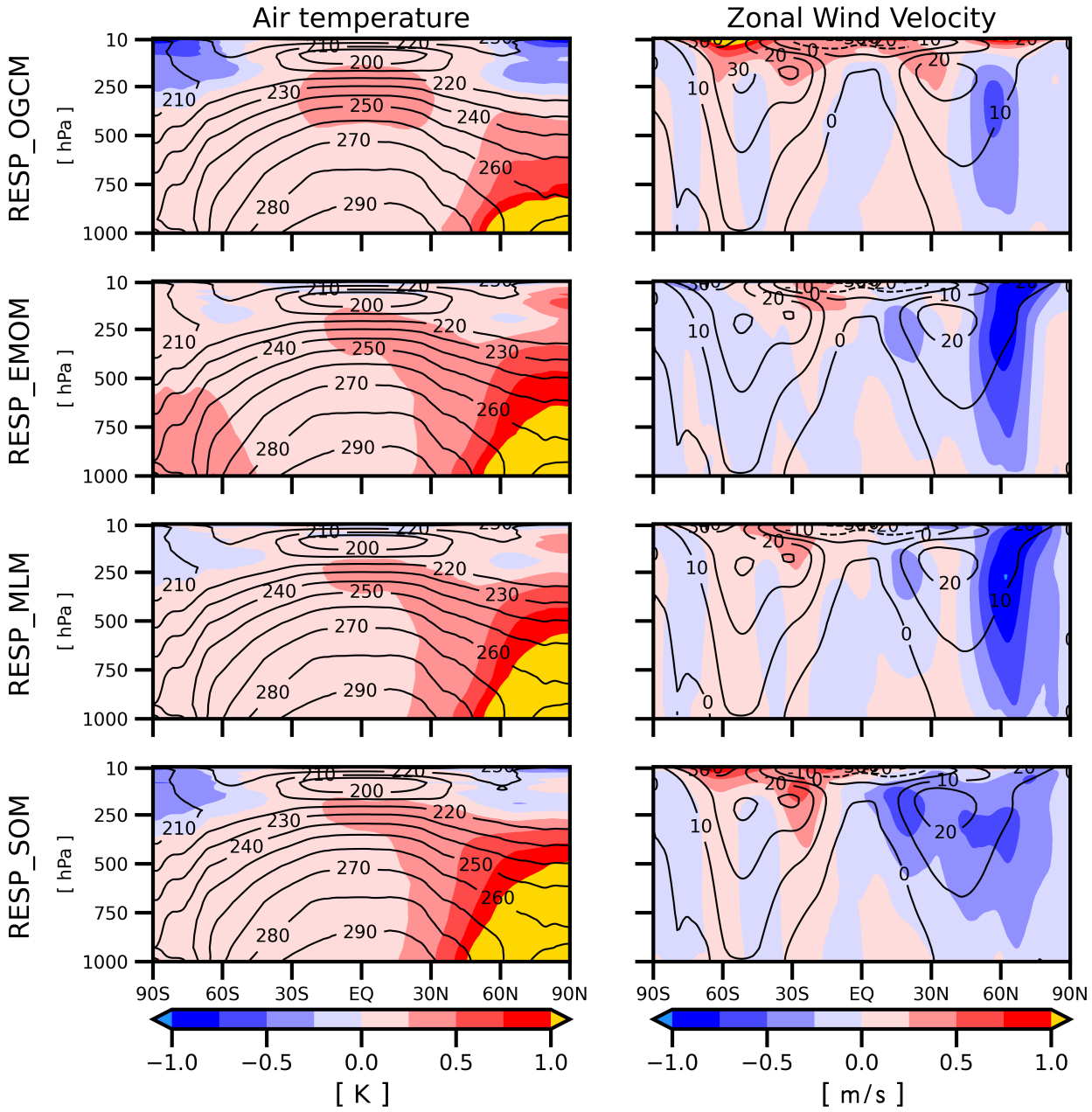

Figure 2.9: The zonal mean response of the atmosphere to Arctic sea-ice loss. The shading shows the response (RESP_[member] := SIL_[member] - CTL_[member]) of zonal mean air temperature (left column) and zonally mean zonal wind (right column). The contours show the quantities in CTL_[member].

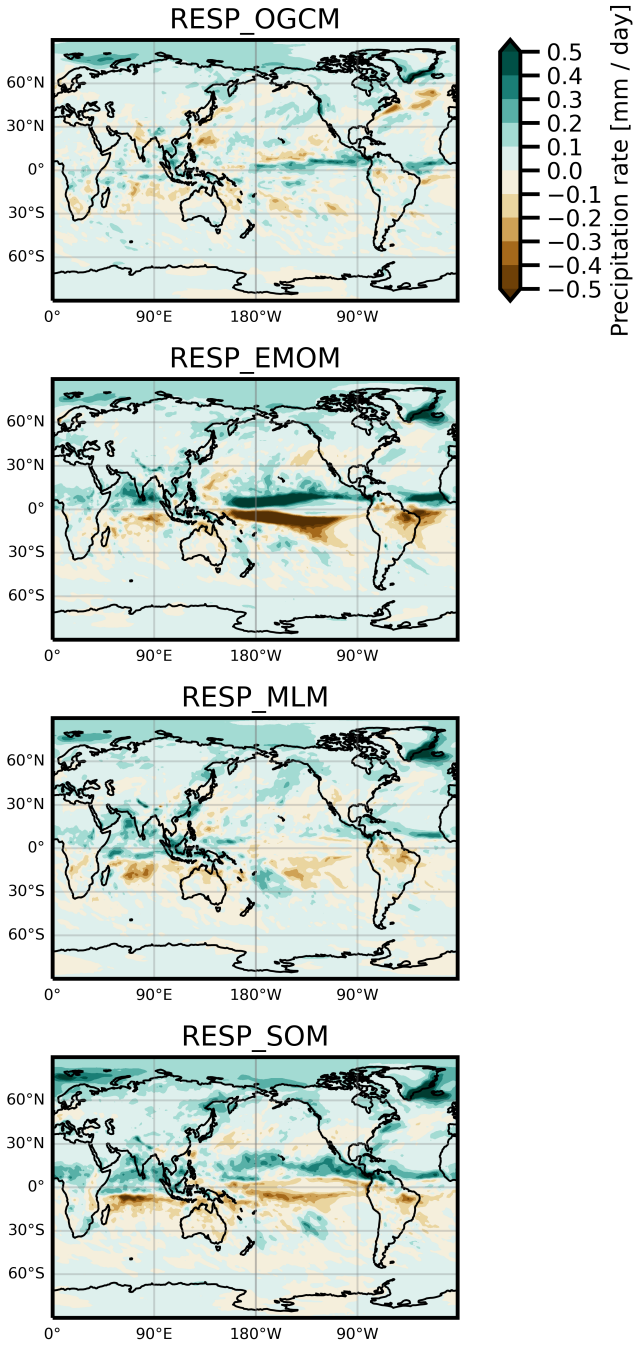

Figure 2.10: Similar to Figure 2.7 but for annual mean precipitation. Most of the responses locate in the tropics. RESP_OGCM shows a narrowing of ITCZ in the Pacific but a northward shift in the Atlantic. Rest of the models show various degree of northward shift of ITCZ.

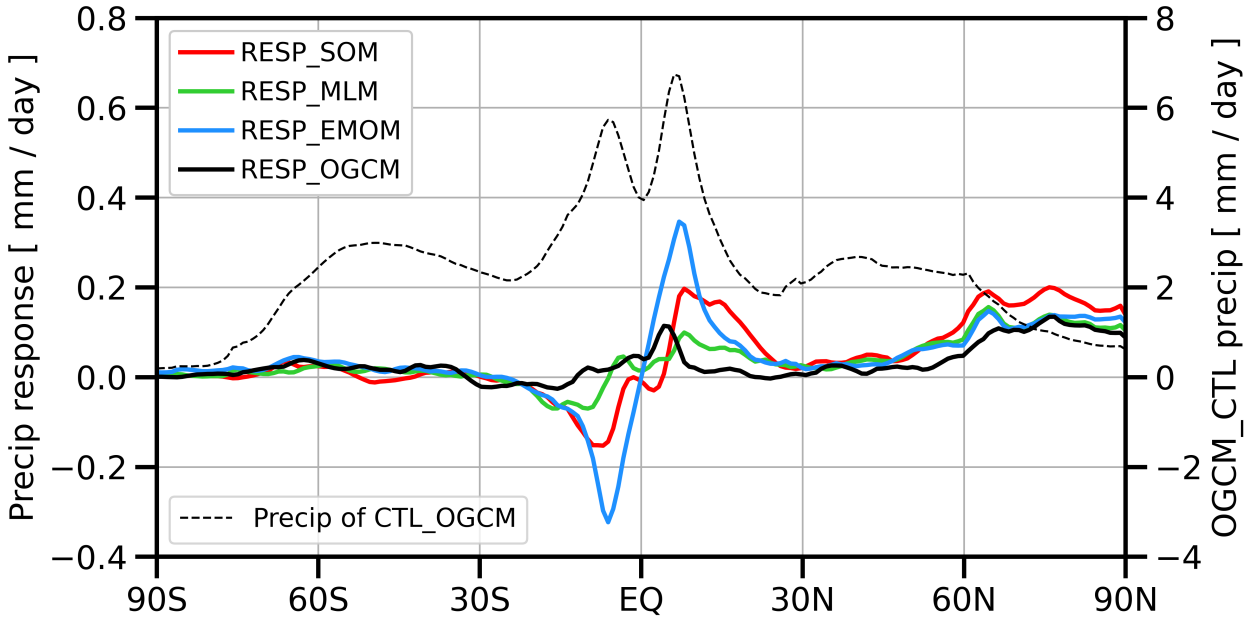

Figure 2.11: Response of zonal mean of annual precipitation (RESP_[member] := SIL_[member] - CTL_[member]; left ticks). Dashed line shows the precipitation in CTL_OGCM (right ticks).

expect that the ITCZ shift may be suppressed in two ways: by (i) ocean heat uptake, or (ii) southward cross-equatorial OHT through Ekman flow.

The suppression of ITCZ shift by ocean heat uptake is a mechanism that should apply to RESP_MLM, RESP_EMOM and RESP_OGCM because they all include the mixed-layer dynamics that can detrain heat anomalies into the deeper ocean, where they are prevented from interacting with the atmosphere.The increased cooling caused by the weak-restoring is 0.01 PW in RESP_SOM and five times greater (0.05 PW) in RESP_MLM and RESP_EMOM, showing that the coupled effect of entrainment and weak-restoring greatly enhances the heat uptake by the deep ocean. From Figure 2.11, we see that the zonal mean precipitation peaks at the same latitude in RESP_MLM and RESP_SOM. However, the peak in RESP_MLM is only half the strength, which once again shows the buffering effect of entrainment. Since the entrained heat accumulates but is also slowly removed due to the weak-restoring, we expect ITCZ response in RESP_MLM to get closer to but always stay weaker than RESP_SOM. In RESP_OGCM, since the anomalous AMOC takes up the heat even more efficiently. This

mechanism is not apparent in RESP_EMOM where the signal is dominated by the Ekman response and therefore the effect of entrainment is shielded.

The argument for the suppression of the ITCZ shift by the Ekman flow hinges on the expectation that the anomalous zonal wind stress associated with the ITCZ shift drives a southward Ekman OHT in both hemispheres (Green and J. Marshall, 2017; T. Schneider, 2017; Green, J. Marshall, and Campin, 2019; Kang, 2020; Adam, 2021). However, our simulation RESP_EMOM shows the opposite. As shown in Figure 2.12 lower panel, both the central Pacific and the western Atlantic have a pronounced northward ITCZ shift. The shift produces a northward cross-equatorial surface wind anomaly and, therefore, a cross-equatorial oceanic Ekman flow. The anomalous Ekman upwelling and downwelling further generate cold and warm SST anomalies that strengthen the dipole pattern in the atmosphere. This mechanism as a positive feedback for the ITCZ shift.

To understand the apparent inconsistency between the amplified ITCZ shift in RESP_EMOM and the expectation from past studies arguing that Ekman flow should damp the shift, we examine the Ekman OHT, i.e. $\mathrm{OHT}_{\mathrm{EK}}$ defined in Equation (2.6). In Figure 2.13, we show the anomalous wind stresses and OHT components in EMOM due to τ^x and τ^y. While the OHT due to τ^x is consistent with past studies (Kang, Y. Shin, and Codron, 2018; Kang, Y. Shin, and Xie, 2018), the northward OHT due to τ^y, neglected in these studies, is big enough to change the qualitative behavior of ITCZ in our simulation. There is evidence from both observations and comprehensive OGCMs, that the cross-equatorial wind can drive a meridional overturning cell at the equator. For example, the observational study of Y. Wang and McPhaden (2017) demonstrates the existence of shallow surface overturning cell in the Indian Ocean (see their Figure 4) and the OGCM study of Steven R Jayne and Jochem Marotzke (2001) also shows a shallow frictionally driven Ekman overturning cell within the top 100m of the ocean surface (see their Figure 9). Further evidence can be found in the OGCM study of Green, J. Marshall, and Campin (2019) — a surface-trapped overturning cell

with northward OHT that is superimposed onto the deeper and stronger counter-rotating overturning cell with southward OHT at the equator can be seen in their Figure 5c in response to a forced Arctic warming. Although the frictionally-driven cell is poorly resolved, its effect on the OHT is visible in their Figure 9b. The bump in the OHT-v.s.-latitude plot at the equator is a manifestation of the anomalous frictionally-driven Ekman heat transport. However, Equation (2.6) also shows that $\mathrm{OHT}_{\mathrm{EK}}$ is proportional to ΔT, which can be directly modified by the choice of $H_{\mathrm{total}} = H_{\mathrm{EK}} + H_{\mathrm{RF}}$, the total thickness for the Ekman and return flows. As a result, our simplified model could potentially be sensitive to the choices of H_{EK} and H_{RF}.

We summarize this discussion in Figure 2.14 that shows the decomposition of the heat transport in each model. In the RESP_SOM and RESP_MLM, almost all the response is through AHT with a small contribution from OHT. The contribution of diffusion to OHT is small. The AHT in RESP_MLM is smaller than for RESP_SOM because the ocean takes up the heat. In RESP_OGCM, the ocean takes up heat and also transports it horizontally so that the subsurface cold water can be replenished to efficiently take up the heat. In RESP_EMOM, the OHT at the equator is northward due to frictional Ekman flow, resulting in an amplification of the ITCZ shift.

Eastern Pacific SST response in RESP_OGCM

In this section, we want to comment on the SST warming response over the Eastern Pacific in RESP_OGCM that is absent in other hierarchy members (Figure 2.7). A similar response has been found in the studies that force the climate model with increased greenhouse gases (Vecchi and Soden, 2007; Xie et al., 2010; Mamalakis et al., 2021). These studies found that the warming of the Eastern Pacific is a consequence of the weakening of the Walker circulation. In our simulation, we find that surface wind and oceanic upwelling do not change significantly in RESP_OGCM (Figure 2.12 upper panel). Instead, the increased shortwave

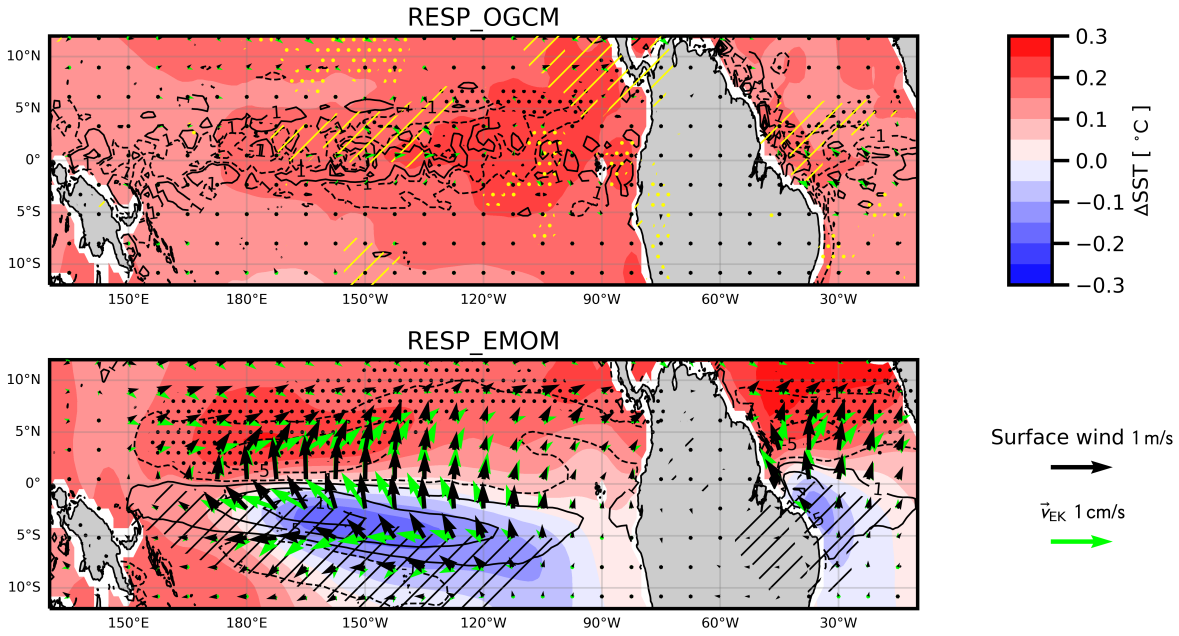

Figure 2.12: The detailed analysis of tropical response in RESP_OGCM (upper panel) and RESP_EMOM (lower panel). The shading is the response of SST. The black and green arrows are the anomalous surface wind and their induced $\vec{v}_{\mathrm{EK}}$ computed using Equation (2.4). The black dotted and slanted hatches represent the increase and decrease of annual mean precipitation more than 100mm. In RESP_OGCM we further denoted the increase and decrease of downward shortwave radiation exceeding $\pm 1 \mathrm{W/m^2}$ by yellow dotted and slanted hatches.

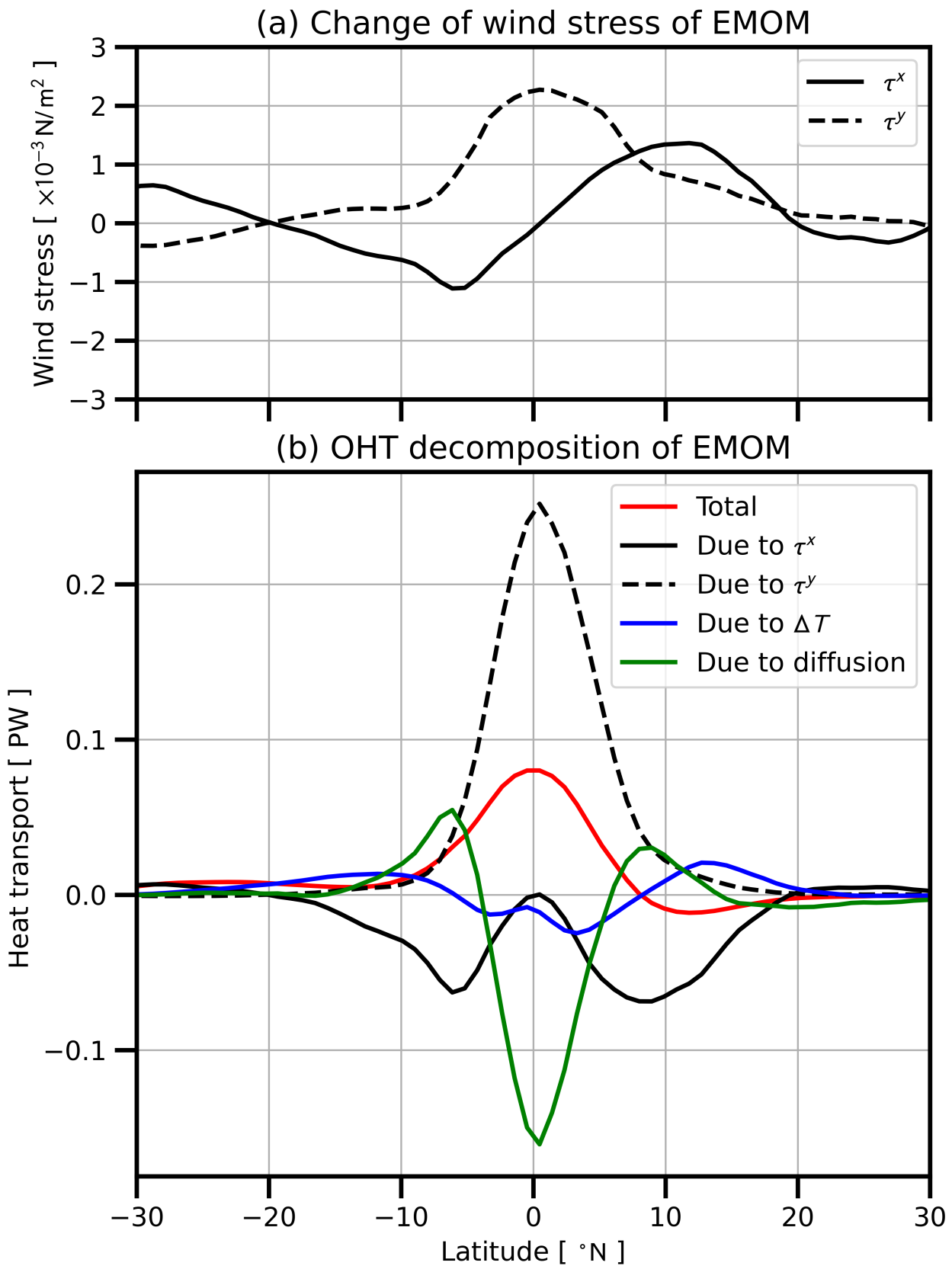

Figure 2.13: (a) The response of surface zonal wind stress τ^x (solid; positive values means eastward wind anomalies) and meridional wind stress τ^y (dashed; positive values means northward wind anomalies) in EMOM. (b) The decomposition of OHT response in EMOM. The OHTs associated with τ^x, τ^y and ΔT are derived from Equation (6) by taking its differential form.

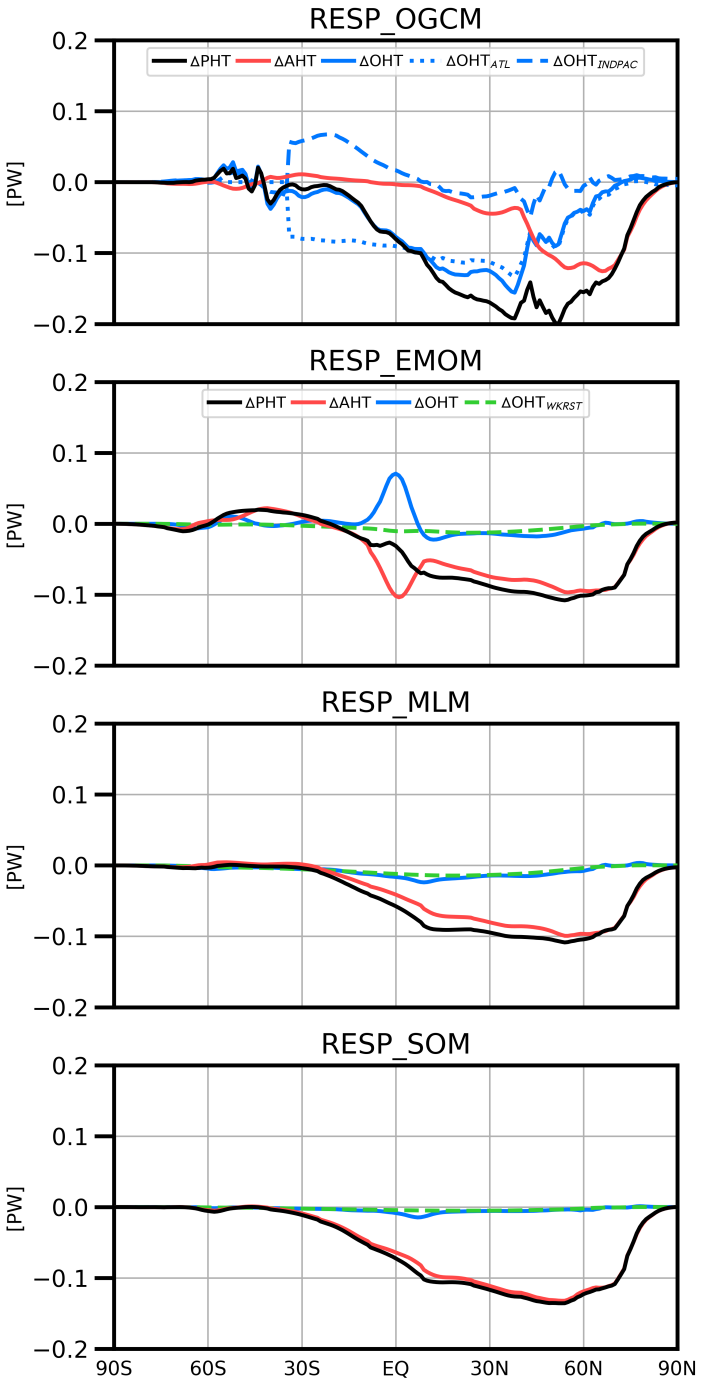

Figure 2.14: Heat transport response analysis. PHT = AHT + OHT. The OHT in RESP_OGCM is further decomposed into Indian-Pacific and Atlantic basins ($\Delta\text{OHT}_{\text{INDPAC}}$ and $\Delta\text{OHT}_{\text{ATL}}$). In the simplified models, we also plot out the OHT due to weak-restoring ($\Delta\text{OHT}_{\text{WKRST}}$) to show it is a minor component. In RESP_SOM and RESP_MLM, OHT is fully contributed by diffusion.

radiation pattern matches the warmest SST anomaly, suggesting that the decrease in reflective clouds causes the surface warming. The warm anomaly is then advected downstream to the central Pacific where it drives the intensification of the ITCZ such that there is a decrease of downward shortwave radiation over the Central Pacific. The difference in the tropical Eastern Pacific response to greenhouse gas forcing and sea-ice loss forcing deserves more investigation in future studies.

2.4 Conclusion

In this paper, we constructed a hierarchy of ocean models including SOM, MLM, EMOM, and OGCM (POP2) that separates mixed-layer entrainment and Ekman flow by progressively including each process into the model. We further couple it to the climate model CESM1 with realistic topography and successfully derive three-dimensional correction flux through the nudging method so that the appropriate climatologies for SST, precipitation, and sea-ice area are reproduced.

The mixed-layer entrainment is important for multiple reasons. In the control climate, we found that mixed-layer entrainment significantly reduces the SST bias in SOM. The entrainment also reduces SST variability that is exaggerated in SOM, since it introduces cold deep water into the mixed-layer during winter when interannual variability is the strongest. Entrainment also results in stronger winter-to-winter SSTA correlation in agreement with the OGCM almost everywhere. There are, however, two prominent exceptions. In the Southern Ocean and tropical Eastern Pacific, the simplified models produce too high winter-to-winter SSTA correlations. Because horizontal transport would remove local temperature anomalies, we speculate that the high correlation is due to their absence in the simplified models. In the sea-ice loss perturbation experiment, including entrainment allows the deep ocean to take up the excessive heat associated with sea-ice loss and reduces the spatial extent

of the warming in the atmosphere. Thermal wind relation then translates the anomalous atmospheric warming structure into a latitudinal shift of the westerly jet.

Moreover, the fact that mixed-layer entrainment alone cannot efficiently remove the heat by horizontal transport highlights the function of AMOC: the AMOC removes the subsurface water carrying the heat entrained from the surface and replaces it with cold water. The uptake of thermal energy also dampens the ITCZ shift because it temporarily reduces the inter-hemispheric imbalance in the heat budget. Thus, entrainment affects the variability and large-scale energy transport when coupled with AMOC.

CTL_EMOM produces SST variability patterns that are in better agreement with those of the OGCM in the mid-latitude North Pacific, South Pacific, and North Atlantic oceans. Improvements in surface air temperature variability over North America and the Southern Ocean are likely associated with improved SST variability located upstream. In the sea-ice loss experiment, the Ekman flow amplifies the ITCZ shift, which contradicts past literature. This disagreement is due to the details of the Ekman parameterization, i.e., the inclusion of $\epsilon\tau^y$ and the choice of $H_{\text{total}} = H_{\text{EK}} + H_{\text{RF}}$. Thus, the ITCZ response to sea-ice loss is sensitive to the Ekman parameterization.

In Section 2.2.6, we found a coupled positive feedback that originates from having insufficient diffusion to counteract the convergence of the frictional-Ekman flow. The feedback excites a coupled mode in which the convergence in the wind field enhances the convergence of warm surface water, that feeds back positively on the atmospheric convection and associated low-level convergence. This feedback generates erroneous rainband (Figure S1a) on the equator in the Central Pacific where the cold tongues are still poorly simulated in many climate models (Tian and X. Dong, 2020). It will be interesting in future studies to investigate whether this positive feedback and cold-tongue bias are connected.

Our hierarchy can still be refined depending on the need. For example:

- The nudging method used to derive the flux correction should account for the sea-ice concentration and thickness in addition to SST. Using information about the sea-ice field will resolve the fluxes of heat that are not accompanied by a change of temperature because of the phase change. In addition, diagnosing the interannual variability of sea-ice forming heat flux $\overline{\Lambda' T'}$ in Equation (2.11) from OGCM and subtracting it out of the flux correction may avoid double counting that causes the warm SST bias in the Southern Ocean along the sea-ice edges.

- One can extend the current Ekman flow parameterization scheme by extending the thickness of the return flow layer H_{RF} from a constant to a spatially varying variable to account for sensitivity of $\mathrm{OHT}_{\mathrm{EK}}$ to H_{RF}. Devising a framework to diagnose H_{RF} from an OGCM will be necessary.

- The introduction of Rayleigh friction is not the only parameterization for resolving the singular nature of the Ekman solution at the equator. One can resolve the singularity by retaining the pressure gradient force in the momentum balance. The Ekman model in Stommel (1959) and the generalized Ekman model in Cronin and Kessler (2009) (their Equation (2) and (7a)) both retain the pressure gradient force and specify the momentum viscosity instead of Rayleigh friction parameter ϵ. After solving the resulting fourth-order ordinary differential equation for the vertical shear, the total flow can be solved by requiring that the vertical integral of the total flow be zero. Thus, the Ekman spiral and the vertical location of the return flow emerge naturally. This provides an avenue for refining EMOM.

- One can adopt the KPP scheme (Large et al., 1994; Van Roekel et al., 2018) so that the mixed-layer evolves dynamically. Using the KPP as opposed other mixed-layer models such as Niiler-Kraus (Niiler, 1977; Gaspar, 1988) will enhance the physical consistency of the hierarchy. In the KPP scheme, the momentum and tracer diffusivities are functions of the vertical shear. To bring the Ekman model in, one would need to

separate the vertical shear into a prescribed non-Ekman component and an Ekman component diagnosed from the instantaneous wind stress.

- Because of the importance of geostrophic flows for the mid-high latitude ocean heat transport, it is desirable to incoporate the wind-driven gyres and meridional overturning circulation into the hierarchy. For example, Haarsma et al. (2005) developed a regional hierarchy that resolves barotropic wind-driven flows, Ekman flows and mixed-layer entrainment. Extending such hierarchy to a global coupled model is one possible avenue for EMOM's further development. Still, one could choose to prescribe the large-scale ocean flow to achieve a certain degree of responsive temperature and salt advection.

Finally, the hierarchy can be used to couple with Community Atmoshpere Model version 5 (CAM5) instead of CAM4. Also, the code of EMOM can be easily ported to Community Earth System Model version 2 (CESM2) because both CESM1 and CESM2 use the similar coupling interface code that we modified to couple to EMOM.

Appendix

2.A Sea-ice forcing

We apply the forcing by constraining sea-ice thickness. The target sea-ice thickness in our sea-ice thickness experiment is derived from years 2081–2100 of an ensemble member of Representative Concentration Pathway 8.5 (RCP8.5) in Coupled Model Intercomparison Project Phase 5 (CMIP5) that is simulated using CCSM4. The total sea-ice volume in the SIL is about one-sixth of that in the CTL with an almost sea-ice-free Arctic in September. The distribution of mean sea-ice thickness is shown in Figure S6.

The target sea-ice thickness is achieved by imposing a pseudo heat flux to the sea-ice model,

$$F_{\text{pseudo}} = \frac{L_{\text{ice}}\rho_{\text{ice}}}{\tau_{\text{nudging}}} \left(h_{\text{model}} - h_{\text{target}}\right), \tag{2.14}$$

where h_{model} and h_{target} are the sea-ice thicknesses of the current time step and the target, F_{pseudo} is the pseudo heat flux with the sign chosen so that $F_{\text{pseudo}} > 0$ indicates an energy flux into the sea ice, $L_{\text{ice}} = 3.34 \times 10^5\,\text{J}\,/\,\text{kg}$ the specific latent heat fusion for sea ice, $\rho_{\text{ice}} = 917\,\text{kg}\,/\,\text{m}^3$ the sea ice density, $\tau_{\text{nudging}} = 5$ days is the nudging timescale, and h_{model} and h_{target} are the modeled and target sea-ice thicknesses. If the modeled sea-ice thickness is larger than the target sea-ice thickness then a heat gain causes the ice volume to decrease.

Conversely, if the modeled sea-ice thickness is less than the target sea-ice thickness then a heat loss causes the ice volume to increase towards the target. The model we use divides the sea ice into five different categories with each having its own equivalent sea-ice thickness. Since we do not differentiate them, we use the value of their sum as sea-ice thickness in the equation above. Nudging the sea-ice thickness does not uniquely determine sea ice concentration which might give rise to inconsistent ice albedo and heat exchange if forcing is weak (Sun, Clara Deser, et al., 2020). Since our forcing is very strong the discrepancy is negligible.

2.B Temporally Varying Mixed-layer Depth Changes SST variability

We construct a one-dimensional mixed-layer model by vertically integrating Equation (2.1a) from the bottom of mixed-layer to the surface to get an approximated well-mixed mixed-layer model as

$$\frac{\partial T_{\text{mix}}}{\partial t} = -\frac{F_{\text{net}}}{\rho c_p h} - \frac{w_e}{h}\left(T_{\text{mix}} - T_d\right) + q$$

where T_{mix} is the mixed-layer ocean temperature, $F_{\text{net}} = F(z = 0) - F(z = -h)$ is the net incoming energy flux into the mixed-layer, T_d is the temperature immediately below the mixed-layer, $w_e = \max(\partial h/\partial t, 0)$ is the entrainment velocity, and q is the sum of freezing and advection tendency terms. Taking the deviation (denoted with a prime) from the seasonal

mean (denoted with an overbar) we get

$$\begin{aligned}\frac{\partial T'_{\mathrm{mix}}}{\partial t} &\approx -\frac{F'_{\mathrm{net}}}{\rho c_p \overline{h}} + \frac{\overline{F}_{\mathrm{net}}}{\rho c_p \overline{h}^2} h' - \left(\frac{w_e}{h}\right)' \left(\overline{T}_{\mathrm{mix}} - \overline{T}_d\right) - \frac{\overline{w}_e}{\overline{h}} \left(T'_{\mathrm{mix}} - T'_d\right) + q' - \frac{1}{\tau_{\mathrm{adj}}} T' \\ &= -\frac{F'_{\mathrm{net}}}{\rho c_p \overline{h}} - \frac{\overline{w}_e}{\overline{h}} T' - \frac{1}{\tau_{\mathrm{adj}}} T' \end{aligned} \tag{2.15}$$

where the last term on the right-hand side is the damping of temperature anomaly due to air-sea interaction with time scale τ_{adj}. We drop the deviation terms related to h because we prescribed its annual evolution; we also drop q' because in the MLM model there is no advection and most of the ocean is sea-ice free; furthermore, we drop T_d for it is expected that $|T'_d| \ll |T'|$. We hypothesize that it is the existence of entrainment that reduces the SSTA variance.

Since strictly speaking, $\overline{h}$ used in SOM is the temporal mean of $\overline{h}$ in MLM so the first term on the right-hand side is also different, we should support this hypothesis by conducting stochastic simulations of Equation (2.15).

We set

$$\overline{h}(t) = h_{\mathrm{m}} + \frac{h_{\mathrm{amp}}}{2} \sin\left(\frac{2\pi}{P} t\right) \tag{2.16}$$

$$F'_{\mathrm{net}}(t) = \left[F_{\mathrm{m}} + \frac{F_{\mathrm{amp}}}{2} \sin\left(\frac{2\pi}{P} t\right)\right] \epsilon'(t) \tag{2.17}$$

where $P = 360\,\mathrm{days}$ is the annual cycle period, $h_{\mathrm{m}} = 70\,\mathrm{m}$ is the mean mixed-layer thickness, h_{amp} is the amplitude of mixed-layer variation, $F_{\mathrm{m}} = 30\,\mathrm{W/m^2}$ and F_{amp} are the same but for F'_{net}, $\epsilon' \sim N$ is a Gaussian noise. It is designed so such that the thicker mixed-layer thickness coincide with higher surface energy flux variance as observed in coupled simulations. SOM is represented by setting $h_{\mathrm{amp}} = 0\,\mathrm{m}$ and MLM by $h_{\mathrm{amp}} = 60\,\mathrm{m}$. In all numerical integration we select $\tau_{\mathrm{adj}} = 180\,\mathrm{days}$, $T'_{\mathrm{mix}}(t=0) = 0$, and Euler forward scheme with time step 30 days is used. For each simulation, integrate for 100-thousand years and compute the resulting

monthly mean values (30 days per month), then use the resulting T'_{mix} time series to compute one standard deviation value.

Assigning $F_{\text{amp}} = 0\,\text{W/m}^2$, the SST variability of SOM and MLM are 0.27°C and 0.21°C. Further assigning $F_{\text{amp}} = 40\,\text{W/m}^2$ we get 0.30°C and 0.20°C. The even larger separation is because larger atmospheric stochastic forcing (winter) is efficiently damped by thicker mixed-layer depth. These two sets experiments show that the main cause of lower SST variability in MLM comes from the temporally varying mixed-layer depth.

Supplimentary

2.S1 Assessment of the mean states in CTL runs

This section presents the analysis of the CTL runs. The experimental setup is documented in Section 2.7.

The simulated climates agree more with the CTL_OGCM as we include more ocean processes. We here discuss the sea-ice and SST biases as they are two important surface properties that control the climate.

2.S1.1 Sea-ice area is better constrained than sea-ice volume

For each CTL simulation with a simplified ocean model, we compared the simulated sea-ice area and the sea-ice volume to the area and volume simulated using the OGCM. The results are summarized in Table 2.S1. The relative sea-ice area biases range from -15% to +2%, while the relative sea-ice volume bias is -30% to +3%. We find a smaller bias for the area compared to the volume in both hemispheres. This larger bias for the volume compared to the area is due to latent heat fluxes in the presence of sea ice that are invisible to our method for diagnosing the flux corrections – recall that our flux corrections are diagnosed from a restoring term that acts on the water temperature (Section 2.5).

Table 2.S1: Sea-ice volume and area of CTL and SIL simulations in the northern and southern hemispheres.

	Sea-ice Volume [$\times 10^3\,\mathrm{km}^3$]				Sea-ice Area [$\times 10^6\,\mathrm{km}^2$]			
	NH		SH		NH		SH	
	CTL	SIL	CTL	SIL	CTL	SIL	CTL	SIL
OGCM	32.9	5.33	29.3	28.3	11.4	7.39	16.5	16.1
EMOM	26.2	5.20	21.0	19.5	10.8	7.02	14.4	13.7
MLM	26.5	5.21	23.6	23.1	10.8	7.02	15.1	14.9
SOM	28.7	5.25	30.4	30.1	11.3	7.15	16.9	16.8

Another possible reason for sea-ice biases is the double-counting of the $\overline{\Lambda' T'}$ term in Equation (11), as discussed in Section 2.5. In high latitudes, an important role of the ocean is to serve as a heat reservoir, meaning that the SOM can produce a portion of the interannual variability. Since lower ocean temperature activates the freezing, Λ' and T' are negatively correlated, i.e., $\overline{\Lambda' T'} < 0$. Therefore, if the term $\overline{\Lambda' T'}$ is a significant contributor to the flux correction and a significant fraction of $\overline{\Lambda' T'}$ in the CTL_OGCM, including the associated heat fluxes contributes to the warm SST biases we see in Figure 2.S4.

2.S1.2 Entrainment reduces SST bias

In all simplified models, the SST biases in most of the regions are within 0.5°C (Figure 2.S4). The biases in the CTL_SOM have a similar pattern to those obtained using the CCSM3-SOM ¡c.f. Figure 2 of ¿bitz2012climate: warmer SSTs over the tropical Eastern Pacific and the Southern Ocean and colder SSTs along the Kuroshio Extension. Once the mixed-layer dynamics are included, these biases are significantly reduced. The tropical warm bias in CTL_SOM causes more precipitation than CTL_MLM and CTL_EMOM (Figure 2.S5).

The common warm SST bias regions are along the sea-ice edge in the Southern Ocean, with CTL_EMOM having the largest bias. This contradicts our expectation that SST bias should decrease as more ocean processes are included. Since the location of this warm SST bias is

along the sea-ice edge, it might due the double-counting of $\overline{\Lambda' T'}$ the same issue as discussed in the previous section on sea-ice bias.

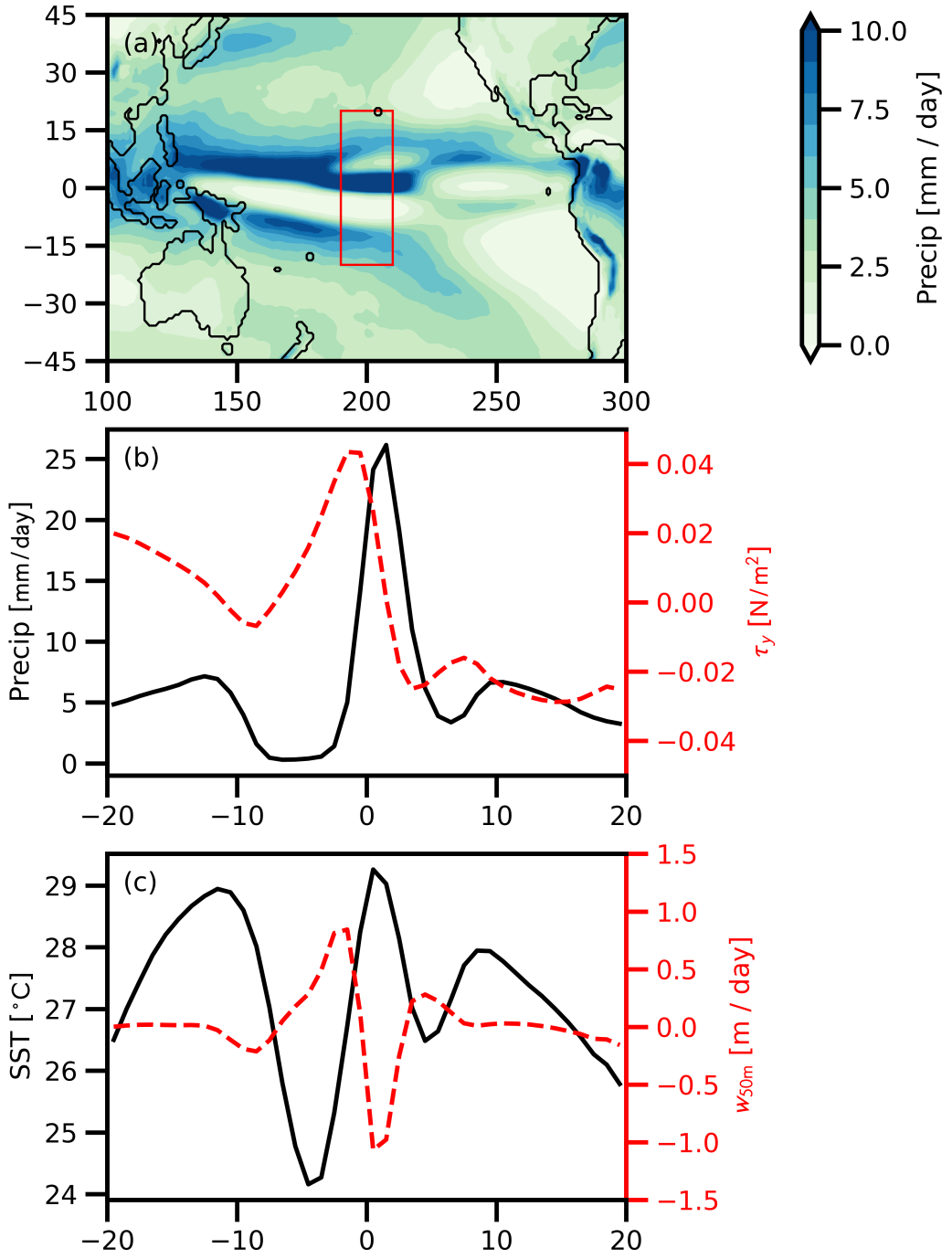

Figure 2.S1: The annual mean values of year 30 of CTL_EMOM in which uniform $K_H = 1500\,\mathrm{m}^2\,/\,\mathrm{s}$ is used. (a) shows the precipitation map of tropical Pacific. (b) shows the zonal mean precipitation (left axis, solid black) and zonal mean meridional wind stress (right axis, red dashed, positive means that wind blows northward) of the regions boxed in (a). (c) is the same as (b) but for SST and oceanic 50-m vertical velocity.

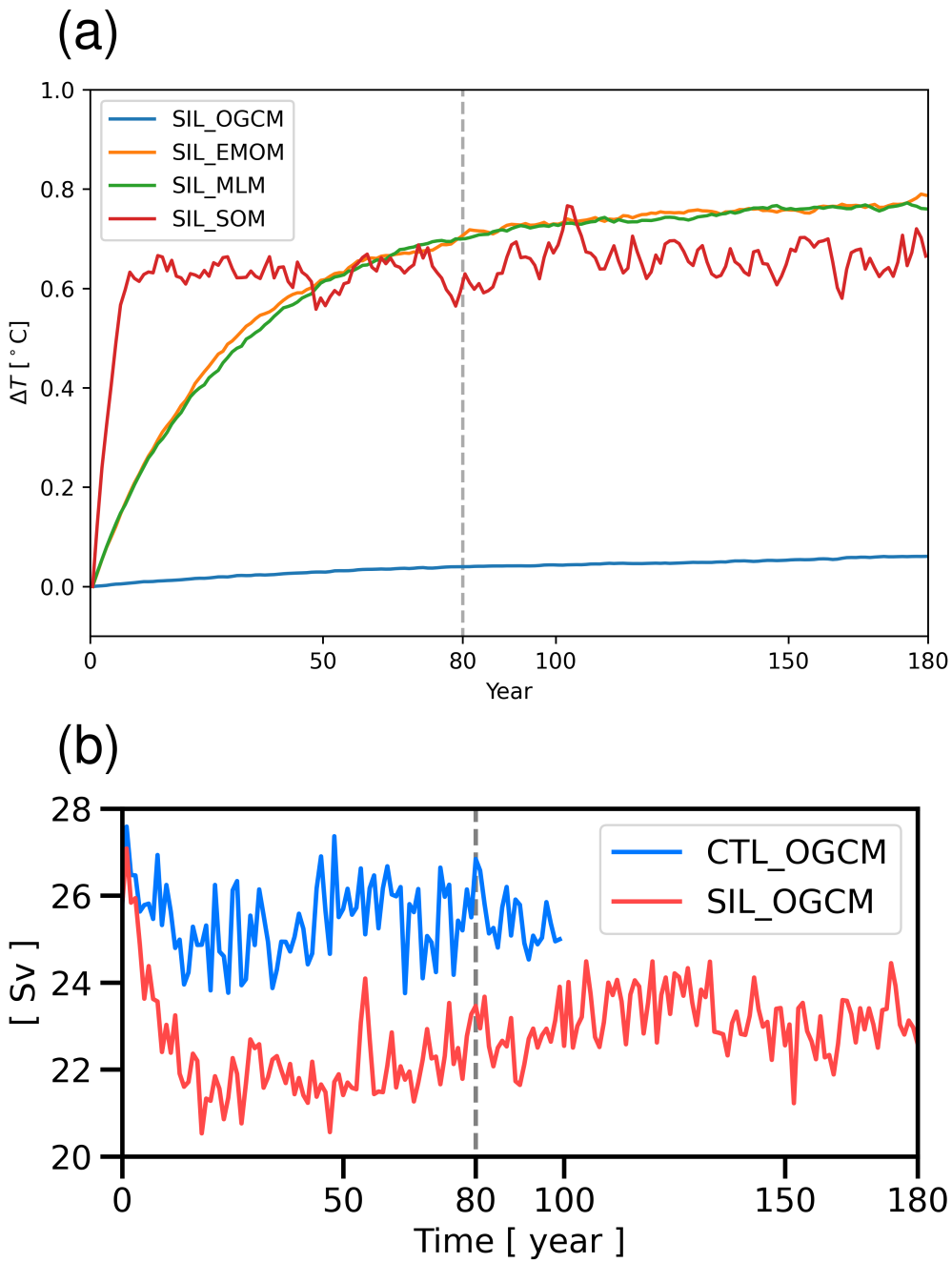

Figure 2.S2: (a) The temporal evolution of mean ocean temperature in top 503.7m in SIL relative to the beginning year of each trajectory. Time window year 80–180 during which SIL data are used for statistics is labeled. Notice that the mean ocean thickness of SOM is about 100 meters so there are more temporal fluctuations. (b) The temporal evolution of AMOC intensity measured in Sv.

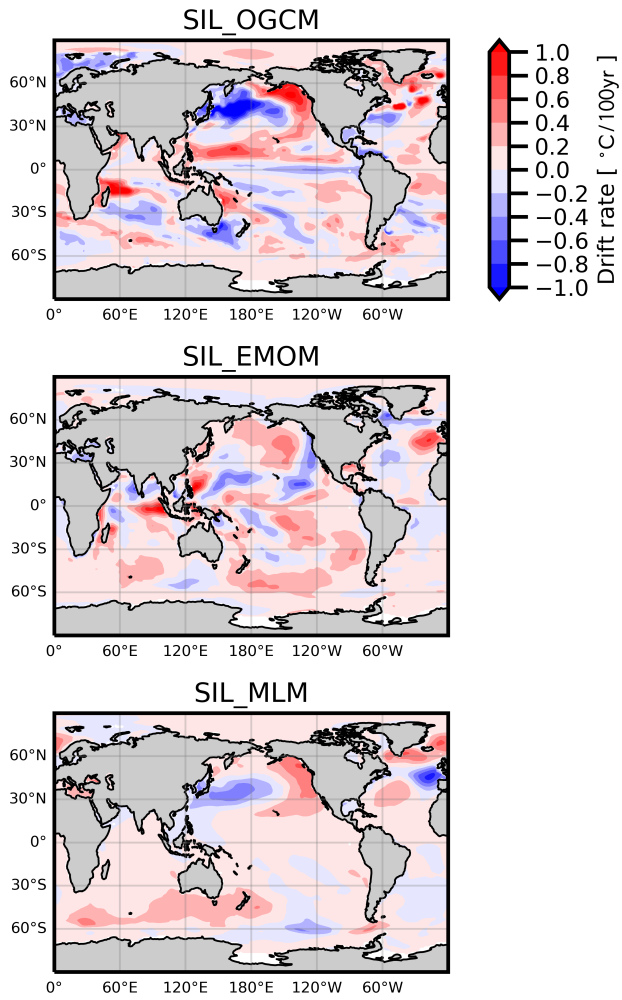

Figure 2.S3: The drift rate of averaged temperature of top 503.7m of the ocean in year 81–180 of SIL runs.

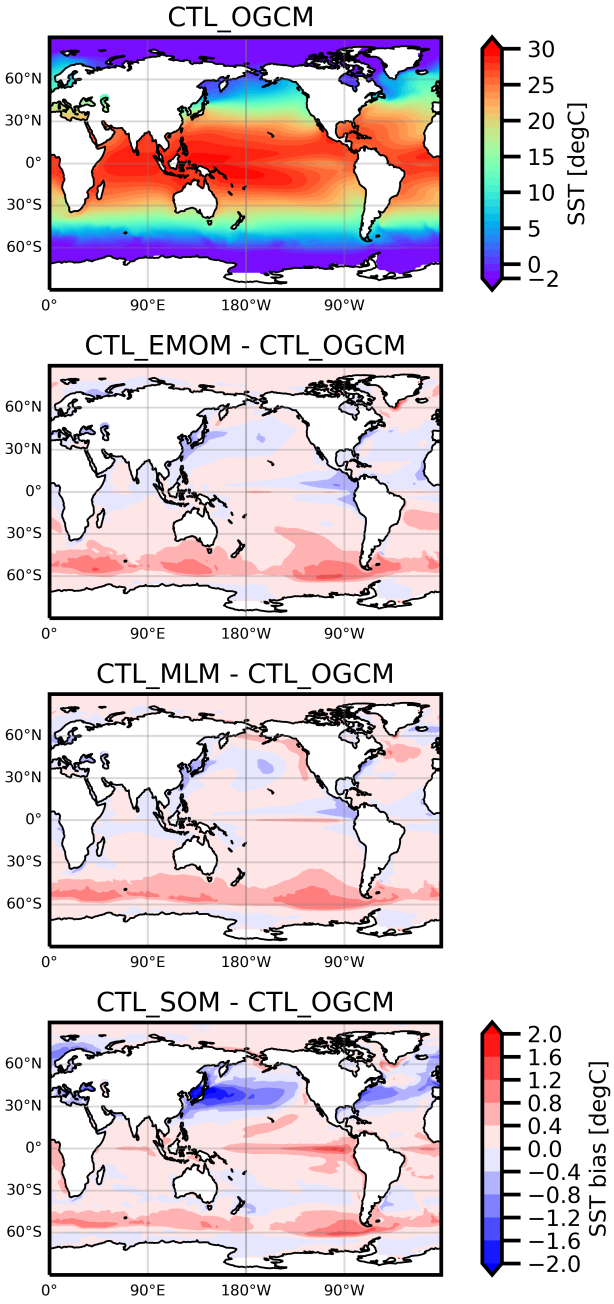

Figure 2.S4: The annual mean SST of the hierarchy in CTL run. The top panel shows the target climatology obtained from the run using the full OGCM. The other panels show the biases in the other hierarchy members, i.e., (CTL_[member] - CTL_OGCM).

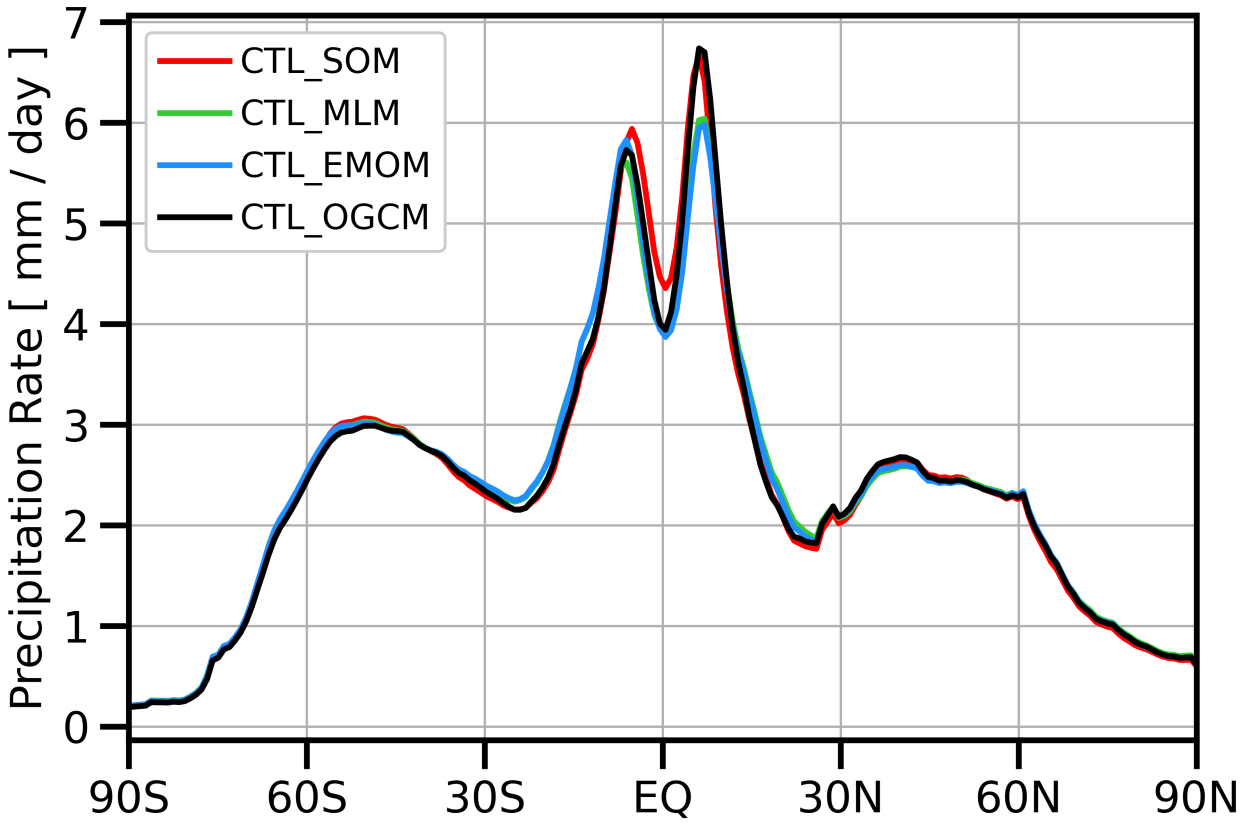

Figure 2.S5: The zonal mean of the annually-averaged precipitation for the CTL run.

Figure 2.S6: The blue shading shows the regions where the annual mean sea-ice thickness is greater than 1 m in control run. The red shading is the same but with data derived from RCP 8.5 year 2081–2100 of CMIP5.

Chapter 3

The Effect of the Active Ocean on the Tropical Rainfall Response to Global Warming

3.1 Introduction

Under global warming, climate models project that the intertropical convergence zone (ITCZ) will contract equatorward (e.g. Lau and K.-M. Kim, 2015; Byrne and T. Schneider, 2016b; Zhou et al., 2019), known as the deep-tropical contraction. The change in the tropical convection pattern will change the mean climate state and its variability (Fang and J.-Y. Yu, 2020; Yun et al., 2021), resulting in a tropical forcing, which may impact the extra-tropical regions through atmospheric teleconnections (M. A. Alexander, Bladé, et al., 2002; S.-I. Shin and Sardeshmukh, 2011; M. Newman et al., 2016). Since the tropical rainfall response to global warming still has large variations across climate models (Ma and Xie, 2013; Long et al., 2016; Byrne, Pendergrass, et al., 2018), it is important to improve our physical un-

derstanding of the underlying processes. In particular, we focus on the air-sea coupling that contributes to the deep-tropical contraction.

The physical mechanism of the deep-tropical contraction is associated with the sharpening of the meridional moist static energy gradient (Neelin et al., 2003; Byrne and T. Schneider, 2016a; Byrne and T. Schneider, 2016b; Byrne, Pendergrass, et al., 2018). Since the sea-surface temperature (SST) controls the distribution of moist static energy in the tropics, the enhanced equatorial warming (EEW) of the SST is also an important factor that drives the deep-tropical contraction (Huang, Xie, et al., 2013; Zhou et al., 2019). The key ocean process that contributes to EEW associated with the weakening of the Walker circulation is identified as the reduced oceanic equatorial upwelling (e.g. Vecchi and Soden, 2007; Chemke and Polvani, 2018). However, to what extent the changes in the ocean circulation modulate the response of tropical precipitation and circulation is not clear and this issue is addressed here.

The hierarchy of ocean models developed in chapter 2 is a great tool to test the effect of the wind-driven oceanic Ekman flow, which dominates the tropical ocean heat transport (Klinger and Marotzke, 2000), on the rainfall pattern. However, use of the simplified models in the hierarchy is hindered by the fact that the Atlantic meridional overturning circulation (AMOC) greatly modulates the tropical response in an atmospheric model that is coupled to an OGCM. This is due to the significant response in heat transport to anomalous freshwater flux in the OGCM. The modulation of AMOC will generate a notable difference between the EMOM and the OGCM. in SST and atmospheric circulation between the EMOM and OGCM such that we will not be able to verify how realistic our hierarchy is. The hierarchy is most useful in studies when the response of AMOC has reached quasi-equilibrium.

We will explore experiments with the hierarchy where the climate forcing is the abrupt quadrupling of atmospheric CO_2. In this chapter, we conduct such an experiment using OGCM and find that the AMOC collapses in the first 300 years and recovers to its original strength

by the end of 500 years. The AMOC collapse and subsequent recovery has been reported previously (e.g. Rind et al., 2018). This phenomenon results from the anomalous freshwater due to the warming gradually reducing in time and thus the meridional buoyancy gradient in the ocean gradually restores. The restored meridional buoyancy gradient re-intensifies the AMOC. Once the AMOC recovers, its modulation on heat transport is significantly reduced, allowing us to compare the outcome of OGCM with EMOM to verify whether the Ekman flow is sufficient to capture the tropical response.

In this chapter, we will perform the first attempt to study the tropical climate response in a hierarchy of ocean models that isolates the effect of oceanic Ekman flow. We will show that the inclusion of Ekman flow allows the model to reproduce the tropical response as simulated in OGCM while the response is sensitive to the prescribed depth of the Ekman layer and to the subsurface diffusivity. Moreover, we will show that at the equator, the warming caused by the Ekman flow associated with the friction is equal to or greater than the ocean warming caused by the traditional Ekman flow.

This chapter is structured as follows: In section 3.2, we briefly introduce the hierarchy of ocean models, the definition of the oceanic rotational and frictional Ekman flows, and the experimental design. In section 3.3, we present the results of our experiments and a discussion of the results. In section 3.4, we draw the conclusions.

3.2 Methods

3.2.1 Hierarchy of ocean models within the CESM1 framework

The hierarchy of ocean models was presented in chapter 2. It is unique in that it fits within the CEMS1 framework such that the Parallel Ocean Program vs 2 (POP2; R. Smith

et al., 2010), the full ocean global climate model within CESM1, sits at the top of the ocean hierarchy, followed by three other successively more simplified ocean models: the Ekman mixed-layer model (EMOM), the mixed-layer model (MLM) and the slab ocean model (SOM). Each ocean model in the hierarchy can be substituted into the CESM framework and run coupled to the other component models of the CESM1 (e.g., the atmosphere and sea-ice models).

Briefly, the lowest model in the hierarchy, the SOM, has a single slab of ocean mixed layer with a thickness that varies in the horizontal but remains constant in time. The SOM does not have any entrainment nor oceanic flow. The MLM takes a step further than SOM by allowing the mixed-layer thickness to vary temporally and follow annually prescribed values. This allows the MLM to resolve seasonal entrainment-detrainment. The EMOM builds on the lower models and adds interactive Ekman transport on top of the MLM. The EMOM assigns a fixed thickness to both the Ekman transport layer and the layer representing the Ekman return flow. Finally, the POP2 is a full ocean general circulation model (OGCM) of CESM1, representing the most realistic ocean of the hierarchy. The details of the hierarchy formulation are illustrated in Section 2 of Chapter 2.

3.2.2 Ekman flow parameterization

The parameterization of total Ekman mass transport $\vec{M}_{\mathrm{EK}}$ in the hierarchy has the form

$$\vec{M}_{\mathrm{EK}} = \vec{M}_f + \vec{M}_\epsilon \tag{3.1}$$

with

$$\vec{M}_f = \frac{f}{f^2 + \epsilon^2} (\tau^y, -\tau^x) \tag{3.2}$$

$$\vec{M}_\epsilon = \frac{\epsilon}{f^2 + \epsilon^2} (\tau^x, \tau^y) \tag{3.3}$$

where $\vec{M}_f$ is the rotational Ekman mass transport associated with the rotational Ekman flow, $\vec{M}_\epsilon$ is the frictional Ekman mass transport associated with the frictional Ekman flow, f is the Coriolis parameter, ϵ is the Rayleigh friction coefficient, τ^x and τ^y are the zonal and meridional wind stress, respectively. Positive values of τ^x mean that the wind is blowing eastward and for τ^y northward. The frictional Ekman mass transport $\vec{M}_\epsilon$ is along the wind stress. The rotational Ekman mass transport $\vec{M}_f$ is 90 degrees to the right (left) of the wind stress in the northern (southern) hemisphere. The $\vec{M}_f$ is essentially the traditional wind-driven Ekman mass transport if $\epsilon \ll f$. Notice that at the equator $\vec{M}_f = 0$ and $\vec{M}_\epsilon$ accounts for all the Ekman mass transport $\vec{M}_{\text{EK}}$. In EMOM, the $\vec{M}_{\text{EK}}$ happens within the top 50 m of the ocean, defined as the Ekman layer. The parameterization puts the layer with the return flow (thickness of 353.7 m) immediately below the Ekman layer. The return flow mass transport $\vec{M}_{\text{RF}}$ is of equal magnitude but opposite direction to the $\vec{M}_{\text{EK}}$, that is, $\vec{M}_{\text{RF}} := -\vec{M}_{\text{EK}}$ so that there is no net accumulation of water mass in each individual water column.

3.2.3 Experimental design

We conduct two sets of experiments. The first one is the pre-industrial control run (PI) where the CO_2 volume mixing ratio is kept constant at 284.7 ppm. For the lower three rungs of the hierarchy members, the coupled models are run for 200 years and they reach equilibrium after 100 years (not shown). For the POP2, we use a 1000-year spin-up run of the ocean (available from NCAR) as the initial state and run the fully coupled model for

200 years. The last 30 years are used for the equilibrium climatology.

The second set of experiments is the quadruple CO_2 run (QCO2) where CO_2 volume mixing ratio is kept constant at 1138.8 ppm. We run the SOM for 200 years, MLM and EMOM for 300 years, and POP2 for 700 years to reach their equilibrium. The last 30 years are used to compute the new equilibrium climate. The evolution of the mean SST and sea-ice volume is shown in Figures 3.1a–d.

3.3 Results

3.3.1 How the ocean reaches equilibrium in the QCO2

Each model is initialized with the quadruple CO_2 concentration compared to the state from which it is initialized, leading to an adjustment process towards equilibrium. To assess the overall adjustment of the climate system, we show the time evolution of the mean SST in Figures 3.1a–b in the northern and southern hemispheres, respectively. Because the evolution of sea ice is sensitive to global energy budget, we also show the total sea-ice volume in Figures 3.1c–d as an additional diagnostic to determine whether the system reaches a quasi-equilibrium. The SOM (blue) takes less than 50 years to reach equilibrium as its ocean has the least mass. The MLM (orange) and EMOM (green) take about 200 years to reach equilibrium because the temporal variation of the mixed layer thickness increases the effective water mass interacting with the atmosphere.

The POP2 takes approximately 500 years to reach a new quasi-equilibrium (red). It appears to go through fluctuations, and the evolution is tightly associated with the changes in the AMOC. The time evolution of AMOC strength, defined as the maximum value of the streamfunction of AMOC north of 20°N and below the depth of 500 m, is shown in

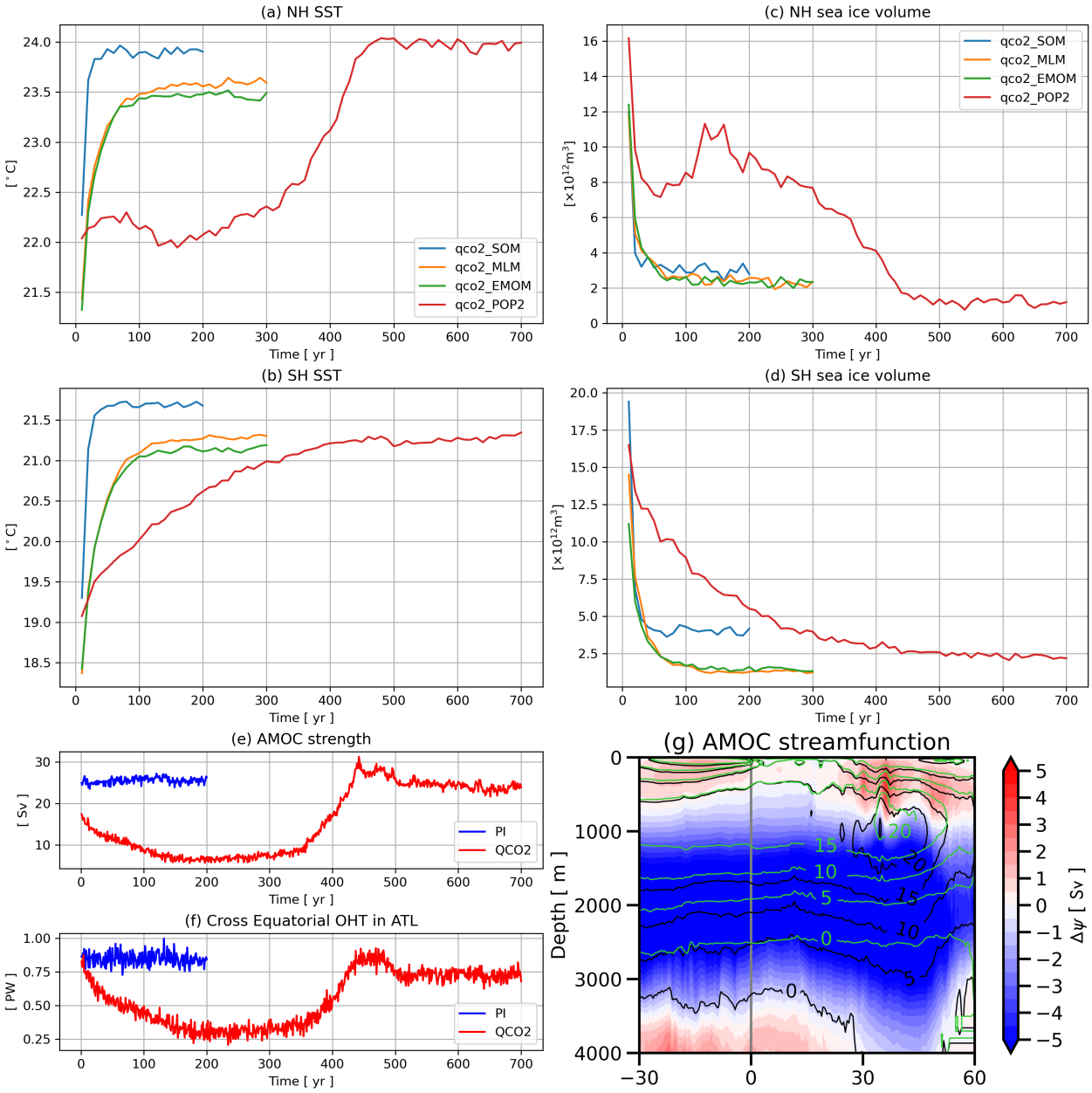

Figure 3.1: The integrated quantities of the abrupt quadruple CO_2 simulation. (a) and (b): the mean sea-surface temperatures (SSTs) of the northern hemisphere and southern hemisphere, respectively. (c) and (d): the total sea-ice volumes in the northern hemisphere and southern hemisphere, respectively. (e): the evolution of the strength of Atlantic meridional overturning circulation (AMOC) in POP2. The strength of AMOC is defined as the maximum value of the streamfunction of AMOC north of 20°N and below the depth of 500 m. The blue line is the simulation of the pre-industrial control run (PI) and the red line is the simulation of the run of quadruple CO_2 (QCO2). (f): the ocean heat transport (OHT) in the Atlantic Ocean on the equator. Color coding is the same as (e). (g): the streamfunction of AMOC of PI (black contours) and QCO2 (green contours) in depth-latitude space. The shading is the difference of the mean streamfunction of the last 30 years of each simulation, i.e., QCO2 (year 671–700) minus PI (year 171–200).

Figure 3.1e, and the cross-equatorial ocean heat transport in the Atlantic is shown in Figure 3.1f. Figure 3.1g shows the mean AMOC streamfunction for PI (in black contours), and for QCO2 averaged over years 671–700 (in green contours). The shading shows the difference in streamfunction over the last 30 years (671–700 of QCO2 minus 171–200 of PI).

In the POP2 model, the sea ice in the northern hemisphere rapidly decreases in the first 50 years as seen in Figure 3.1c. The increased anomalous freshwater flux reduces the AMOC's strength. During years 51–200, the strength of AMOC keeps decreasing (Figure 3.1e) while there is a rebound of total sea-ice volume in the northern hemisphere (Figure 3.1c). The rebound of sea ice is possibly due to the reduction of northward ocean heat transport caused by the AMOC slowdown. During years 200–350, the sea ice in the northern hemisphere steadily decreases, and the associated anomalous freshwater flux keeps the AMOC in a weakened state. During years 350–500, the northern hemisphere sea ice keeps decreasing until it reaches a total volume of approximately $1000\,\mathrm{km}^3$ (Figure 3.1c). At this point, although there is still sea ice forming in the winter, it completely melts away in the following summer, resulting in a nearly constant sea-ice volume and thus zero anomalous freshwater flux due to the sea-ice melting. Afterwards, the AMOC quickly recovers to its original strength as shown in Figure 3.1e. The initial overshooting of the AMOC strength is a transient phenomenon indicating that the AMOC is releasing the stored potential energy (Rahmstorf et al., 2005). Throughout the years 1–500, the southern hemispheric sea ice decreases exponentially to its new equilibrium as seen in Figure 3.1d. During years 501–700, the sea-ice volume remains the same while the strength of AMOC slowly decreases. During this period, although the AMOC is still adjusting, the sea ice volume and SST stabilize. Therefore, we conclude that after year 500 the system reaches a quasi-equilibrium, and we pick the year 671–700 to compute the climatology for the QCO2.

Although the AMOC recovers to its original strength, it still shoals by the end of the simulation as shown in Figure 3.1g. Moreover, if we identify the ocean heat transport of AMOC

as the cross-equatorial ocean heat transport in the Altantic, then Figure 3.1f shows that it decreases from 0.8PW to 0.3PW in the first 200 years, recovers to 0.8PW around year 450, and decreases to about 0.7PW after year 500. This demonstrates that the evolution of cross-equatorial heat transport, equivalent to inter-hemispheric heat transport, is tightly associated with the strength of AMOC. Therefore, we expect that the effect of AMOC on the surface ocean and climate reaches its peak during years 201–300 and becomes negligible after 500 years. Thus, the members with simplified ocean in the hierarchy will be informative on physical mechanisms and should be able to inform us on the POP2 simulation after year 500. Henceforth, we will show results for the response in QCO2 compared to PI over these time intervals where the climate is in equilibrium.

3.3.2 Tropical response in the Pacific Ocean

The tropical response is shown in Figure 3.2. In the SST plot, we subtract the mean of anomalous SST in the tropics to study the spatial pattern of anomalous SST easier.

In EMOM, the magnitude of increased rainfall matches to that of POP2 while the peak of the anomalous rainfall in EMOM is centered more equatorward than that of POP2. This suggests that the increased of rainfall due to dynamical coupling may be largely attributed to the oceanic Ekman response. In later paragraphs, we will argue that the details of the simulated Ekman flow are important in producing the correct location of the peak anomalous rainfall.

In POP2, the anomalous SST has a meridional cold-warm-cold tripole pattern, i.e., EEW pattern, with the warm anomalous SST along the equator in the Eastern Pacific. EMOM produces a similar enhanced tropical rainfall and SST tripole pattern. The enhanced rainfall and the SST tripole pattern in the EMOM are squeezed equatorward compared to POP2. There is also a dry response at the southern flank of the ITCZ in the EMOM that is absent

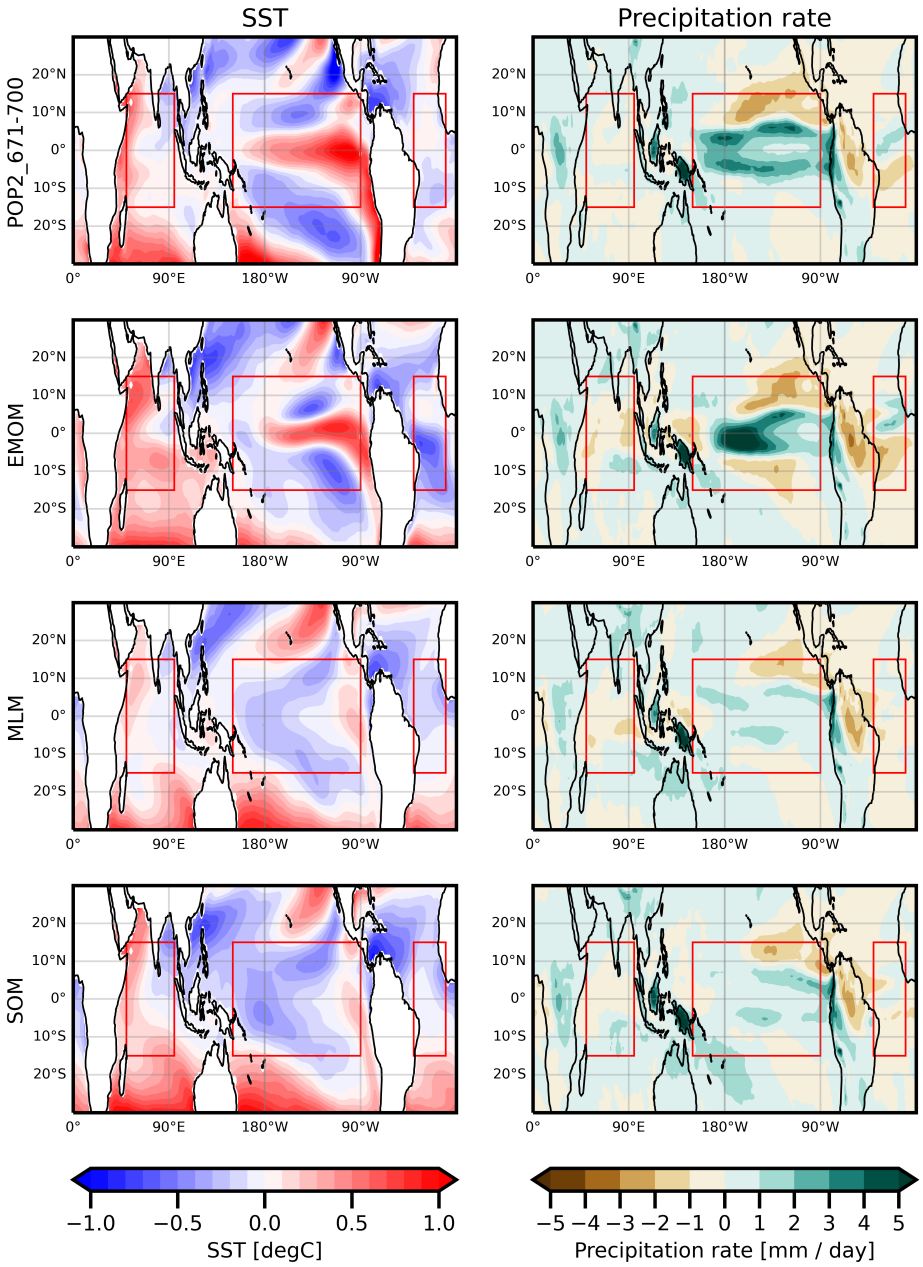

Figure 3.2: The response of quadruple CO_2 simulation of each hierarchy member. Left column shows the response of sea-surface temperature (SST). The tropical mean SST (30°S–30°N) is subtracted to show the pattern. The right column shows the response of annual mean precipitation rate. The ocean domains boxed in red will be used to compute the zonal mean quantities in Figures 3.3 and 3.4.

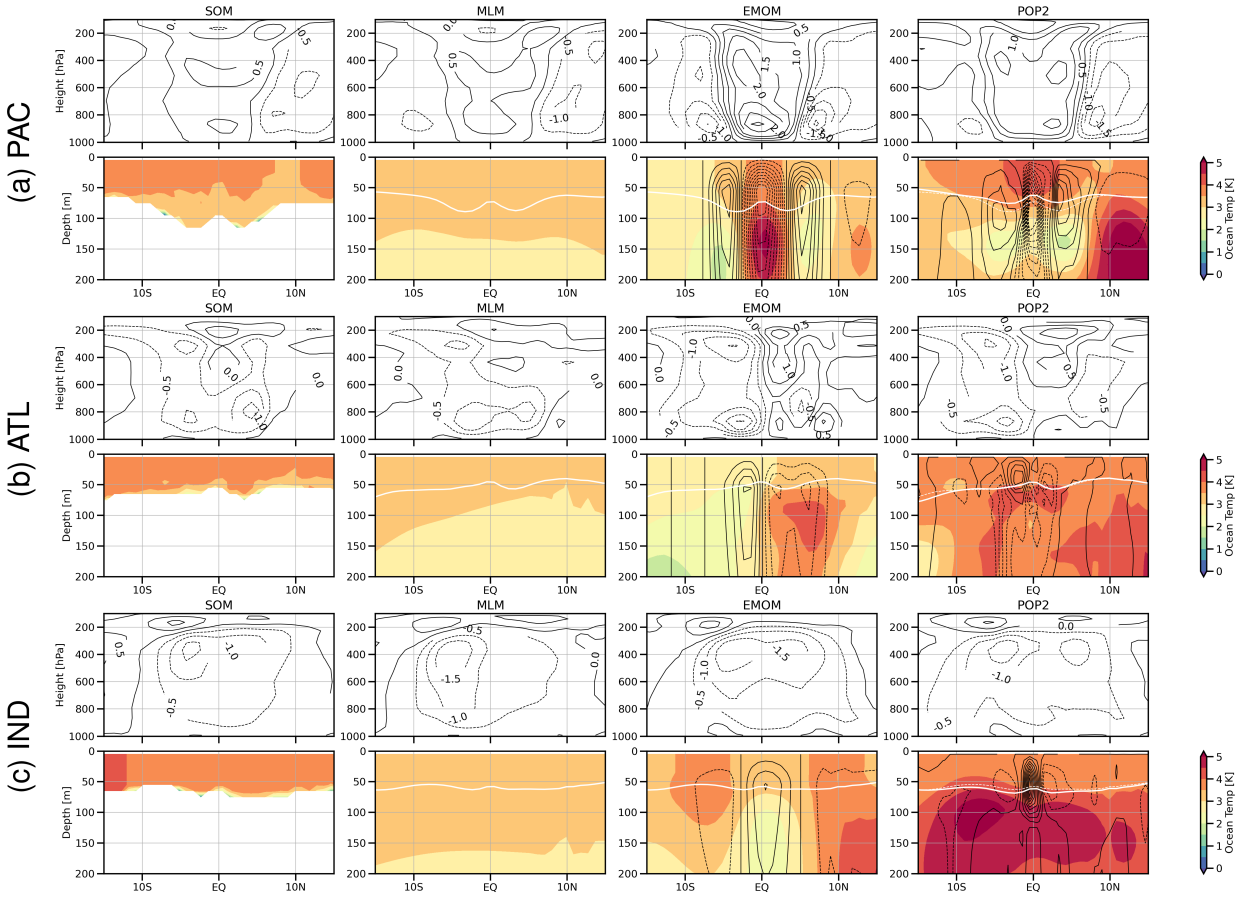

Figure 3.3: The response of atmosphere and ocean to quadruple CO_2 simulation (QCO2) in each hierarchy member over (a) Pacific Ocean, (b) Atlantic Ocean, and (c) Indian Ocean. For each pair of panels, the top panel shows the response of atmospheric vertical velocity ω with contours in the unit of Pa/s. Positive values mean upward motion and are contoured as solid lines. Negative values mean downward motion and are contoured as dashed lines. The contour intervals are 0.5 Pa/s. The bottom panel shows the response of ocean temperature (shading) and vertical velocity w with contours in the unit of m/yr. The contour intervals are 10 m/yr. The white solid and dashed lines are the annual mean mixed-layer thicknesses in the pre-industrial control run (PI) and QCO2 runs, respectively.

in POP2. In the SOM and MLM, the ITCZ is mildly enhanced and the EEW pattern is missing as the equatorial warm tongue is not present.

The response in the atmosphere is tightly connected to that of the ocean as shown in Figure 3.3, which depicts the zonally averaged response in each basin for both the atmosphere (in vertical velocity Pa/s) and the ocean (in vertical velocity m/s and temperature K). For POP2, on the far right, there is a downwelling maximum on the equator at a depth of 70 m, an upwelling maximum on the northern flank at the same depth, and an upwelling maximum on the southern depth at the depth of 110 m. The two upwelling maxima create two significant cooling regions of the ocean temperature. The equatorial downwelling does not create a warm anomaly as strong as for EMOM because the subducted heat in POP2 is transported poleward through subsurface diffusive processes that are unresolved in EMOM. The depth of the upwelling maximum north of the equator matters to the surface climate because the shallower northern oceanic upwelling drives stronger descending air motion and hence a dry response.

In EMOM, we see broadly similar oceanic vertical velocity response as in POP2 in that there is a downwelling maximum at the equator and two upwelling maxima on the poleward flanks of the equatorial region. The maxima are necessarily located at a depth of 50 m because in EMOM the Ekman flow has a constant thickness of 50 m. Similar to POP2, the two upwelling centers create cold anomalies. However, since the upwelling depths are shallower, the cold anomalies are not as significant as seen in the POP2. In EMOM, the downwelling at the equator creates a significant warming below the downwelling maximum. Unlike POP2, EMOM does not resolve the eddies that are generally diffusive. As a result, lower diffusivity preserves the warm anomaly. Since the warm anomaly is not removed, the excessive heat energy can only be taken away through air-sea exchange and therefore it triggers stronger atmospheric convection compared to POP2.

Both the anomalous zonal and meridional wind stress contributes to the oceanic vertical

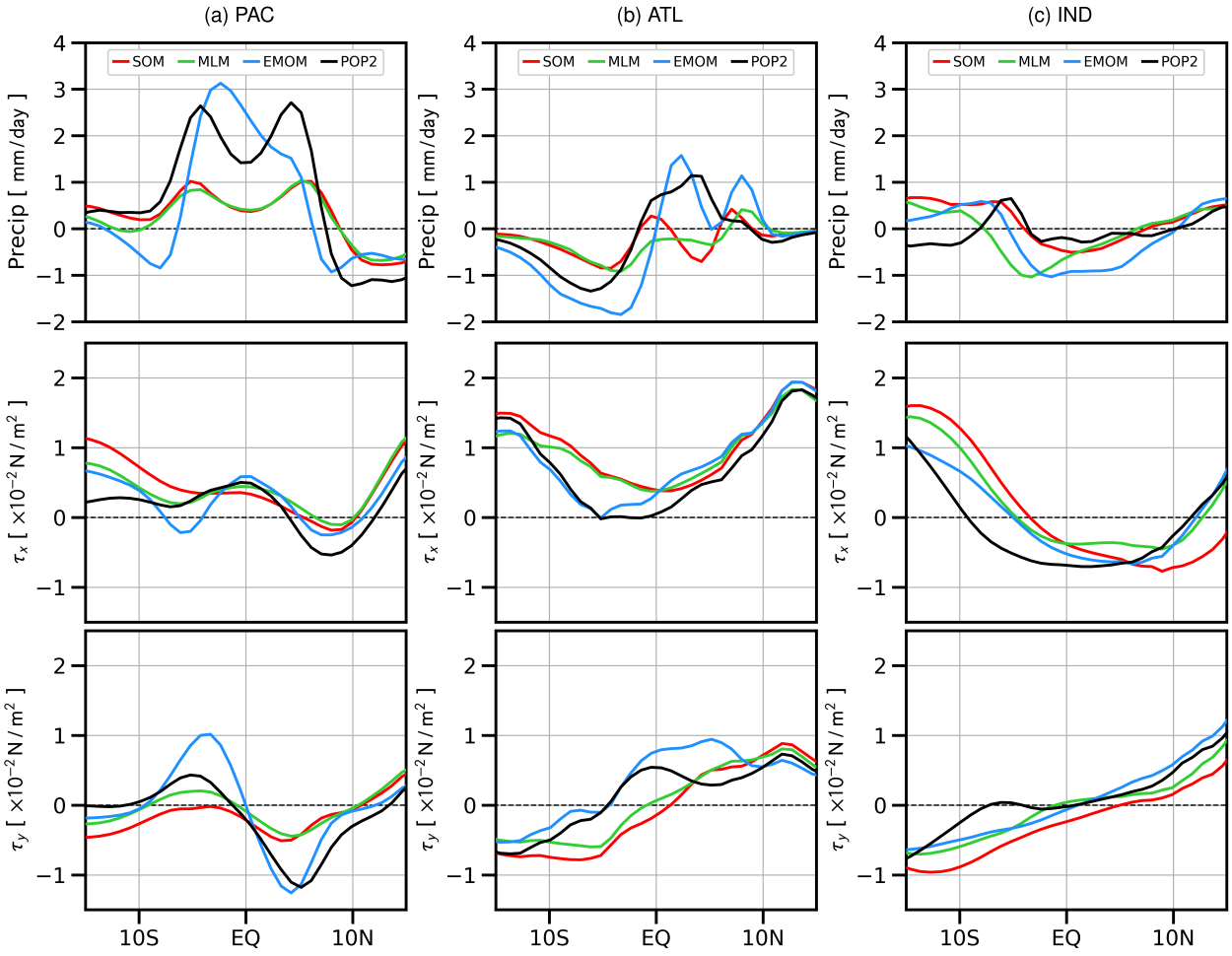

Figure 3.4: The response of atmospheric quantities to quadruple CO_2 simulation in each hierarchy member over (a) Pacific Ocean, (b) Atlantic Ocean, and (c) Indian Ocean. Top panels: the response of the zonal mean annual mean precipitation. Middle panels: the response of zonal mean zonal wind stress over the sea surface. Positive values mean the anomalous wind is blowing eastward. Bottom panels: the response of the zonal mean meridional wind stress over the sea-surface. Positive values mean the anomalous wind is blowing northward.

motions. The anomalously weakened trade winds over the equator (Figure 3.4a) generate the equatorial downwelling through the convergent rotational Ekman flow. Similarly, the anomalously convergent meridional wind induces the convergent frictional Ekman flow and therefore, the additional equatorial downwelling. Away from the equator, the upwelling motion too is generated by the divergent rotational and frictional Ekman flows. The effect of the rotational Ekman flow has been discussed in the past literature (e.g. Vecchi and Soden, 2007; Chemke and Polvani, 2018). What has received less attention is the effect of the frictional Ekman flow that acts the same direction as the rotational Ekman flow. Moreover, the ocean heat transport and convergence due to the frictional Ekman flow is equal to or stronger than those due to the rotational Ekman flow alone as seen in Figure 3.5a.

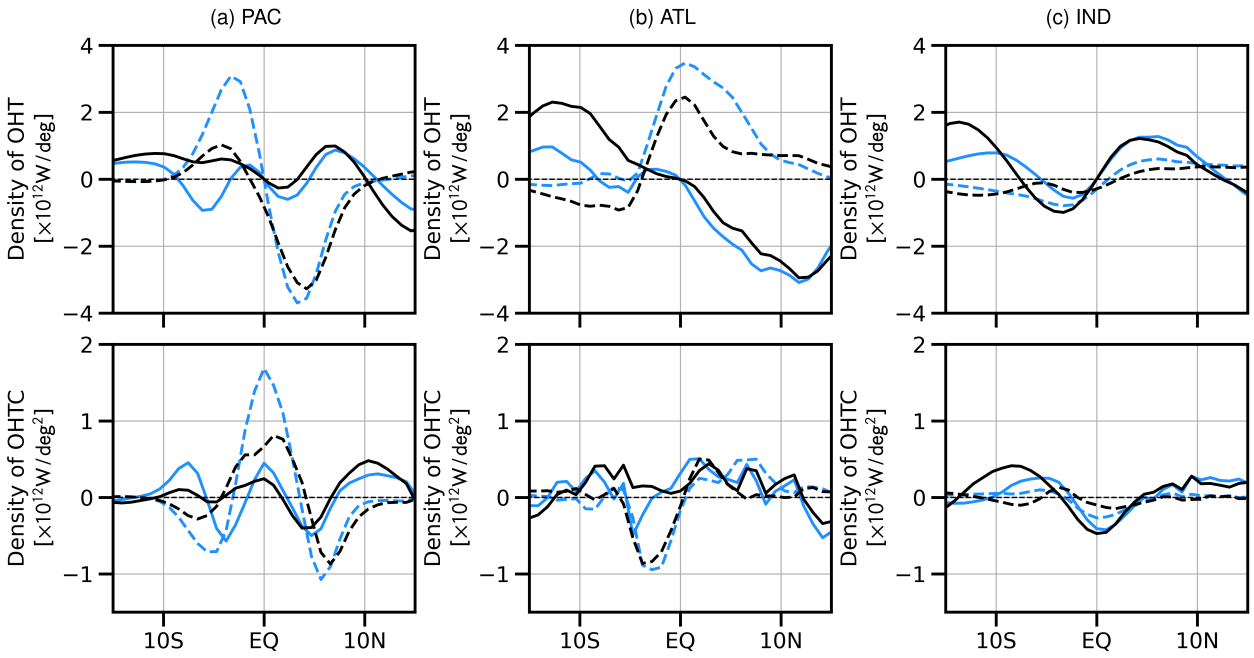

Figure 3.5: The analysis of ocean heat transport (OHT) of EMOM (blue lines) and POP2 (black lines) over (a) Pacific Ocean, (b) Atlantic Ocean, and (c) Indian Ocean. Top panels show the OHT caused by zonal mean zonal wind stresses. Solid lines are the OHT induced by the rotational Ekman flow and dashed lines are the OHT density induced by the frictional Ekman flow. Positive values means northward OHT and vice versa. Bottom panels show the density of OHT convergence (OHTC). The density of OHT and OHTC means the OHT and OHTC per degree longitude.

3.3.3 Tropical response in the Atlantic Ocean

The zonal mean analysis shows that all models have more rainfall in the northern than the southern side of the equator, showing the northward shifts of ITCZ (Figure 3.4). In POP2, there is only one precipitation change peak in the northern hemisphere while the other models have two peaks. The EMOM captures the magnitude of the anomalously positive rainfall between 0°–5°N despite the fact that there is another peak near 10°N.

In Figure 3.3, the ocean circulations of POP2 upwells near the surface in the 5°S–0° latitudinal band and downwells in the 0°–5°N latitudinal band. The upwelling branch reduces the warming of the SST and causes the descending atmospheric motion. The downwelling branch is associated with a convergent heat flux in the ocean that excites stronger atmospheric convective activity. This pair of ascending and descending air motions is strong in the atmospheric model coupled to EMOM but weak in the models coupled to the SOM and MLM, it shows that the Ekman coupling is essentially amplifying the atmospheric response.

The ascending and descending air motions to the north and south of the equator in EMOM is stronger than those in POP2 (Figure 3.3b), resulting in stronger local increase and decrease response in precipitation (Figure 3.4b). The absence of the unresolved subsurface processes in EMOM seem to intensify the meridional SST gradient. Similar to the Pacific Ocean, we speculate that the unresolved processes are diffusive, and they transport the oceanic subsurface warm anomaly produced by the downwelling motion in the northern hemisphere into the southern hemisphere. This diffusive ocean heat transport weakens the meridional SST gradient and drives less anomalous vertical air motions in POP2 than EMOM.

The ocean heat transport analysis of EMOM and POP2 (Figure 3.5) shows that the rotational and frictional Ekman flow contributes equally to the convergence of ocean heat transport in the nothern hemisphere. Surprisingly, the frictional Ekman flow contributes most of the heat convergence in the southern hemisphere because of the weak response of zonal wind

stress (Figure 3.4). This again demonstrates the importance of frictional Ekman flow at the equator.

3.3.4 Tropical response in the Indian Ocean

In the Indian Ocean, there is a reduction in the rainfall, showing the weakening of the ITCZ (Figures 3.2 and 3.3c). This response is captured by all models, suggesting ocean does not affect the qualitative change of the rainfall.

In the models coupled to SOM and MLM, they produce a descending air motion in the southern hemisphere. When the Ekman flow is included in EMOM, it generates additional descending motions in the northern hemisphere. This is because the strengthened trade wind and the increased divergent meridional wind (Figure 3.3c) drive an upwelling on the equator that cools the SST and thus induce the descending air motion.

The ocean heat transport analysis of EMOM and POP2 (Figure 3.5c) shows that the rotational Ekman flow dominates mostly in the Indian Ocean because the change in the zonal wind stress is larger than that of the meridional wind stress (Figure 3.4c). This is different from the analysis in the Pacific and Atlantic Ocean where the frictional Ekman flow can dominate the heat transport.

3.4 The role of the frictional Ekman flow

The past literature has revealed the role of the rotational Ekman flow on the the enhancement of convection along the equator through the weakening of trade winds (e.g. Vecchi and Soden, 2007; Chemke and Polvani, 2018). This is true in our simulation over the Indian Ocean. However, we find that the contribution of warming due to the convergent frictional Ekman

flow is equally important and sometimes contributes more than that of the rotational Ekman flow in the Pacific and Atlantic Oceans.

Another important aspect is that, although the contributions of frictional and rotational Ekman flows are of the same sign in our simulations, their interactions with SST will result in opposite feedbacks. If there is an anomalous equatorial SST, the stronger meridional SST gradient will drive a stronger Hadley cell. The intensified Hadley cell implies stronger trade winds that decrease the equatorial SST by inducing Ekman pumping that upwells the cold subsurface water. This causality implies a negative feedback of equatorial SST through the rotational Ekman flow. Oppositely, if there is an anomalous equatorial SST, the strengthened Hadley cell will lead to stronger convergence of meridional wind at the equator. The convergent meridional wind will drive convergent frictional Ekman flows that increases the equatorial SST by a reduction in the equatorial upwelling, and thus the SST warms further. This causality implies a positive feedback of equatorial SST through the frictional Ekman flow. Therefore, we think that correctly identifying the component of rotational and frictional Ekman flows in climate models will help us understand the SST biases in tropical oceans.

3.5 Conclusion

Understanding the mechanisms that modulate the response of tropical convection to global warming will help reduce the uncertainties in climate models. Since oceanic Ekman flow dominates the tropical ocean heat transport (Klinger and Marotzke, 2000), the air-sea Ekman coupling is invoked to explain the role of the ocean modulation. In this study, we performed the abrupt quadruple CO_2 numerical simulations across the ocean model hierarchy that can isolate the Ekman coupling to understand its modulation on the equilibrium response of tropical rainfall. Because the modulation of AMOC fades as the system reaches a new

equilibrium, it allows us to capture the surface climate response through the intermediate ocean models developed in chapter 2. In this hierarchy, the lower rungs of hierarchy do not resolve the AMOC while the top one does.

We find that, the Ekman flow coupling amplifies the rainfall response. The heat transport analysis shows that both the rotational and frictional Ekman flow induced ocean heat transport contributes, but the partition is basin dependent. Over the Pacific and Atlantic Oceans, the contribution of frictional Ekman flow of ocean heat transport is equal to, and sometimes more than that of the rotational Ekman flow. Over the Indian Ocean, the rotational component dominates. On the other hand, the modulation of Ekman over the SST response is sensitive to the structure of the Ekman-induced overturning circulation and the subsurface diffusive processes. The subsurface diffusive processes change the final meridional SST gradient, which is important to tropical circulations. In this study, we are not addressing what contributes to the asymmetry of vertical motions in the simulation of POP2, but it is an important feature of our simulation and more work should be done in understanding its physical origination.

Since the frictional Ekman flow is a convenient parameterization while the momentum diffusion is the original physical term in the governing equation, more work is required to identify such flow in observational data or OGCM output. While some pioneering work has been done in understanding the Ekman transport at the equator (Cronin and Kessler, 2009), the frictional flow was not the focus. Moreover, we think there should be more research of various aspects of frictional Ekman flow on climate dynamics such as its influence on the variability of tropical rainfall, and even on the modeled precipitation biases.

Chapter 4

Zonal Asymmetry of Freshwater Forcing as a Stability Threshold that Controls the Existence of Multiple Equilibria of Meridional Overturning Circulations

4.1 Introduction

The Atlantic Meridional Overturning Circulation (AMOC) is an essential climate component that carries 40% of the maximum ocean heat transport (Trenberth, Fasullo, Karina Von Schuckmann, et al., 2016). Numerical models show that in certain climate regimes, the overturning circulation has two stable equilibria. One is the on-state with a strong circulation that transports heat into mid-to-high latitudes in the northern hemisphere. The other is the

off-state in which the circulation is weak and has no appreciable northward heat transport (Weijer, Cheng, Drijfhout, et al., 2019). An abrupt change of the overturning circulation from an on-state to an off-state is called a shutdown, which may lead to substantial changes in the atmospheric circulation, water availability, and global food production (Vellinga and Wood, 2002; Jackson et al., 2015; Lenton et al., 2019; Zhang et al., 2019; Good et al., 2022).

Since the meridional overturning circulation is in geostrophic balance (J. Hirschi and Marotzke, 2007; Rayner et al., 2011; Sévellec and Huck, 2016), the strength of AMOC should be sensitive to changes in freshwater forcing that perturb zonal buoyancy gradients. With ongoing global warming, changes in the hydrological cycle and the loss of land ice are reshaping the freshwater forcing significantly, raising the possibility that these hydrological perturbations might trigger an AMOC shutdown by pushing the system across the stability thresholds that separate the regimes of multiple equilibria where both the on-state and off-state exist to regimes where off-state is the only equilibrium. However, there are still considerable uncertainties in estimating the stability thresholds in the context of the current climate (Weijer, Cheng, Drijfhout, et al., 2019). Therefore, exploring the stability thresholds with respect to the detail of the freshwater forcing will help us to improve the estimate of where the present AMOC resides in parameter space.

The physical mechanism for producing multiple equilibria of the overturning circulation is the salt-advection feedback (e.g., Johnson et al., 2019; Weijer, Cheng, Drijfhout, et al., 2019). The mechanism works as follows: An anomalous overturning circulation will lead to a stronger northward salt transport, and thus a stronger meridional buoyancy gradient. This stronger meridional buoyancy gradient further enhances the strength of the overturning circulation, which completes the positive feedback loop. An initial perturbation of high-latitudes freshwater flux weakens the overturning circulation, which is then amplified by the salt-advection feedback. If the amplification is strong enough, a shutdown may occur. However, because the overturning circulation is sensitive to zonal buoyancy gradients, its initial

weakening, or even strengthening, in response to the freshwater flux perturbation, depends on the zonal location of the forcing. For example, if the freshwater forcing is located on the western boundary, the forcing will produce an anomalously negative zonal buoyancy gradient, weakening the overturning circulation in addition to the reduced meridional buoyancy gradient, and increasing the likelihood of shutdown. Conversely, if the freshwater forcing is located on the eastern boundary, the forcing will create an anomalously positive zonal buoyancy gradient. This strengthens the overturning circulation and reduces the chance of a shutdown. Therefore, the zonal asymmetry of freshwater forcing is relevant to locating the state of overturning circulation in parameter space.

Indeed, there is evidence showing that the zonal distribution of freshwater forcing is a possible stability threshold. Dijkstra and Weijer (2003) studied the multiple equilibria of AMOC in an oceanic general circulation model (OGCM) coupled with an energy balanced atmospheric model. They separated the freshwater forcing into a global time-mean hydrological forcing, $\overline{\gamma}$ (they name it γ), and a localized anomaly, γ' (they name it γ_p). The localized anomaly γ' is located on the western side of the North Atlantic (24°W–60°W, 54°N–66°N) that mimics the freshwater input due to the loss of the Greenland ice sheet. They plotted the bifurcation diagram showing the multiple equilibria of the overturning circulation as a function of $\overline{\gamma}$ for various values of γ'. They found that the existence of the multiple equilibria depends on the value of γ'.

In the present study, we numerically investigate the effect of a zonally asymmetric high-latitude hydrological forcing on the existence of the multiple equilibria of the overturning circulation. The numerical models that have been used to study the multiple equilibria of the meridional overturning circulation range from box models (e.g. Stommel, 1961; Cessi, 1994; S.-K. Kim et al., 2022), zonally averaged models (e.g. Jochem Marotzke et al., 1988; Stocker et al., 1992; Vellinga, 1996; Dijkstra and MOLEMAKER, 1997; Sévellec and Fedorov, 2011), self-consistent geostrophic-force-balance model (Callies and Marotzke, 2012) to OGCMs (e.g.

Frank Bryan, 1986; Dijkstra and Weijer, 2003; R. S. Smith and Gregory, 2009; Roche et al., 2010). Ideally, we would use an OGCM for its realism. However, the parameter spaces of the OGCM are too complicated for us to study thoroughly and the computational cost is high. Therefore, we conduct our study by extending the self-consistent geostrophic-force-balance model of Callies and Marotzke (2012) to include the effects of temperature and salinity on buoyancy.

The self-consistent geostrophic-force-balance model has two meridional slabs situated on the eastern and western sides of the basin. It can therefore explicitly simulate the zonal buoyancy gradient, which is a major advantage compared to zonally averaged models that have to parameterize the relationship between the meridional and zonal buoyancy gradients. Thus, unlike the zonally averaged models, the self-consistent geostrophic-force-balance model can be used to impose the zonal asymmetric hydrological forcing in a natural way. Hereafter, we name this extended model ZATOM — the Zonally Averaged Two-slabs Ocean Model. ZATOM is appropriate for our study because it is relatively easy to elucidate the dynamics compared to OGCMs, and it does not assume the relationship between the meridional and zonal buoyancy gradients as in zonally averaged models (e.g. Stocker et al., 1992). For simplicity, the domain is restricted to a single hemisphere.

We will use ZATOM to perform numerical bifurcation analysis over two parameters through the pseudo arc-length continuation method (Seydel, 2009). The first parameter is the hydrological forcing γ that represents the freshwater forcing due to global moisture transport. The second parameter is the zonal asymmetry of freshwater forcing γ, which measures the zonal moisture transport within the ocean basin. We will find ξ controls the location of tipping point at which a small increase of γ causes a shutdown of the overturning circulation. Further processing the bifurcation curves, we will present the regime diagram that shows the parameter space allowing the existence of multiple equilibria.

Using the insight gained from ZATOM, we will extend Stommel two-box model (Stommel,

1961) to include the effect of zonal asymmetry of freshwater forcing over the overturning circulation. The Stommel two-box model is frequently invoked to understand the multiple equilibria of the overturning circulation. The model has two stable equilibria, thermal and haline modes, are identified. The strong circulation in the thermal mode is driven by the temperature gradient and is identified as the on-state. On the other hand, the weak and reversed circulation in the haline mode is driven by salinity and is identified as the off-state. Most importantly, the Stommel two-box model parameterizes the strength of overturning circulation as a function of meridional buoyancy gradient. In the extended two-box model, we modify this parameterization by considering the modulation of zonal asymmetric freshwater forcing. The extended two-box model allows us to physically understand the vanishing of the multiple equilibria in strong zonal asymmetric freshwater forcing in ZATOM as the suppression of either the thermal or the haline mode.

The paper is structured as follows: in Section 2 we introduce the formulation of ZATOM and the extended two-box model, and the continuation method; in Section 3 we illustrate the spin-up process of ZATOM with a thought experiment; in Section 4 we present the result and discussion; in Section 5 we draw the conclusion. Most importantly, we will show that zonal asymmetry of freshwater forcing ξ is a stability threshold that determines the existence of multiple equilibria.

4.2 Methods

4.2.1 Zonally Averaged Two-slabs Ocean Model (ZATOM)

Before formulating the model, we first illustrate the essential dynamics that drives the meridional overturning circulation. Consider a single hemispheric ocean basin that is bounded in both meridional and latitudinal directions. The hydrostatically and geostrophically balanced

incompressible ocean satisfies

$$f\hat{k} \times \frac{\partial \vec{v}_H}{\partial z} = -\nabla_H b, \tag{4.1a}$$

$$\nabla \cdot \vec{v} = 0, \tag{4.1b}$$

where $\vec{v}_H$ is the horizontal velocity vector, $\vec{v}$ is the total velocity vector, ∇ is the divergence operator, ∇_H is the horizontal gradient operator, $\hat{k}$ is a unit vector pointing upward, and $f = 2\Omega \sin\phi$ is the Coriolis parameter with ϕ denoting the latitude and Ω the Earth's rotation rate. The geostrophic balance (4.1a) is satisfied away from the boundary of the ocean. The boundary flow are determined by satisfying the continuity (4.1b). The zonally integrated thermal wind balance of meridional velocity is

$$\frac{\partial V}{\partial z} = \frac{b_e - b_w}{f} \tag{4.2}$$

where V is the zonally integrated velocity, b_e and b_w are the buoyancy on the eastern and western boundaries. Further using the streamfunction ψ of the meridional overturning circulation defined through continuity with $V = -\partial\psi/\partial z$, we have

$$\frac{\partial^2 \psi}{\partial z^2} = -\frac{b_e - b_w}{f}. \tag{4.3}$$

That is, the positive buoyancy gradient $b_e - b_w > 0$ drives a positive meridional overturning circulation whose upper branch flows northward (southward) if it is in the northern (southern) hemisphere. The meridional overturning circulation is westerly intensified due to the westward propagation of Rossby wave that concentrates the buoyancy anomalies onto the western boundary.

We initialize a zonally symmetric stratified ocean in which the most buoyant water is at the tropical surface and is less buoyant poleward and downward (Figure 4.1a). Then, since the

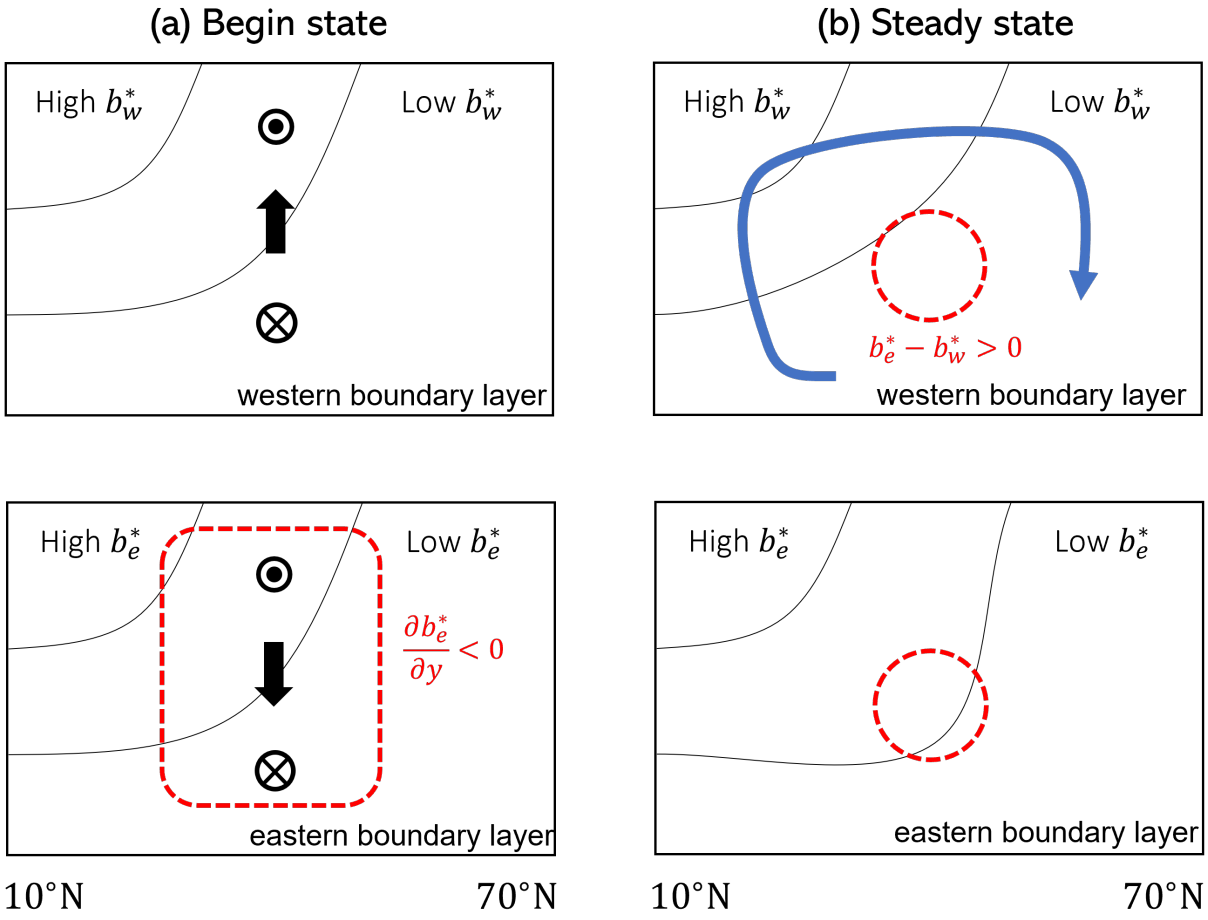

Figure 4.1: Cartoon explaining the thought experiment to understand the overturning circulation dynamics. The solid contour lines are the isobuoyancy surfaces. (a) shows the initial state where the buoyancy is zonally symmetric and the seawater gets denser as we move northward and downward. as begin the thought experiment with the most buoyant water located in the tropical surface. Because $b_e = b_w$, by equation (4.3) there is no meridional overturning circulation. The arrows shows the boundary vertical motion driven by the zonal geostrophic flow. (b) shows the system state after it evolves for some time. The zonal overturning circulation advects the surface buoyant water downward in the eastern boundary layer and subsurface dense water upward. The opposite vertical motions creates a patch within which $b_e - b_w > 0$. Meanwhile, the warm salty ocean advected from the tropics cools in the western boundary layer and starts convective mixing downward, which helps to produce even larger $b_e - b_w$. Because $b_e - b_w > 0$, a positive meridional overturning circulation is implied by equation (4.3). Notice that the zonal overturning circulation still exists in (b) but is not shown for graphical clarity.

initial state is zonally symmetric, i.e., $b_e = b_w$, by equation (4.3) there is no meridional overturning circulation. Instead, there exists a surface eastward and deep westward geostrophic flows due to meridional buoyancy gradient. To satisfy the continuity, they produce a downward motion on eastern boundary and an upward motion on the western boundary which complete the zonal overturning circulation. As the system evolves, the zonal overturning circulation advects the buoyant surface water downward in the eastern boundary layer and dense subsurface water upward in the western boundary layer (Figure 4.1b). The opposite vertical motions create a region with a positive zonal buoyancy difference $b_e - b_w > 0$ that drives a westerly intensified meridional overturning circulation whose upper branch flows northward according to (4.3). The convective mixing further amplified the zonal buoyancy difference, triggered by the westerly intensified meridional overturning circulation that sends salt into the high latitude to form dense surface water in the western boundary. Therefore, the essential ingredients needed for meridional overturning circulation are the difference between eastern and western boundary, the existence of the zonal overturning circulation, and the convective mixing.

Now, we start formulating ZATOM by extending the two-slabs model of Callies and Marotzke (2012) to include the separate effects of temperature and salinity on the buoyancy. The updated model carries separate tracers for temperature T and salinity S from which the buoyancy is computed using a linearized equation of state,

$$b = \alpha_T T - \alpha_S S, \tag{4.4}$$

where α_T is a constant thermal expansion coefficient that converts the temperature into buoyancy, and α_S is a constant haline contraction coefficient that converts the salinity into buoyancy. As introduced earlier, the model follows hydrostatic and geostropic balances and the fluid is incompressible.

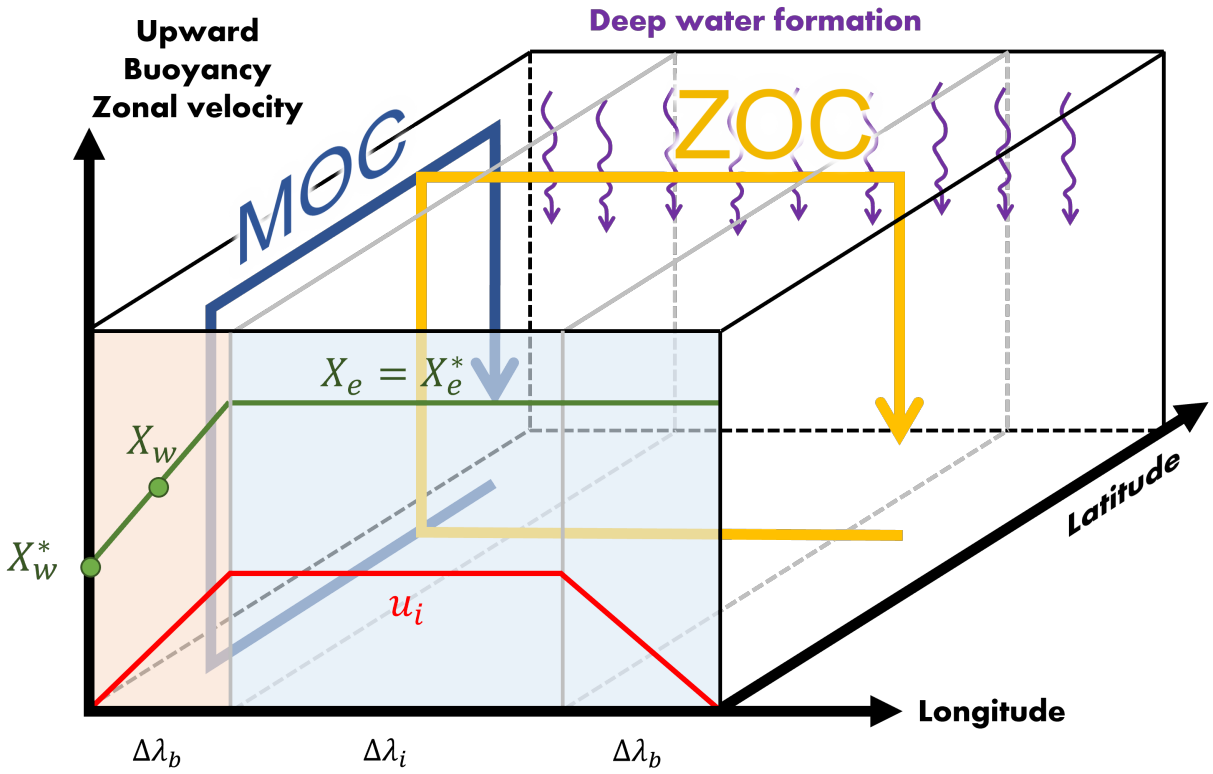

Figure 4.2: Schematic of ZATOM. The basin is divided into three regions, western boundary layer, interior ocean, and eastern boundary layer. The tracers, i.e., temperature, salinity, are zonally homogeneous across the interior ocean and eastern boundary layer with value X_e. Within the western boundary layer, the tracers linearly changes from X_e^* to X_w^*. The $X_w = (X_w^* + X_e^*)/2$ is the mean of the tracer in the western boundary layer. The quasi-geostrophic balance requires that the overturning circulation only exists in the western boundary layer. The balance also requires the zonal flow u_i to exists in the interior ocean, i.e. the ZOC. The ZOC functions as translating meridional buoyancy gradient into east-west buoyancy gradient that supports the overturning circulation (see figure 4.1).

A schematic of the model domain together with arrows indicating the directions of the zonal and meridional overturning circulations is given in Figure 4.2. The basin boundaries coincide with lines of constant longitude and latitude, so that the zonal width of the basin decreases in proportion to $\cos\phi$.

The ocean basin is divided into three meridional slabs: (i) a slab on the eastern boundary of fixed longitudinal width $\Delta\lambda_b$ in which the meridional component of the velocity, v_e vanishes, and where the divergence of the vertical velocity feeds zonal current u_i into the interior slab, (ii) an interior slab of longitudinal width $\Delta\lambda_i$ in which both the vertical and meridional

velocity components vanish leaving only the zonal velocity, and (iii) a western boundary layer with the same longitudinal width as the eastern layer, i.e. of width $\Delta\lambda_b$. The zonal velocity is zonally homogeneous in the interior ocean and decreases to zero on the domain boundaries. The temperature and salinity, and hence the buoyancy is flat across the interior ocean and eastern boundary layer due to the smoothing by Rossby waves and the anomalies are concentrated in the western boundary layer (Jochem Marotzke, 1997; Cessi and Wolfe, 2009). Therefore, the overturning circulation only exists in the western boundary layer according to thermal wind relationship (4.1a). The tracer values on the boundaries are denoted with supscript $*$, and the mean tracer values are denoted without the supscript. In ZATOM, the tracer on the eastern boundary X_e^* is the same as the mean value across the interior ocean and eastern boundary X_e, i.e. $X_e^* = X_e$. For simplicity, we will refer the domain of interior ocean and eastern boundary together as "eastern ocean" unless specified.

Apply the idea described above, the meridional and vertical velocities in the western and eastern boundary layers, v_w, w_w, v_e, and w_e, can be diagnosed. First, because overturning circulation only exists in the western boundary, $v_e = 0$. Then, the rest three velocities are diagnosed from two elliptical equations resulting from Equations (4.1a) and (4.1b) as

$$\partial_z^2 \psi = -\left(\frac{b_e^* - b_w^*}{f}\right). \tag{4.5a}$$

$$\partial_z^2 w_e = -\frac{\partial_y b_e^*}{f L_b} \tag{4.5b}$$

where the w_e is the vertical velocity in the eastern boundary layer, L_w is the width of the boundary layer, ∂_y and ∂_z are the gradient operators in the meridional and vertical directions, respectively. The ψ is the streamfunction that satisfies

$$L_w \left(v_w, w_w + w_e\right) = \left(-\partial_z \psi, \partial_y \psi\right). \tag{4.6}$$

The temperature and salinity evolves through the following equations,

$$\frac{\partial T}{\partial t} = -\vec{v}\cdot\nabla T + K_V\partial_z^2 T + K_H\nabla_H^2 T + q_T + F_T, \tag{4.7}$$

$$\frac{\partial S}{\partial t} = -\vec{v}\cdot\nabla S + K_V\partial_z^2 S + K_H\nabla_H^2 S + q_S + F_S, \tag{4.8}$$

where T is temperature, S is salinity, K_V is the vertical diffusivity, K_H is the horizontal diffusivity, q_T and q_S are the convective adjustments. The F_T and F_S are the forcing terms used to introduce the atmospheric forcing. Meanwhile, the freshwater is removed from the tropics and precipitates into higher latitudes. ZATOM mimics these through adding forcing terms only at the surface for temperature and salinity within the depth H_T and H_S in analogy to the mixed layer. Later we will use step function

$$\Theta_H(z) = \begin{cases} 1 & \text{if } z > -H, \\ 0 & \text{if } z \le -H, \end{cases} \tag{4.9}$$

to achieve the control over the forcing. The forcing of temperature is

$$F_T = -\frac{1}{\tau_T}\left(T - T_{\text{sfc}}\right)\Theta_{H_T} \tag{4.10}$$

where τ_T is the relaxation timescale of sea-surface temperature. The forcing of salinity, which we subsequently separate into the forcing acting on the surface of western boundary layer and eastern ocean as $F_{S,w}$ and $F_{S,e}$, are

$$F_{S,w} = -S_0\gamma\left(1 - \xi'\eta\right)\sigma\frac{\Theta_{H_S}}{H_S} \tag{4.11a}$$

$$F_{S,e} = -S_0\gamma\left(1 + G\xi'\eta\right)\sigma\frac{\Theta_{H_S}}{H_S} \tag{4.11b}$$

where the γ is the total freshwater forcing (volume per unit time), S_0 is the reference salinity, $G := \Delta\lambda_b/\left(\Delta\lambda_b + \Delta\lambda_i\right)$ is the ratio of the width of the domains, ξ' is the dimensionless scalar

to control the zonal freshwater asymmetry with positive values depositing more freshwater into the eastern ocean, η is a step function

$$\eta(\phi) = \begin{cases} 1 & \text{if } \phi > \phi_c, \\ 0 & \text{if } \phi \leq \phi_c, \end{cases} \tag{4.12}$$

where ϕ_c is the latitude north of which the forcing becomes zonally asymmetric. The σ is a distribution function of γ that has the unit of per area and satisfies

$$\int \sigma \cos(\phi)\, \mathrm{d}\phi = 0 \tag{4.13a}$$

$$a^2 (2\Delta\lambda_b + \Delta\lambda_i) \int_{\sigma>0} \sigma \cos(\phi)\, \mathrm{d}\phi = 1 \tag{4.13b}$$

as we require conservation of total salinity and σ normalized. Normally, $H_T = H_S$ as mixed layer does not differentiate temperature and salinity. However, later in Section 4.3.3 we will keep H_T the same but thicken H_S to diminish the effect of stratification in the ocean surface due to the freshwater forcing. The T_{sfc} is designed as

$$T_{\text{sfc}} = T_s + \frac{T_n - T_s}{2} \left[1 + \cos\left(\frac{\pi(\phi - \phi_s)}{\phi_n - \phi_s} \right) \right], \tag{4.14}$$

is the forced sea-surface temperature where T_s and T_n are the prescribed temperature on the southern and northern boundaries. The σ is chosen as

$$\sigma(\phi) = \begin{cases} \sigma_0 \tanh\left(\frac{\phi-\phi_c}{\delta}\right) & \text{if } \phi > \phi_c, \\ \sigma_0 \tanh\left(\frac{\phi-\phi_c}{\delta}\right) \frac{\int_{\phi_c}^{\phi_s} \tanh\left(\frac{\phi-\phi_c}{\delta}\right) \cos\phi \mathrm{d}\phi}{-\int_{\phi_c}^{\phi_n} \tanh\left(\frac{\phi-\phi_c}{\delta}\right) \cos\phi \mathrm{d}\phi} & \text{if } \phi \leq \phi_c, \end{cases} \tag{4.15}$$

where δ is the transition width, and σ_0 is a normalizing constant such that (4.13b) is satisfied. An forcing example is plotted in Figure 4.3a. The overall concept is illustrated in Figure 4.3b. The hydrological forcing γ transports the moisture from low to high latitude and the asymmetric freshwater forcing $\xi\gamma$ transports the moisture from western to eastern side of

the high-latitude ocean.

The detailed derivation and boundary conditions required to solve the elliptical equations and the exact tracer tendency equations are documented in Appendix 4.A. The parameters we use in this paper are listed in table 4.1.

4.2.2 Pseudo arc-length continuation method

Typical Newton's method to solve the steady state of the system failed on the bifurcation point since by definition bifurcation points are where Jacobian of the system becomes singular, on which unique solution is not guaranteed. To navigate the singularity of Jacobian matrix, an additional parameter, i.e. freshwater forcing γ or the zonal asymmetry of freshwater forcing ξ in this study, is included so that the extended Jacobian is non-singular. Such an approach is termed arc-length continuation method. The pseudo arc-length continuation method is a simplified version of arc-length continuation (Keller, 1977; Seydel, 2009). In this paper, the convergence is achieved if mean $|\partial T/\partial t| < 0.001$°C/yr and $|\partial S/\partial t| < 0.001$psu/yr.

The continuation method has been applied to geophysical problems such as the bifurcation analysis of the zonal mean overturning circulation (Vellinga, 1996; Dijkstra and MOLEMAKER, 1997), overturning circulation in ocean general circulation model (Dijkstra, Oksuzoglu, et al., 2001; Dijkstra and Weijer, 2005), and double-gyre problem (Primeau and D. Newman, 2007).

4.2.3 Extended two-box model

As in the original Stommel two-box model, the extended two-box model has a box representing high-latitude ocean and another box representing low-latitude ocean with each box having the same volume V (Figure 4.4). Each box has its own temperature and salinity.

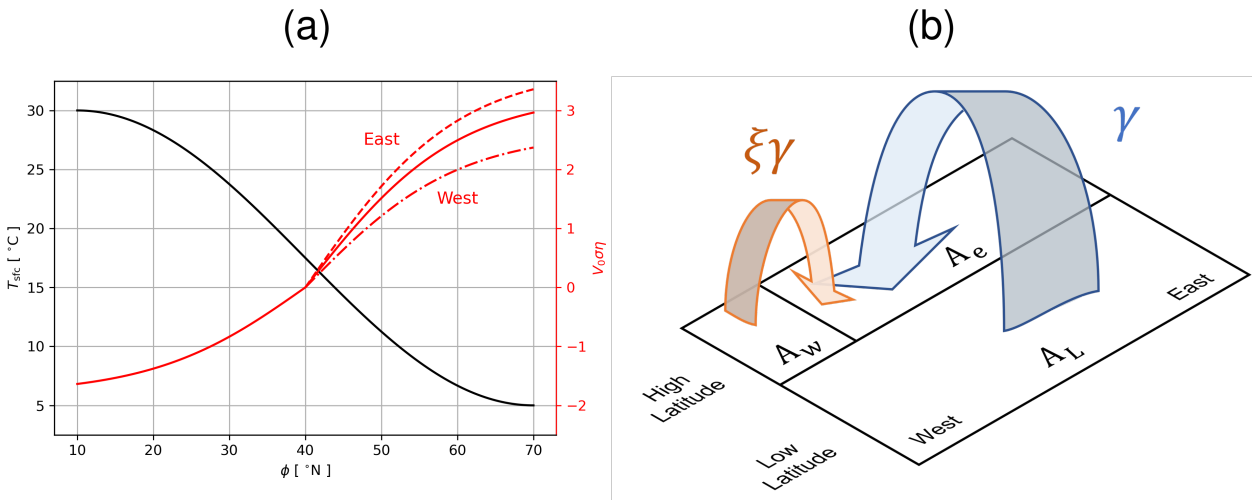

Figure 4.3: The forcing used in ZATOM. (a) The black line shows the specified sea-surface temperature T_{sfc} in (4.10). The red line is the distribution function σ of hydrological forcing in (4.11a), weighted a volume constant $A_0 := a^2\,(\Delta\lambda_i + 2\Delta\lambda_b)$. With $\xi = 0.2$, the modified forcing is plotted as dashed (eastern ocean) and dotted-dashed (western boundary layer) lines. (b) The schematic diagram showing the freshwater forcing. There are three boxes representing the Atlantic ocean: low latitude box, high latitude western box (the western boundary layer), and high latitude eastern box with surface areas A_L, A_w, and A_e. The γ is the hydrological forcing (blue arrow) transporting the freshwater from low to high latitude ocean. The $\xi\gamma$, the product of asymmetry of freshwater forcing ξ and γ, is the zonal freshwater forcing transporting moisture from western to eastern boxes.

Table 4.1: The default parameters used in ZATOM.

Parameter	Value
K_v	$1 \times 10^{-4}\,\text{m}^2/\text{s}$
K_c	$1\,\text{m}^2/\text{s}$
K_H	$4 \times 10^4\,\text{m}^2/\text{s}$
δ	$10°$
ϕ_c	$40°$
$\Delta\lambda_b$	$5°$
$\Delta\lambda_i$	$10°$
Δ_c	$1 \times 10^{-4}\,\text{m/s}^2$
H	$4500\,\text{m}$
H_{sfc}	$60\,\text{m}$
a	$6400\,\text{km}$
T_s	$25°\text{C}$
T_n	$0°\text{C}$
S_0	$35\,\text{psu}$
α_T	$2 \times 10^{-3}\,\text{m/s}^2/°\text{C}$
α_S	$7 \times 10^{-3}\,\text{m/s}^2/\text{psu}$

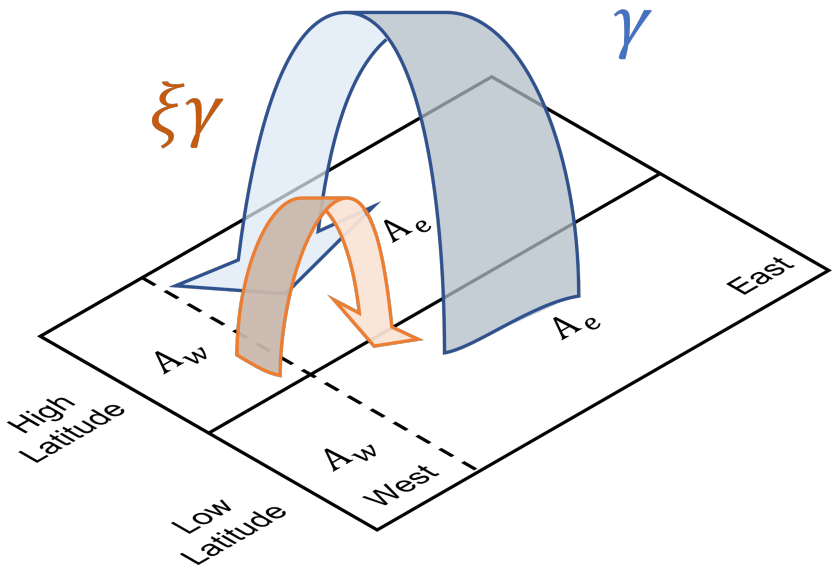

Figure 4.4: The design of extended two-box model. There is a low latitude box and a high latitude box representing the low and high latitude oceans with equal surface areas $A = A_w + A_e$ where A_w and A_e are the surface areas of the western and eastern side of the ocean separated by the dashed line. The γ is the hydrological forcing (blue arrow) transporting the freshwater from low to high latitude ocean. The $\xi\gamma$, the product of asymmetry of freshwater forcing ξ and γ, is the zonal freshwater forcing transporting moisture from western to eastern side of the ocean.

The meridional overturning circulation with strength ψ and background diffusion mixes the temperature and salinity between the boxes. Essentially, the two-box system has only two free-evolving variables: south-minus-north temperature and salinity differences denoted by δT and δS. The governing equations are

$$\frac{\mathrm{d}\delta T}{\mathrm{d}t} = -\frac{1}{t_r}\left(\delta T - \delta T^*\right) - \left(\frac{1}{t_d} + \frac{|\psi|}{V}\right)\delta T, \tag{4.16a}$$

$$\frac{\mathrm{d}\delta S}{\mathrm{d}t} = 2\frac{\gamma S_0}{V} - \left(\frac{1}{t_d} + \frac{|\psi|}{V}\right)\delta S, \tag{4.16b}$$

where t_r is the restoring timescale of temperature, t_d is the timescale of background diffusion, δT^* is the temperature difference due to atmosphere forcing, S_0 is the reference salinity, γ is the freshwater forcing. The strength of overturning circulation ψ is assumed to be proportional to the mean east-west buoyancy difference Δb, the buoyancy difference between the boxes divided by a dashed line in Figure 4.4. Following the understanding of the dynamics illustrated in the beginning of Section 4.2.1, there are two sources and one sink of Δb. One source is the tilting of isopycnal surfaces by the zonal overturning circulation. Another source is the direction contribution from the zonal asymmetry of freshwater forcing. The sink is all other unresolved mixing processes that removes Δb with a timescale $t_{\Delta b}$. The resulting tendency equation of Δb is

$$\frac{\partial \Delta b}{\partial t} = \mu' \delta b + \frac{2\alpha_S S_0 \gamma \xi}{V}\left(1 + G\right) - \frac{\Delta b}{t_{\Delta b}} \tag{4.17}$$

where δb is the south-minus-north buoyancy difference, ξ is the zonal asymmetry of freshwater forcing whose product with γ, i.e. $\xi\gamma$, is the zonal freshwater forcing that transport the freshwater zonally, and

$$G = \frac{1}{2}\left(\frac{A_e}{2A_w} + \frac{A_w}{2A_e} - 1\right) \geq 0 \tag{4.18}$$

is the geometric factor that changes the efficiency of the generation of Δb given the same γ. The μ' is the sensitivity of the generation rate of the east-west buoyancy difference to meridional buoyancy difference. Essentially, μ' represents the stratification of the ocean and δb represents the strength of zonal overturning circulation that tilts the isopycnal layers to produce zonal buoyancy gradients. The geometric factor is zero only if east and west box have the same size, i.e., $A_e = A_w$. In the case of our design in ZATOM, $A_e = 3A_w$, thus $G = 1/3$. Then, we make two assumptions to obtain a parameterization of ψ. One assumption is that Δb is in fast equilibrium, meaning $\partial \Delta b/\partial t \approx 0$. Another assumption is that $\Psi = c\Delta b$ where c is a proportional constant, as suggested by (4.61b) in ZATOM. Thus, we can rearrange the Equation (4.17) as

$$\psi = ct_{\Delta b}\mu' \left(\alpha_T \delta T - \alpha_S \delta S\right) + \frac{ct_{\Delta b}\alpha_S S_0}{V}\gamma\xi \tag{4.19}$$

To reduce the We introduce the following parameters to non-dimensionalize the governing equations,

$$t = t_d \tau, \tag{4.20a}$$

$$\delta T = \delta T^* x, \tag{4.20b}$$

$$\delta S = \frac{\alpha_T \delta T^*}{\alpha_S} y, \tag{4.20c}$$

$$\gamma = \frac{\alpha_T \delta T^* V}{2\alpha_S t_d S_0 \left(1+G\right)} p, \tag{4.20d}$$

$$\psi = \frac{V}{t_d}\Psi, \tag{4.20e}$$

$$Q = \frac{t_d}{t_R}, \tag{4.20f}$$

$$\mu = \frac{ct_{\Delta b}\mu'\alpha_T \delta T^* t_d}{V}, \tag{4.20g}$$

$$\nu = \frac{ct_{\Delta b}\alpha_T \delta T^*}{V}. \tag{4.20h}$$

where τ, x, y, p, and Ψ are the non-dimensionalized t, δT, δS, γ, and ψ, respectively. The Q

is the ratio of the horizontal diffusion and restoring timescale. The μ and ν are the generation efficiency of overturning circulation given a unit of meridional buoyancy difference and a unit of zonal freshwater forcing, respectively. The non-dimensionalized system is

$$\frac{\mathrm{d}x}{\mathrm{d}\tau} = -Q\,(x-1) - (1+|\Psi|)\,x \tag{4.21a}$$

$$\frac{\mathrm{d}y}{\mathrm{d}\tau} = p - (1+|\Psi|)\,y \tag{4.21b}$$

with the non-dimensionalized strength of overturning circulation Ψ

$$\Psi = \mu\,(x-y) + \nu p \xi \tag{4.22}$$

4.3 Result

To understand how the zonal asymmetry of freshwater forcing impacts the existence of multiple equilibria, we carry out the bifurcation analysis of ZATOM in Section 4.3.2. Then, in Section 4.3.2 we introduce the extended two-box model and derive its bifurcation diagram In Section 4.3.3, we discuss the difference of bifurcation between ZATOM and the extended two-box model. Finally in Section 4.3.4, we discuss the implication of our finding and its linkage to the Dijkstra and Weijer (2003).

4.3.1 The bifurcation diagrams of ZATOM

The bifurcation diagram of the mean strength of overturning circulation $\langle\psi\rangle$ is plotted in Figure 4.5a where the bracket is defined as

$$\langle\,\cdot\,\rangle = \frac{1}{(\sin\phi_n - \sin\phi_s)\,H^*}\int_{-H^*}^{0}\int_{\phi_s}^{\phi_n}(\cdot)\cos\phi\mathrm{d}\phi\,\mathrm{d}z \tag{4.23}$$

with $H^* = 1000\,\mathrm{m}$. We choose five values of zonal asymmetry of freshwater forcing ξ' to demonstrate its modulation over the regime of multiple equilibria. Furthermore, by comparing Figure 4.5a and 4.5b we see that the mean overturning circulation strength $\langle\psi\rangle$ is closely related to the mean east-west buoyancy difference. Thus, we should be able to understand the behavior of $\langle\psi\rangle$ through understanding $\langle b_e^* - b_w^*\rangle$.

In Appendix 4.B, we derive a diagnostic relationship of $b_e^* - b_w^*$ of ZATOM (same as Equation (4.69))

$$\langle b_e^* - b_w^*\rangle = c_1 \langle\chi\rangle \left\langle \partial_z \bar{b} \right\rangle + c_2 \Delta\tilde{q} + c_3 \xi' \gamma. \tag{4.24}$$

where $\partial_z \bar{b}$ is the zonally mean stratification, $\Delta\tilde{q}$ is the east-west convective mixing fraction difference, and c_1, c_2 and c_3 are the constants. A convenient form is to take the finite difference of the equation

$$\delta \langle b_e^* - b_w^*\rangle = c_1 \delta \left(\left\langle \partial_z \bar{b} \right\rangle \langle\chi\rangle \right) + c_2 \delta \left(\Delta\tilde{q}\right) + c_3 \xi' \delta\gamma. \tag{4.25}$$

The equation allows us to understand the changes of steady states of the overturning circulation into: the direct contribution of the zonal overturning circulation that acts on the stratification, the contribution of the east-west convective mixing difference, and the contribution of the asymmetric freshwater forcing. If the change of state is small enough, then

$$\delta \left(\left\langle \partial_z \bar{b} \right\rangle \langle\chi\rangle \right) \approx \left\langle \partial_z \bar{b} \right\rangle \delta \langle\chi\rangle + \langle\chi\rangle \, \delta \left\langle \partial_z \bar{b} \right\rangle. \tag{4.26}$$

can use the diagnostic relation (4.24) to obtain physical understanding of the bifurcation of overturning circulation $\langle\psi\rangle$.

To understand the behavior of the solution branch as a function of γ, we plot the bifurcation

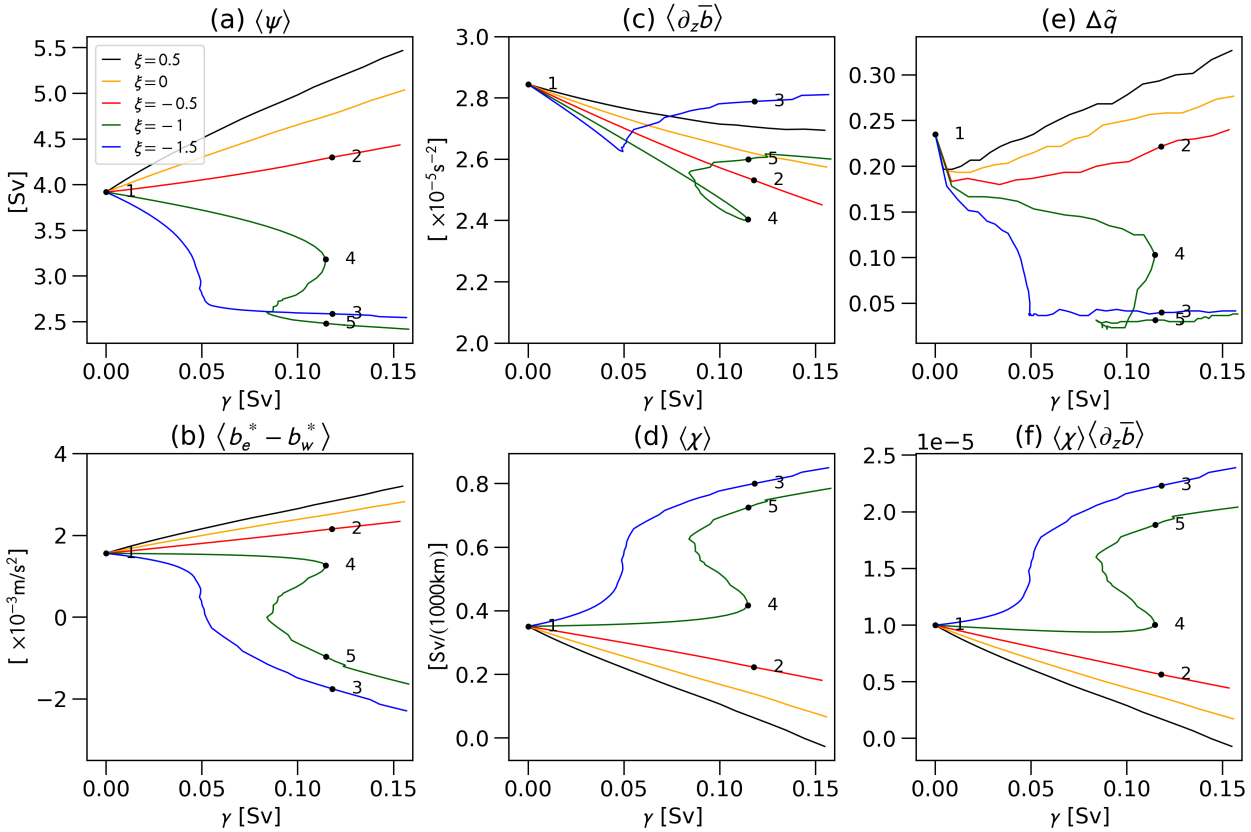

Figure 4.5: Bifurcation diagram of ZATOM under various freshwater forcing γ with asymmetry ξ. Here we show the curves of $\xi = -1, -0.5, 0, 0.5$ and 1. The dotted ocean states 1–5 are plotted in Figure 4.6.

diagrams of the mean strength of zonal overturning circulation $\langle\chi\rangle$, mean stratification $\langle\partial_z\bar{b}\rangle$, and east and west convective mixing fraction $\tilde{q}_e$ and $\tilde{q}_w$ in Figure 4.5c–e. These quantities are selected to interpret the behavior diagnosed by (4.24).

We first consider the case where the freshwater forcing is zonally symmetric, i.e., $\xi' = 0$, as this is the most common setup for many other studies on the multiple equilibria of overturning circulation. Figure 4.6a shows that the mean overturning circulation strength $\langle\psi\rangle$ increases as the freshwater forcing γ increases throughout the γ-axis. In Figure 4.5c-d, as γ increases, both the changes of the mean zonal overturning circulation $\delta\langle\chi\rangle$ and stratification $\delta\langle\partial_z\bar{b}\rangle$ are negative. The weakening of $\langle\chi\rangle$ is because the freshwater forcing increases (decreases) the buoyancy in the high-(low-)latitude ocean and thus weakens the

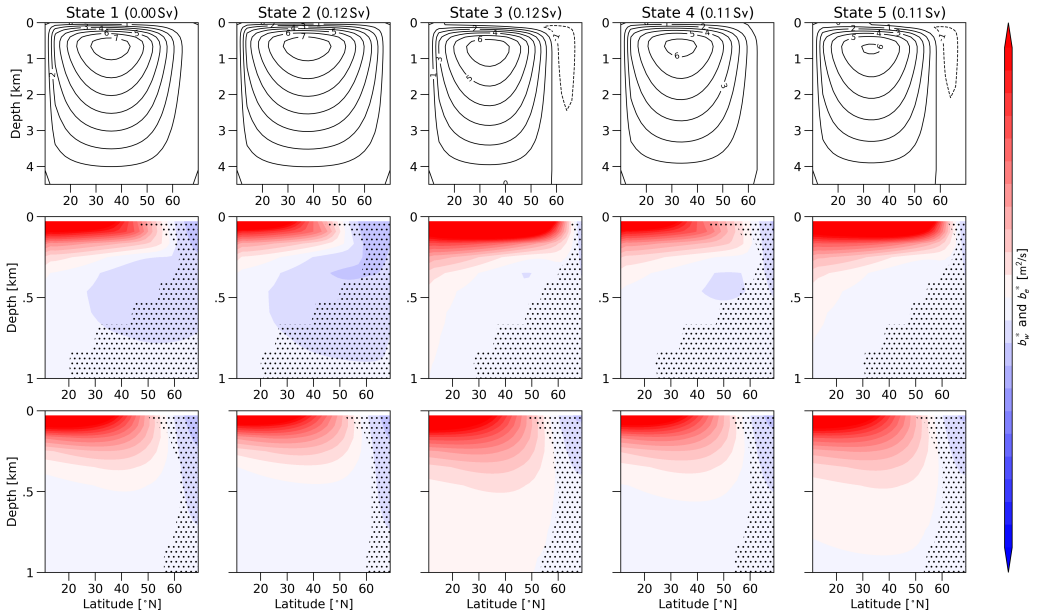

Figure 4.6: The analysis of states 1 to 5 as marked in Figure 4.5. Each column represents a state denoted in the title with the freshwater forcing γ in parenthesis. Top panels: the ψ in Sv. Middle panels: the shading shows b_w^*, the contours show the ψ in Sv, the dotted hatches show the regions where $\partial_z b_w < 0$. Bottom panels: the shading shows b_e, the contours show the χ in m^2/s, the dotted hatches show the regions where $\partial_z b_e < 0$. Notice that we only show the top 1 km of the ocean profile in the middle and lower panels.

north-south buoyancy gradient. The weakening of $\langle \partial_z \bar{b} \rangle$ is less obvious because the freshwater forcing stratifies the high latitude but destratifies low latitude. Because $\delta \langle \chi \rangle$ and $\delta \langle \partial_z \bar{b} \rangle$ contribute to the weakening of $\langle \psi \rangle$ as suggested by Equation (4.25), the increase of the $\langle \psi \rangle$ is associated with the increase of east-west difference of volume fraction of convective mixing $\Delta \tilde{q}$. In Figure 4.5e, except for the regime of very small γ, the $\Delta \tilde{q}$ curve of $\xi' = 0$ increases with increasing γ, meaning the convective mixing becomes relatively more vigorous in the western boundary as the freshwater forcing increases. While both the western boundary and eastern ocean stratify, the freshwater forcing is less effective in reducing the convective mixing in the western boundary because the more vigorous convective mixing in the western boundary removes the surface buoyancy faster than the eastern ocean. The increased east-west buoyancy difference intensifies the circulation and transports more salt into western boundary layer in high latitudes to trigger stronger convective mixing. It is shown in states 1 and 2 in Figure 4.6 where the less buoyant water extends downward in state 2 compared to state 1.

Now we examine the case where there is more freshwater delivered to the eastern ocean, i.e. the zonal asymmetry of freshwater forcing $\xi' > 0$. The case $\xi' = 0.5$ shows a steeper increase of the mean overturning circulation strength $\langle \psi \rangle$ along as the freshwater forcing γ increases compared to the case $\xi' = 0$ due to two contributions. One is the faster increase of mean stratification $\langle \partial_z \bar{b} \rangle$ that makes the zonal overturning circulation more efficient in generate east-west buoyancy difference as γ increases. The change in $\langle \partial_z \bar{b} \rangle$ is positive because that more freshwater is now delivered to the eastern ocean where there is less convective mixing such that the eastern ocean effectively traps the buoyant water at the surface and increase the stratification. The other one is the contribution from the zonal asymmetry $\xi' > 0$ that directly generates the east-west buoyancy difference. These two contributions overweigh the negative contribution from the greater decreasing rate of the mean zonal overturning circulation $\langle \chi \rangle$ as γ increases. On the contrary, for the cases where more freshwater is delivered to the western boundary, i.e. $\xi' < 0$, the freshwater is less effective in stratifying

the ocean. At the same time, the asymmetric freshwater forcing produces negative east-west buoyancy that contributes to the negative change of $\langle\psi\rangle$. Together they generate a milder increase of $\langle\psi\rangle$ in $\xi' = -0.5$ compared to $\xi' = 0$ and in $\xi' = 0$ compared to $\xi' = 0.5$.

If the delivery of the freshwater to the western boundary is strong enough such as $\xi' = -1.0$, the mean overturning circulation strength $\langle\psi\rangle$ weakens as the freshwater forcing γ increases. In this case, all the four components, i.e., the changes in the mean of stratification $\delta\left\langle\partial_z\bar{b}\right\rangle$, zonal overturning circulation $\delta\langle\chi\rangle$, east-west difference of volume fraction of convective mixing $\delta(\Delta\tilde{q})$, and zonal asymmetric freshwater forcing $\xi'\delta\gamma$, contribute to the weakening as shown in the bifurcation diagrams (Figure 4.5c–e).

In the case $\xi' = -1$, the curve reaches the bifurcation point at $\gamma \approx 0.12\,\mathrm{Sv}$. We label two steady states 4 and 5. During the transition from state 4 to 5, by selection they have the same freshwater forcing γ so that $\mathrm{d}\gamma = 0$. The change of the product of zonal overturning circulation and mean stratification $\delta\left(\left\langle\partial_z\bar{b}\right\rangle\langle\chi\rangle\right)$ is positive while the change of east-west convective mixing difference $\delta(\Delta\tilde{q})$ is negative. Examining the convective mixing fraction of the western boundary layer $\tilde{q}_w$ and eastern ocean $\tilde{q}_e$ (not shown), there is a reduction of $\tilde{q}_w$ but an increase of $\tilde{q}_e$. Therefore, the intensification due to stratification and meridional gradient is outcompeted by the shift of the deepwater formation from west to the east. The increase of $\langle\chi\rangle$, or equivalently $\langle\partial_y b_e^*\rangle$, is because the weaker overturning circulation produces less meridional mixing so that meridional buoyancy gradient is less removed. Less obvious is that the weaker salt transport increases the $\partial_z\bar{b}$ in higher latitude that outcompetes the decrease of $\partial_z\bar{b}$ in the lower latitude and results in an overall increase in $\left\langle\partial_z\bar{b}\right\rangle$. Once the $\tilde{q}_w$ decreases because of less salt transport, the dense water becomes trapped at the surface of the western boundary. These trapped dense water either diffuses or is transported to the eastern ocean to trigger convective mixing.

For $\xi' = -1.5$, the reduction of the deepwater formation in the western boundary layer and the negative contribution directly from the zonal asymmetry $\xi'\mathrm{d}\gamma$ are both negative and

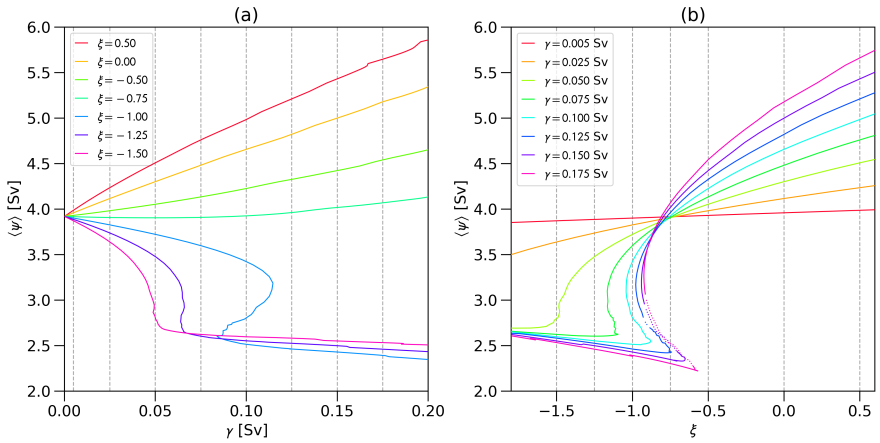

Figure 4.7: Bifurcation diagrams of ZATOM over the (a) γ-$\langle\psi\rangle$ and (b) ξ-$\langle\psi\rangle$ spaces. The vertical gray dashed lines in (a) mark the plotted fixed γ in (b). Conversely, the dashed lines in (b) mark the plotted fixed ξ in (a).

strong. The mean overturning circulation strength $\langle\psi\rangle$ quickly weakens and no bifurcation is found.

The analysis above clearly shows the dependency of multiple equilibria on the choice of ξ and it focuses on the solution branches with individual fixed zonal asymmetry of freshwater forcing ξ while varying freshwater forcing γ as shown in Figure 4.7a. To understand the multiple equilibria due to ξ more thoroughly, we can also obtain solution branches with fixed γ but varying ξ using the pseudo arc-length continuation technique.

The resulting solution branches in ψ-ξ space are shown in Figure 4.7b. An observation is that they seem to intersect a point at $(\xi, \langle\psi\rangle) \approx (-0.75, 3.9\text{Sv})$, meaning that if $\xi = -0.75$, the strength of overturning circulation will be independent of the freshwater forcing γ. Another observation is that there seem to exist an interval of ξ outside which there is no multiple equilibria, i.e. the interval $\xi \in [-1.5, -0.6]$. In the later Section 4.3.2, we will have a better physical understanding of these behavior through the extended two-box model.

4.3.2 The bifurcation diagrams of the extended two-box model

Following Cessi (1994), we consider the case that the temperature difference is quickly restored to the atmosphere forced temperature difference, i.e., $Q \to \infty$ such that $\delta T \to \delta T^*$, or equivalently $x \to 1$. Thus, the system (4.21) reduces to a single variable y as

$$\frac{\mathrm{d}y}{\mathrm{d}\tau} = p - (1 + |\Psi|)\, x \tag{4.27}$$

with

$$\Psi = \mu\,(1 - y) + \nu p \xi. \tag{4.28}$$

We plot the right-hand-side of tendency equation (4.27) as a function of y in Figure 4.8 where we have substitute the parameterization (4.28) into (4.27). The steady-states are the intercepts of the tendency curve with the horizontal axis $\mathrm{d}y/\mathrm{d}\tau = 0$. Given a freshwater forcing p, the solution has three special points: a fixed point A_1, a kink A_2, and a local minimum A_3 as

$$A_1 = (0, p)\,, \tag{4.29a}$$

$$A_2 = \left(1 + \frac{\nu p \xi}{\mu}, p - \left(1 + \frac{\nu p \xi}{\mu}\right)\right), \tag{4.29b}$$

$$A_3 = \left(\frac{1 + \mu + \nu p \xi}{2\mu}, p - \frac{(1 + \mu + \nu p \xi)^2}{4\mu}\right). \tag{4.29c}$$

If there are three steady-state solutions $\mathrm{d}y/\mathrm{d}\tau = 0$ such as the one shown in Figure 4.8. The middle solution is unstable. The outer two points are the stable solutions. Starting with the case $\xi = 0$ where the model reduces to the one devised in Cessi (1994), the left-most steady-state has $y < 1$, so this is a solution where the overturning circulation is dominated by meridional temperature gradient and is known as the thermal mode. Reversely, the right-most steady-state has $y > 1$, meaning the overturning circulation is reversed due to the

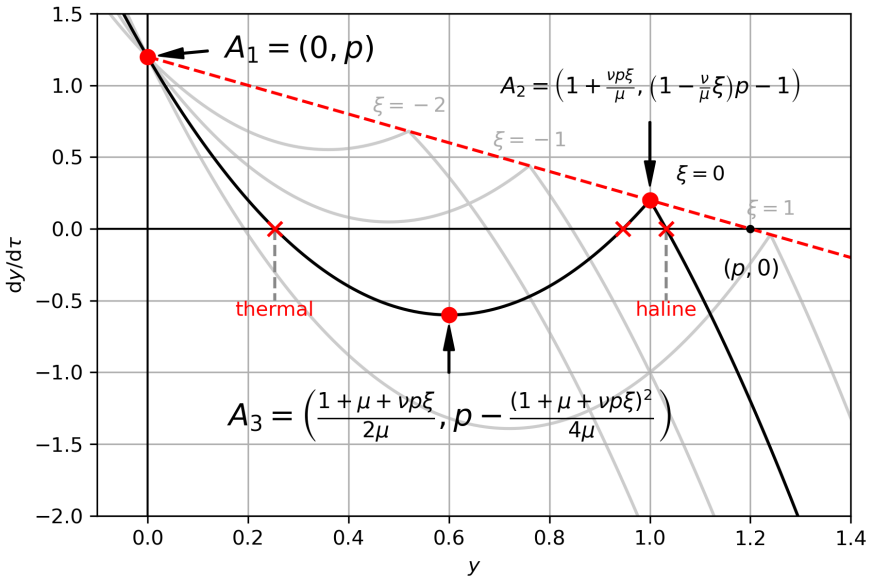

Figure 4.8: The analysis of the extended Stommel's two-box model. The horizontal and vertical axes show y and $\mathrm{d}y/\mathrm{d}\tau$. The curve shows the Equation (4.27). Three special points are dotted red. A_1 is a fixed point, A_2 is a kink point, also a local maxima in general, A_3 is a local minima horizontally between A_1 and A_2. Two steady-states are cross-denoted: thermal mode, characterized by low y value and therefore stronger Ψ; haline mode, high y and weaker Ψ. To demonstrate the change of the curve with ξ, we plot the curves with $\xi = -2, -1, 0$ and 1.

meridional salinity gradient and is known as the haline mode. We can extend this definition to accommodate the case where there only is one steady state: If the stable solution is to the left of A_3, then it is a thermal mode, otherwise it is a haline mode. This allows us to continue the discussion into the effect of changing ξ in the next paragraph.

In the Figure 4.8, the increase of zonal asymmetry ξ moves the kink point A_2 to the right along a straight line that intercepts at A_1 with a slope of -1, indicated by the red dashed line. The parametric form of this straight line of ξ is (4.29b). The location of A_2 controls the existence of thermal and haline modes. If ξ is large such that A_2 is below the horizontal line $\mathrm{d}y/\mathrm{d}\tau = 0$, or to the right of the point $(p, 0)$, then haline mode vanishes. The removal of haline mode physically means that the strengthening of overturning circulation ψ caused by asymmetric freshwater forcing overweighs the weakening of ψ due to the reduction in meridional buoyancy gradient caused by freshwater forcing. On the other hand, if ξ is low

such that A_3 is above the horizontal line $\mathrm{d}y/\mathrm{d}\tau = 0$, then the thermal mode vanishes. The removal of thermal mode physically means that the ψ generated by prescribed meridional temperature difference δT^* is not strong enough to remove the salinity difference generated by freshwater forcing γ so that y cannot be kept below 1.

To derive the analytical form of the p-Ψ bifurcation diagram, we solve for y as a function of p and Ψ in Equation (4.28) as

$$y = 1 - \frac{\Psi}{\mu} + \frac{\nu\xi}{\mu}p. \tag{4.30}$$

Then, use the expression above to substitute y in Equation (4.27), and solve for p to get the analytical solution along Ψ-axis given fixed ξ as

$$p = \frac{(1 + |\Psi|)\left(1 - \frac{\Psi}{\mu}\right)}{1 - \frac{\nu\xi}{\mu}(1 + |\Psi|)}. \tag{4.31}$$

Figures 4.9a shows the resulting bifurcation diagram in Ψ-p space. There are three special points: a fixed point B_1 and two bifurcation points B_2 and B_3 with their analytical solution as

$$B_1 = (0, \mu) \tag{4.32a}$$

$$B_2 = (p(\Psi^*), \Psi^*) \tag{4.32b}$$

$$B_3 = \left(\left(1 - \frac{\nu\xi}{\mu}\right)^{-1}, 0\right) \tag{4.32c}$$

where Ψ^* is solved by requiring $\mathrm{d}p/\mathrm{d}\Psi^* = 0$. The existence of B_1 is natural because when $p = 0$, zonal asymmetry of freshwater forcing loses its effect and therefore all choices of ξ should degenerate into the same solution. The interval of p between B_2 and B_3 is the regime with multiple equilibria.

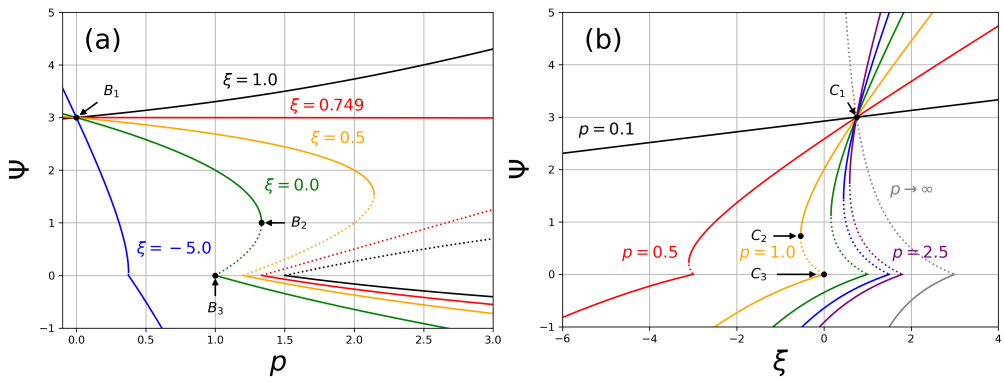

Figure 4.9: Bifurcation diagrams of the extended two-box model over the (a) p-Ψ and (b) ξ-Ψ spaces.

For certain choices of ξ, the solution B_2 is not well-defined. For example, the horizontal location of B_3 converges to $\pm\infty$ as $\xi \to \mu/\nu$ (the sign depends on the choice of μ and ν and the direction the limit is approaching). In this same case, B_3 should also approach to infinity. To resolve this issue, we can rearrange the Equation (4.31) to get the expression for ξ along Ψ-axis given fixed p as

$$\xi = \frac{\mu}{\nu}\left(\frac{1}{1+|\Psi|} - \frac{1-\frac{\Psi}{\mu}}{p}\right). \tag{4.33}$$

Figures 4.9b shows the resulting bifurcation diagram in Ψ-ξ spaces. There are three special points: a fixed point C_1, and two bifurcation points C_2 and C_3 with their analytical solution as

$$C_1 = \left(\frac{\mu}{(1+\mu)\,\nu}, \mu\right) \tag{4.34a}$$

$$C_2 = \left(\xi\left(\Psi^{**}\right), \Psi^{**}\right) \tag{4.34b}$$

$$C_3 = \left(\frac{\mu}{\nu}\left(1-\frac{1}{p}\right), 0\right) \tag{4.34c}$$

where $\Psi^{**} = \sqrt{p\mu} - 1 \geq 0$ is solved by requiring $\mathrm{d}\xi/\mathrm{d}\Psi^{**} = 0$. The existence of C_1 is special. Taking this particular choice ξ^*, the weakening of the overturning circulation Ψ due

to increased freshwater forcing p is completely cancelled by the strengthening of Ψ due to the supplying of east-west buoyancy gradient from ξ^*. Indeed, if we require $\partial\Psi\left(p,\xi^*\right)/\partial p = 0$ and apply it to Equation (4.28), we get

$$0 = -\mu\frac{\partial y^*}{\partial p} + \nu\xi^* \tag{4.35}$$

Then, we use the equilibrium solution of (4.27),

$$y^* = \frac{1}{1+\left|\Psi^*\right|} \tag{4.36}$$

where the asterisks denote the evaluated value at ξ^* to derive

$$\frac{\partial y^*}{\partial p} = \frac{1+\left|\Psi^*\right| - p\frac{\partial\Psi^*}{\partial p}/\left|\Psi^*\right|}{\left(1+\left|\Psi^*\right|\right)^2} = \frac{1}{1+\left|\Psi^*\right|} \tag{4.37}$$

Use the expression above to solve for ξ in Equation (4.35), we have

$$\xi^* = \frac{\mu}{\nu\left(1+\left|\Psi^*\right|\right)} = \frac{\mu}{\nu\left(1+\mu\right)} \tag{4.38}$$

where we have used the fact that $\Psi\left(p\right) = \Psi\left(p,\xi^*\right)$ should be a constant function that passes the fixed point B_1 on which $\Psi = \mu$.

When solving for the bifurcation point C_2, $\Psi^{**} = \sqrt{p\mu} - 1$ is strictly non-negative, meaning C_2 only exists for $p \geq 1/\mu$. The transformation from Equation (4.3.2) to (4.33) resolves the issue of diverging B_2 and B_3: the ξ position of C_2 always exists. Furthermore, it can be proved that if $\sqrt{p\mu} - 1 \geq 0$, then the ξ position of C_2 is always below C_3, meaning the ξ regime with multiple equilibria always exists as p going infinity.

4.3.3 The comparison between the regime diagrams with multiple equilibria of ZATOM and the extended two-box model

In this section, we will demonstrate that the zonal asymmetry of freshwater forcing ξ has a similar control on the regimes of multiple equilibria in both ZATOM and the extended two-box model.

We first discuss the qualitative behavior of regime with multiple equilibria of the extended two-box model since it has analytical solutions. Figure 4.10 shows the regime diagrams of the extended two-box models in the p-ξ space. We color the regime as the collection of p and ξ intervals enclosed by bifurcation points B_2, B_3 and C_2, C_3, respectively. In other words, the left and right boundaries of blue dotted-hatched area are the collections of B_3 and B_2; the lower and upper boundaries of red line-hatched area are the collections of C_2 and C_3. This method is adequate to find regime through the ξ intervals enclosed by C_2 and C_2 while failed through finding intervals enclosed by B_2 and B_3. The numerical solver failed to find B_2 and B_3 above $\xi = \mu/\nu\,(1+\mu)$ because these two points diverge to infinity.

In Figure 4.10, the regime of multiple equilibria in the extended two-box model is bounded from below as $p = 1/\mu$ but extends to $p \to \infty$. This regime is also bounded from below as $\xi = -\mu\,(\mu-1)\,/\nu$ and from above as $\xi = \mu/\nu$. For p, the lower bound is $p = 1/\mu$. We denote this left-bottom corner point as $P = (1/\mu, -\mu\,(\mu-1)\,/\nu)$.

Figure 4.11a shows the regimes with multiple equilibria of the extended two-box model and ZATOM. To dimensionalize the extended two-box model compare it with the result of ZATOM. We use the values given in ZATOM to setup the values. Thus, we let the prescribed meridional temperature gradient $\delta T^* = 25\,\mathrm{K}$, halved ocean volume $V = 2.46 \times 10^1 6\,\mathrm{m}^3$ ($2V$ is the entire ocean volume in ZATOM), the surface area of the eastern ocean is three times to that of the western boundary layer, i.e., $A_e = 3A_e$ such that the $G = 1/3$. We estimate the diffusion timescale $t_d = L^2/K_H \approx 35\,\mathrm{yr}$ where we let $L = 6.70 \times 10^6\mathrm{m}$ as the

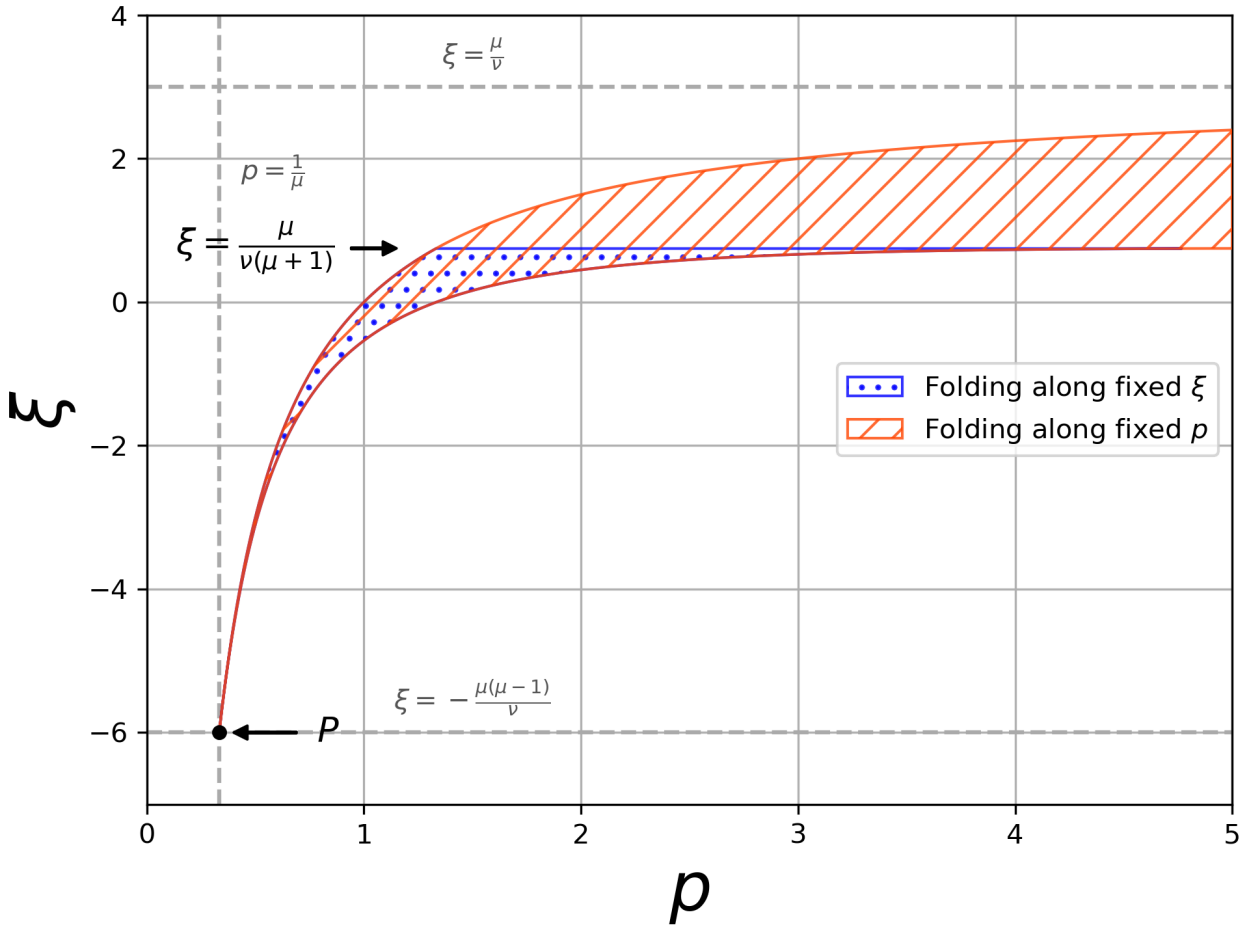

Figure 4.10: The regime diagrams with multiple equilibria of (a) ZATOM and (b) the extended two-box model over the γ-ξ and p-ξ spaces. γ and p are the strengths of freshwater forcing in ZATOM and the extended two-box model, respectively. The shaded regions denote the parameter space that has multiple equilibria. The blue-dotted-hatched area is the regime with multiple equilibria over γ or p enclosed by points B_2 and B_3. The red-line-hatched area is the regime with multiple equilibria over ξ enclosed by points C_2 and C_3.

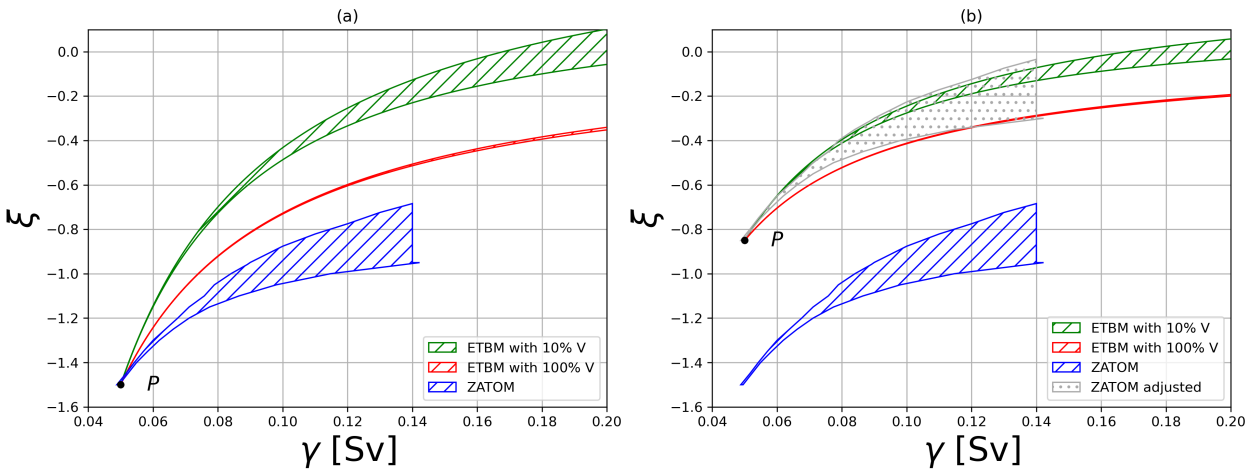

Figure 4.11: The regimes with multiple equilibria of ZATOM and the extended two-box model over the γ-ξ spaces. The hatched regions denote the parameter space that has multiple equilibria. In (a), the values of μ and ν in the extended two-box model is estimated with $P = (0.05\,\mathrm{Sv}, -1.5)$ while in (b) we let solve with $P = (0.05\,\mathrm{Sv}, -0.85)$ to manually correct the positive ξ bias in ZATOM.

meridional length of the domain and $K_H = 4 \times 10^4\,\mathrm{m}^2/\mathrm{s}$. To determine μ and ν, we use the fact that the regime of ZATOM has a similar tip in the left-bottom corner to that of extended two-box model, i.e., point P, in Figure 4.11a. Since P has an analytical solution $P = (1/p, -\mu\,(\mu - 1)\,/\nu)$, we equate this location with the point of the tip in ZATOM $P = (0.05\mathrm{Sv}, -1.5)$ to solve for μ and ν. We need to point out that in the extended two-box model, the C_1 point always locates at $\xi = \mu/\left((1+\mu)\,\nu\right) \geq 0$ while the C_1 point of ZATOM locates at $\xi = -0.75 < 0$. Our explanation is that the surface eastward flow due to the zonal overturning circulation in ZATOM pushes the surface freshwater forcing to the east, effectively creates a positive ξ bias, creating the entire shift of the bifurcation diagram towards negative ξ. This argument seems to be valid because if we set the ξ of point P as -0.85 instead of -1.5 to manually correct the bias in ξ, the regimes of the two-box model and ZATOM overlap (Figure 4.11b).

A sensitivity of the extended two-box model is the choice of V that affects the strength of the overturning circulation. The strength of the circulation at point C_1 (Figure 4.9) is an convenient measure because it is a fixed point across different freshwater forcing. According

to our setup, the strength of the overturning circulation at C_1 is given by

$$\psi = \frac{\mu V}{t_d} = \gamma^* \frac{\alpha_T \delta T^* V^2}{2\,(1+G)\,\alpha_S S_0 t_d^2} \tag{4.39}$$

where γ^* is the value of γ at C_1. Using the $V = 2.46\times10^{16}\,\mathrm{m}^3$, $\psi = 737\,\mathrm{Sv}$ which is unrealistic. To obtain a better agreement with ZATOM, we observe that in Figure 4.6 the emergence of the reversed circulation is limited to the surface and higher latitude. Making the effective V smaller. Therefore, we additionally plot the regime with multiple equilibria of the extended two-box model with 10% of the V in Figure 4.11. The choice of 10% volume reduces the original estimated overturning circulation strength by 99%, leaving $\psi = 7.37\,\mathrm{Sv}$, which is the same order of magnitude we have in ZATOM. The correction of effect V is convincing because the regime of the extended two-box model with 10% volume is also overlapping with the regime of ZATOM.

As the freshwater forcing γ increases, both the regimes with multiple equilibria of ZATOM and the extended two-box model shifts towards positive direction of zonal asymmetry of freshwater forcing ξ, meaning given the same ξ, stronger γ will induce the haline mode. Similarly, as the ξ increases, the regimes shift towards positive γ direction, meaning given the same γ, larger ξ will favor the thermal mode.

Given the same zonal asymmetry of freshwater forcing ξ, the regime of the extended two-box model is generally thinner than that of ZATOM. Among two choices of ocean volume scale V, we see that the regime with smaller V has a wider regime while larger V has a narrower regime. However, the regime of ZATOM is the widest and flattest among all, we think that the difference between the model is not merely because the choice of V but also the differences of the processes that is involved in generating multiple equilibria. We speculate that it is the existence of the interactive convective mixing that enlarges the width of the regime in ZATOM. In particular, we argue that the interactive convective mixing strengthens

the salt-advection feedback which in turns widen the regime of multiple equilibria: If there is not enough loss of buoyancy, the convective mixing will not be extending downward because the surface ocean is stratified; once there is enough loss of buoyancy such that the depth of convective mixing extends below the thermocline, the growth of the depth of convective mixing per unit increase of buoyancy loss will increase dramatically. This effectively makes a stronger positive salt-advection feedback that widens the regime of multiple equilibria.

An important information reveled by the regime diagrams in Figure 4.11 is that for sufficiently large positive or negative fixed values of zonal asymmetry of freshwater forcing ξ, the bifurcation does not exist. Moreover, while larger values of ξ has larger separation of multiple equilibria in the strength of overturning circulation (Figures 4.7 and 4.9), larger values of ξ shifts the regime of multiple equilibria to higher freshwater forcing γ. These observations might provide explanation for the absence of the multiple equilibria in more realistic models Weijer, Cheng, Drijfhout, et al., 2019.

4.3.4 Comparison with Dijkstra and Weijer (2003)

The dependence of multiple equilibria on the zonal asymmetry of freshwater forcing has not received much attention, but Dijkstra and Weijer (2003) is an exception. Dijkstra and Weijer (2003) used the continuation method to trace out the bifurcation diagram of the overturning circulation in an OGCM that coupled to an energy balance atmospheric model with realistic continental arrangement. Their model did not have convective adjustment for it required high computational costs due to associated grid-scale bifurcations (den Toom et al., 2011). They imposed the freshwater forcing as a linear combination of hydrological forcing and a local rectangular freshwater flux over the Labrador Sea where the deepwater formation occurs ([60°–24°W] × [54°–66°N]). The hydrological forcing over the Atlantic Ocean is relatively zonally symmetric compared to their local freshwater forcing over the Labrador Sea, which

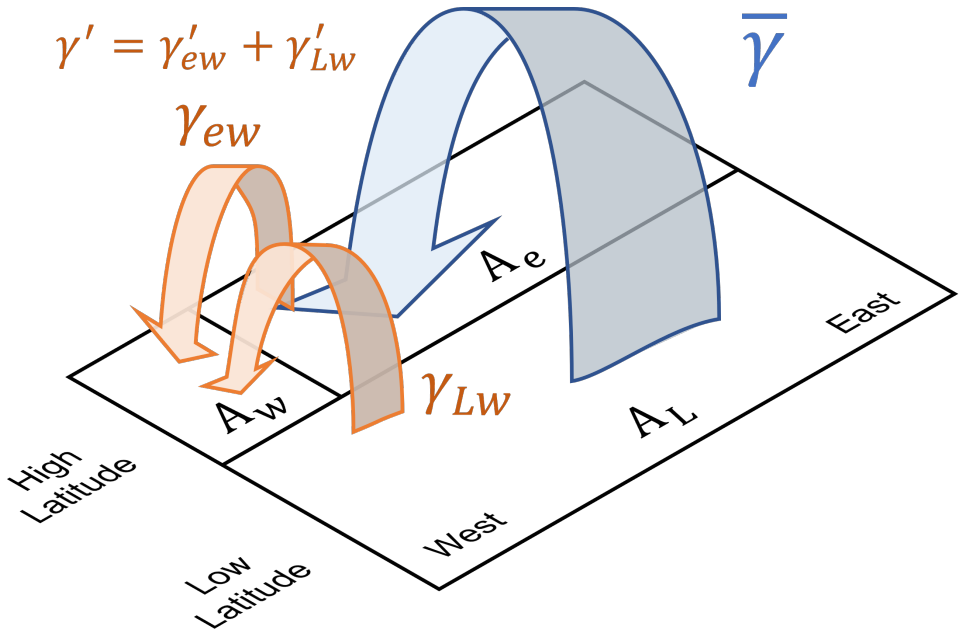

Figure 4.12: The simplified analogy of the freshwater forcing used in Dijkstra and Weijer (2003). There are three boxes representing the Atlantic ocean: low latitude box, high latitude western box, and high latitude eastern box with surface areas A_L, A_w, and A_e. The $\overline{\gamma}$ is the hydrological forcing (blue arrow) transporting the freshwater from low to high latitude ocean. The $\gamma' = \gamma'_{Lw} + \gamma'_{ew}$ is the local freshwater forcing over the western box transporting moisture from low latitude (γ'_{Lw}) and eastern boxes (γ'_{ew}). The transports are proportional to individual surface areas to ensure the freshwater flux per unit area is even, i.e. $\gamma'_{Lw}/A_L = \gamma'_{ew}/A_e$.

essentially locates on the western boundary of Atlantic Ocean. Thus, we can view their hydrological forcing as the zonally symmetric freshwater forcing and the local freshwater forcing as a zonally asymmetric freshwater forcing.

In Dijkstra and Weijer (2003), they constructed bifurcation diagrams using several chosen strengths of local freshwater flux, in their Figure 1a they showed an emergence of multiple equilibria. If a lower local freshwater flux is chosen, increasing the hydrological forcing results in an intensification of overturning circulation. Oppositely, if higher local freshwater flux is chosen, increasing the hydrological forcing weakens the overturning circulation. The behavior described above is very similar to what we see in our Figures 4.7a and 4.9a. Therefore, we speculate the zonal asymmetry of freshwater forcing plays a role in their experiments.

It will be informative if we can map the coordinate in their Figure 1a to our Figure 4.11. To achieve this, we simplify their domain into three boxes as shown in Figure 4.12 with the high-latitude eastern, western, and low-latitude boxes having a surface area of A_w, A_e, and A_L. We denote the hydrological forcing as $\overline{\gamma}$ (their γ) and the local freshwater forcing as γ' (their γ_p). The positive γ' represents the freshwater forcing over the western box and is balanced by an averaged evaporation everywhere else. Therefore, this arrangement is equivalent to ZATOM with

$$\gamma = \overline{\gamma} + \frac{A_L}{A_e + A_L}\gamma' \tag{4.40}$$

The second term on the right-hand-side comes from the evaporation associated with the local freshwater flux. The zonally symmetric high-latitude precipitation is

$$\overline{p} = \frac{\gamma}{A_H} \tag{4.41}$$

where $A_H := A_w + A_e$ is the total high-latitude surface area. The precipitation rate over the western box is

$$p_w = \frac{\overline{\gamma}}{A_H} + \frac{\gamma'}{A_w} \tag{4.42}$$

Therefore, the deviation of the precipitation over the western box is

$$\Delta p_w = p_w - \overline{p} = \frac{\overline{\gamma} - \gamma}{A_H} + \frac{\gamma'}{A_w} \tag{4.43}$$

The asymmetry of freshwater forcing ξ becomes

$$\xi = -\frac{\Delta p_w}{\overline{p}} = -\frac{1 + \frac{A_H(A_L + A_e)}{A_W A_L}}{1 + \frac{A_L + A_e}{A_L}\frac{\overline{\gamma}}{\gamma'}} \tag{4.44}$$

Hence we have the transformation

$$(\gamma, \xi) = \left(\overline{\gamma} + \frac{A_L}{A_e + A_L}\gamma', -\frac{1 + \frac{A_H(A_L+A_e)}{A_w A_L}}{1 + \frac{A_L+A_e}{A_L}\frac{\overline{\gamma}}{\gamma'}} \right) \tag{4.45}$$

to convert from their coordinate to ours. Keeping $\overline{\gamma}$ fixed, decreasing γ' is equivalent to moving towards negative direction in the γ but positive direction in ξ, meaning the overturning circulation favors the thermal mode if local freshwater is weak. Conversely, increasing γ' is equivalent to moving towards positive direction in the γ but negative direction in ξ, meaning the overturning circulation moves towards the haline mode. Readers are noted that the usage of thermal and haline modes here becomes ambiguous if this parametric trajectory does not cross the regime with bifurcation because in such cases there does not exist multiple equilibria along the trajectory. Similarly, keeping γ' fixed, increasing $\overline{\xi}$ is equivalent to moving towards positive direction of γ and ξ and vice versa. Interestingly, ξ never gets above $\xi = 0$ if $\overline{\gamma}$ and γ' are of the same sign, meaning whether the regime with equilibria extends to $\xi = 0$ is important. It makes the regime diagrams in Figure 4.11a and b significantly different this way because the regime of multiple equilibria in ZATOM does not seem to cross $\xi = 0$ while the two-box model does.

Our study gives different perspective of the emergence of multiple equilibria of the overturning circulation from Dijkstra and Weijer (2003). First, Dijkstra and Weijer (2003) explained that the emergence of multiple equilibria is due to emergence of northern sinking mode competing with the southern sinking mode, which is a contrast to our model setup because these sinking modes are associated with double hemispheric symmetry breaking while in this paper we use the single hemisphere domain that should not have such geometric symmetry. Second, in ZATOM the convective adjustment is crucial in understanding the bifurcation in our analysis in Section 4.3.1 while the OGCM of Dijkstra and Weijer (2003) does not implement the convective adjustment. Future investigation will be needed to explain these gaps between ZATOM and their OGCM.

4.4 Conclusion

In this paper, we study the dynamics and multiple equilibria of ZATOM and the extended two-box model in a single hemisphere with zonally asymmetric of freshwater forcing ξ. By constructing their regime diagrams (Figures 4.11), it is found that both model share similar dependency of the regime with multiple equilibria over the freshwater forcing versus zonal asymmetry of freshwater γ-ξ space. Through the extended two-box model, we are able to understand that ξ controls the existence of thermal and haline modes. Large positive values of ξ enhance the thermal mode whereas large negative values of ξ enhances the haline mode. We also derive a multi-linear relation Equation (4.24) consistting of the strength of overturning circulation with respect to the product of mean stratification and mean meridional gradient, the east-west difference of convective mixing, and the asymmetric freshwater forcing. By using this diagnostic relation, we argue that the convective mixing plays an important role in the transition between on- and off-states of the overturning circulation.

The impact of the asymmetry of freshwater forcing over the strength of overturning circulation and the regime of multiple equilibria of overturning circulation are potentially influential. In the Supplementary Information of Weijer, Cheng, Garuba, et al. (2020), they showed that the strength of AMOC measured at 26°N ranges from 8 to 32 Sv among 27 different climate models. The large intermodel spread among the climate models clearly remains an unresolved important issue because the thermohaline circulation strongly modulates the transient climate response to global warming (Kostov et al., 2014; D. P. Marshall and Zanna, 2014; Rose and Rayborn, 2016; Lewis and Curry, 2018; Shi et al., 2018).

Our finding encourages future idealized studies to explore the effect of zonal redistribution of freshwater discharge due to surface processes, including wind-driven circulations such as gyres and Ekman transport. Finally, the domain used in ZATOM should be extended across the equator and having a re-entrant channel representing the Southern Ocean. Such

extensions are important as the southern meridional overturning circulation has influential impact on the AMOC (Nikurashin and G. Vallis, 2012) and is found to be responsible for more than half of the ocean heat uptake under global warming (Shi et al., 2018).

Appendix

4.A ZATOM detail

The governing equations of tracers in ZATOM is separated into western boundary layer and eastern boundary layer which will be denoted using subscripts w and e. The governing equations are

$$\begin{aligned}\frac{\partial}{\partial t}X_w =& -\frac{u_i}{L_b}X_e - \mathrm{D}_y\left(v_w X_w\right) - \mathrm{D}_z\left(w_w X_w\right) \\ &+ \mathrm{D}_y\left(K_H \partial_y X_w\right) + \mathrm{D}_z\left(K_V \partial_z X_w\right) + q_{X,w} + F_{X,w} + \frac{K_{\mathrm{b.c.}}}{L_b}\frac{X_e^* - X_w^*}{L_b},\end{aligned} \tag{4.46}$$

$$\begin{aligned}\frac{\partial}{\partial t}X_e =& \frac{u_i}{L_b + L_i}X_e - G\mathrm{D}_z\left(w_e X_e\right) \\ &+ \mathrm{D}_y\left(K_H \partial_y X_e\right) + \mathrm{D}_z\left(K_V \partial_z X_e\right) + q_{X,e} + F_{X,e} - \frac{K_{\mathrm{b.c.}}}{L_b + L_i}\frac{X_e^* - X_w^*}{L_b},\end{aligned} \tag{4.47}$$

where X can be temperature T or salinity S, subscript w and e denote the mean tracer values in the western boundary and eastern ocean, X_w^* and X_e^* are the values of tracer X on the western and eastern boundaries. According to the design shown in Figure 4.2, $X_w = \left(X_w^* + X_e^*\right)/2$, and $X_e = X_e^*$. The L_b and L_i are the widths of boundary layer and interior ocean, u_i the zonal velocity of the interior ocean, D_y and D_z are the one dimensional divergence operators in the meridional and vertical direction, ∂_y and ∂_z are the gradient

operators in the meridional and vertical direction, $v_{(\cdot)}$ and $w_{(\cdot)}$ are the meridional and vertical velocities in the boundary layers and v_e is set to zero. The K_H is the constant meridional diffusivity, K_V is the vertical background diffusivity, $q_{X,(\cdot)}$ is the convective mixing that depends on the local stratification (see Equation (4.48)), $K_{\text{b.c.}}$ is the strong zonal diffusivity between the western and eastern boundary layers that is only non-zero on the northern and southern boundary to achieve boundary condition (see Equation (4.58a)), $F_{X,(\cdot)}$ is the forcing of $X_{(\cdot)}$ (see Equations (4.10) and (4.11a)), $G = \Delta\lambda_b / (\Delta\lambda_b + \Delta\lambda_i)$ is the geometric factor that acts on the eastern boundary because we assume well-mixed condition between eastern boundary layer and interior ocean.

The explicit form of convective adjustment is

$$q_{X,(\cdot)} = \mathrm{D}_z \left(K_c \Gamma \left(\frac{s_{(\cdot)}}{\Delta_c} \right) \partial_z X \right), \tag{4.48}$$

where K_c is the diffusivity constant of convective mixing. The Γ

$$\Gamma(x) = \begin{cases} 1 & \text{if } x < -1, \\ 3x^2 + 2x^3 & \text{if } -1 \leq x < 0 \\ 0 & \text{if } x \geq 0 \end{cases} \tag{4.49}$$

is a transition function that activates K_c with transition width Δ_c when the stratification $s_{(\cdot)} = \partial_z b_{(\cdot)} < 0$. The transition function Γ has a continuous first derivative that allows Newton's method to converge. Our model adopts the spherical coordinate (λ-ϕ-z) and the corresponding operators are

$$(\mathrm{D}_y, \mathrm{D}_z) = \left(\frac{\partial \cos\phi}{a \cos\phi \partial\phi}, \frac{\partial}{\partial z} \right), \tag{4.50}$$

$$(\partial_y, \partial_z) = \left(\frac{\partial}{a\partial\phi}, \frac{\partial}{\partial z} \right), \tag{4.51}$$

$$(L_b, L_i) = a \cos\phi \, (\Delta\lambda_b, \Delta\lambda_i), \tag{4.52}$$

where a is the radius of Earth.

The thermal wind relationships are

$$\partial_z u_i = -\frac{1}{f}\partial_y b_e^*, \tag{4.53a}$$

$$\partial_z v_w = \frac{1}{f}\frac{b_e^* - b_w^*}{L_b}, \tag{4.53b}$$

where f is the Coriolis parameter. The continuity equations are

$$-\frac{u_i}{L_b} + \mathrm{D}_z w_e = 0, \tag{4.54a}$$

$$\frac{u_i}{L_b} + \mathrm{D}_y v_w + \mathrm{D}_z w_w = 0. \tag{4.54b}$$

To diagnose the velocities, we first apply ∂_z to Equations (4.54a) and (4.54b) to obtain

$$\partial_z^2 w_e = -\frac{\partial_y b_e^*}{f L_b} \tag{4.55a}$$

$$\partial_z^2 w_w = \frac{\partial_y b_e^*}{f L_b} - \mathrm{D}_y\left(\frac{1}{f}\frac{b_e^* - b_w^*}{L_b}\right) \tag{4.55b}$$

The summation of two equations above gives

$$\partial_y \partial_z^2 \psi = -\partial_y\left(\frac{b_e^* - b_w^*}{f}\right) \tag{4.56}$$

where ψ is the stream function such that

$$L_b\left(v_w, w_w + w_e\right) = \left(-\partial_z\psi, \partial_y\psi\right). \tag{4.57}$$

Then, through thermal wind balance (4.53b) and the streamfunction (4.57), the no-normal

flow boundary conditions also requires

$$b_e^* = b_w^*, \tag{4.58a}$$

$$\frac{\partial^2 \psi}{\partial z^2} = 0 \tag{4.58b}$$

at $\phi = \phi_s, \phi_n$ where ϕ_s and ϕ_n are the latitudes of southern and northern boundaries. Integrate the equation (4.56) with respect to y gives the diagnostic equation

$$\partial_z^2 \psi = -\left(\frac{b_e^* - b_w^*}{f}\right). \tag{4.59}$$

The north and south boundary condition $b_e^* = b_w^*$ is achieved through specifying large values of $K_{\text{b.c.}}$ at the north and south grid points. The equations (4.59), (4.57), (4.55a), (4.54a) are the necessary equations to solve for v_w, w_w, w_e, u_i with no-normal boundary conditions.

The equation (4.54a) directly implies the zonal overturning circulation density $\chi = \chi(\phi, z)$ whose velocities are

$$(u_i, w_e) = \left(-\partial_z \chi, -\frac{\chi}{L_b}\right). \tag{4.60}$$

As a result, the ocean circulation is a superposition of meridional and zonal overturning circulations. Notice that the strength of meridional overturning circulation ψ is measured as the total volume flux so it has the unit of m^3/s. The strength of zonal overturing circulation χ is as volume flux per unit width in meridional direction so it has the unit of m^2/s.

Three useful scaling relationships come out from the elliptical equations (4.55a) and (4.59)

$$w_e \approx \frac{H^2}{fL_b}\partial_y b_e^*, \tag{4.61a}$$

$$\psi \approx \frac{H^2}{f}\left(b_e^* - b_w^*\right), \tag{4.61b}$$

$$\chi \approx -\frac{H^2}{f}\partial_y b_e^*. \tag{4.61c}$$

The numerical model uses Arakawa-C grid (Figure S1). To physically step the model, we adopts Runge-Kutta of the second order to advect the tracers and we step the forcing, convective mixing and diffusion using Euler backward method.

4.B Diagnostic

To find a simple diagnostic equation for ψ, we start transforming (4.46) into buoyancy form ($b = \alpha_T T - \alpha_S S$) as

$$\frac{\partial}{\partial t}b_w = -\frac{u_i}{L_b}\left(b_e - b_w\right) - v_w\partial_y b_w - v_w\partial_z b_w + \mathrm{D}_y\left(K_H\partial_y b_w\right) + \mathrm{D}_z\left(K_V\partial_z b_w\right) + q_{b,w} \tag{4.62a}$$

$$+ \alpha_T F_{T,w} - \alpha_S F_{S,w} + \frac{K_{\mathrm{b.c.}}}{L_b}\frac{b_e^* - b_w^*}{L_b},$$

$$\frac{\partial}{\partial t}b_e = -Gw_e\partial_z b_e + \mathrm{D}_y\left(K_H\partial_y b_e\right) + \mathrm{D}_z\left(K_V\partial_z b_e\right) + q_{b,e} \tag{4.62b}$$

$$+ \alpha_T F_{T,e} - \alpha_S F_{S,e} - \frac{K_{\mathrm{b.c.}}}{L_b + L_i}\frac{b_e^* - b_w^*}{L_b},$$

where we have use the continuity equation to convert the equation into the advection form. Then, by doing (4.63) - (4.62a) and get

$$\frac{\partial b_e - b_w}{\partial t} = u_i \frac{b_e - b_w}{L_b} + v_w \partial_y b_w - \left(G w_e \partial_z b_e - w_w \partial_z b_w\right) + \mathrm{D}_y \left[K_H \partial_y \left(b_e - b_w\right)\right] + \mathrm{D}_z \left[K_{V,e} \partial_z \left(b_e - b_w\right)\right] + \left(q_{b,e} - q_{b,w}\right) + \alpha_T \left(F_{T,e} - F_{T,w}\right) - \alpha_S \left(F_{S,e} - F_{S,w}\right) - 2 \left(\frac{1}{L_b} + \frac{1}{L_b + L_i}\right) K_{\mathrm{b.c.}} \frac{b_e - b_w}{L_b}. \tag{4.63}$$

We then (1) assume the east-west gradient is much weaker than vertical gradient so that we can drop the terms having $b_e - b_w$, (2) assume $\partial_z b_w \approx \partial_z b_e \approx \partial_z \bar{b}$, (3) assume w_w is mostly contributed by ZOC so that $w_w \approx -w_e$. The resulting equation is

$$\frac{\partial b_e - b_w}{\partial t} = v_w \partial_y b_w + \left(1 + G\right) \frac{\chi}{L_b} \partial_z \bar{b} + \left(q_{b,e} - q_{b,w}\right) - \frac{\alpha_T}{\tau_T} \left(T_e - T_w\right) \Theta_{H_T} + \alpha_S \left(1 + G\right) S_0 \gamma \sigma \xi' \eta \frac{\Theta_{H_S}}{H_S}. \tag{4.64}$$

where we use Equation (4.60) to replace vertical velocity with χ, substitute the actual forcing with Equations (4.10) and (4.11a). Next, define the ocean average with the bracket as

$$\langle \cdot \rangle = \frac{1}{\left(\sin \phi_n - \sin \phi_s\right) H^*} \int_{-H^*}^{0} \int_{\phi_s}^{\phi_n} (\cdot) \cos \phi \mathrm{d}\phi \, \mathrm{d}z \tag{4.65}$$

we apply the average over (4.64) to get

$$\frac{\partial}{\partial t} \langle b_e - b_w \rangle = \langle v_w \partial_y b_w \rangle + \left(1 + G\right) \frac{\left\langle \chi \partial_z \bar{b} \right\rangle}{L_b} + \left(\langle q_{b,e} \rangle - \langle q_{b,w} \rangle\right) - \left\langle \frac{\alpha_T}{\tau_T} \left(T_e - T_w\right) \Theta_{H_T} \right\rangle + \alpha_S \frac{1 + G}{H^*} S_0 \gamma \xi'. \tag{4.66}$$

Physically, the meridional advection associated with MOC and the sea-surface temperature boundary condition act to remove the east-west buoyancy difference, which inspire us to

assume they remove the $b_e - b_w$ in a timescale of τ'. Therefore, in the steady-state,

$$\frac{\langle b_e^* - b_w^* \rangle}{2\tau'} = (1+G)\frac{\left\langle \chi \partial_z \bar{b} \right\rangle}{L_b} + \Delta \langle q_b \rangle + \alpha_S \frac{1+G}{H^*} S_0 \gamma \xi'. \tag{4.67}$$

where we have used the identity $b_e - b_w = (b_e^* - b_w^*)/2$ and define $\Delta \langle q_b \rangle := \langle q_{b,e} \rangle - \langle q_{b,w} \rangle$. Next, we define $\tilde{q}_\Omega$ as the fraction of the cell volumes in the top H^* of the ocean whose convective mixing is active in place of the convective mixing q and $\Delta\tilde{q} := \tilde{q}_e - \tilde{q}_w \propto \langle \Delta \langle q_b \rangle \rangle$. The definition using fraction is convenient because $\tilde{q}_\Omega$ does not depend on the type of tracer. Finally, for analysis purpose we assume $\left\langle \chi \partial_z \bar{b} \right\rangle \approx \langle \chi \rangle \left\langle \partial_z \bar{b} \right\rangle$, and define so that

$$\frac{\langle b_e^* - b_w^* \rangle}{2\tau'} = (1+G)\frac{\langle \chi \rangle \left\langle \partial_z \bar{b} \right\rangle}{L_b} + c_0 \Delta\tilde{q} + \alpha_S \frac{1+G}{H^*} S_0 \gamma \xi', \tag{4.68}$$

where c_0 is a constant. Clean up all constants, we have

$$\langle b_e^* - b_w^* \rangle = c_1 \langle \chi \rangle \left\langle \partial_z \bar{b} \right\rangle + c_2 \Delta\tilde{q} + c_3 \xi' \gamma. \tag{4.69}$$

A more inspiring equation that connects the meridional buoyancy gradient and ψ can be derived by using the approximation

$$\chi \approx -\frac{H^2}{f_0} \partial_y b_e^* \quad \text{from (4.61c)}, \tag{4.70a}$$

$$\psi \approx \frac{H^2}{f_0} (b_e^* - b_w^*) \quad \text{from (4.61b)}, \tag{4.70b}$$

where we assume $f = f_0$. Substitute these approximation into (4.69) we have

$$\langle \psi \rangle = -c_1' \langle \partial_y b_e^* \rangle \left\langle \partial_z \bar{b} \right\rangle + c_2' \Delta\tilde{q} + c_3 \xi' \gamma. \tag{4.71}$$

The Equation (4.71) explicitly relates the ψ with meridional buoyancy gradient, stratification, east-west convective mixing difference, and the zonal asymmetry of hydrologic forcing.

Chapter 5

Conclusion

As our climate is warming due to the rapid increase of greenhouse gases, the Earth's atmospheric and oceanic circulations, hydrology cycle, ecosystem, and human's society is going to change accordingly. Still, there remains a lot of uncertainties in how the climate system is responding to the greenhouse forcing. Some of the uncertainties originates from the air-sea coupling. In this thesis, we study how the ocean modulates the climate response towards global warming through air-sea coupling in chapter 2 and 3. These two chapters reveal that the Atlantic meridional overturning circulation (AMOC) has a dominant role to modulate the climate response. Therefore, in chapter 4 we subsequently study how the existence of AMOC multiple equilibria, a necessary condition for AMOC shutdown, is affected by the zonal asymmetry of freshwater forcing.

5.1 Summary of the work

To study the influence of ocean processes in a changing climate, we formulate the Ekman mixed-layer model (EMOM) to construct a hierarchy of ocean models in Chapter 2. The

EMOM explicitly resolves the wind-induced Ekman flow at the ocean surface and resolves the entrainment due to the variation of the ocean mixed layer. By independently turning on and off the Ekman flow and variation of mixed-layer thickness, EMOM can degenerate into the mixed-layer model and the slab ocean model. Together with the targeted ocean general circulation model (OGCM), chosen as POP2, an ocean hierarchy of four members is formed. The hierarchy can be used to study the non-linear effect due to the air-sea coupling. The hierarchy also reduces the inter-model uncertainties because three out of four models are physically consistent.

We also examine the unperturbed climatology simulated in EMOM-derived models. Given adequate flux corrections, all models are able to produce similar climatology, including sea-surface temperature, precipitation and sea ice coverage. The flux correction derivation is non trivial because it does not only contain the missing processes. We realize that the flux correction also includes the flux of missing mechanism but resolved processes. The mean sea-surface temperature (SST) bias in the slab ocean model is largely corrected when the variation of mixed-layer thickness is included. The inclusion of wind-induced Ekman flow improves the simulated Pacific Decadal Oscillation pattern and its temporal spectrum. Major SST biases are located in high latitudes, especially the sea-ice covered regions.

By applying forced loss of sea ice to the hierarchy, we found that the reduction of the Atlantic meridional overturning circulation strongly influences the ocean heat uptake. Also, we found that the modulation of wind-driven Ekman flow does not damp the shift of intertropical convergence zone (ITCZ), which is opposite to what was proposed in past literature (T. Schneider, 2017; Green, J. Marshall, and Campin, 2019; Kang, 2020) and reveals the sensitivity of Ekman parameterization.

In chapter 3, we used the ocean hierarchy developed in chapter 2 to test the response of climate to a sudden quadrupling of CO_2 concentration. In POP2, we see the recovery of AMOC after 500 years, which greatly reduces the influence of AMOC so that the EMOM,

having the wind-driven ocean Ekman flow, is able to reproduce the enhanced rainfall and wind response over the tropical ocean. Separating the Ekman flow into the rotational and frictional components, we find that the ocean heat transport (OHT) due to the frictional Ekman flow is equal to or greater than the OHT due to the rotational Ekman flow over the Pacific and Atlantic Oceans. The difference between the response of EMOM and POP2 is sensitive to the vertical location of the oceanic vertical upwelling and the subsurface diffusive processes that influences the SST and thus the atmospheric circulation.

In chapter 2 and 3, we notice that the AMOC's response due to the changes in the freshwater forcing has profound modulation over the surface climate, mostly due to its heat transport in the transient climate. Our knowledge of AMOC's response in a changing climate remains primitive. In particular, although the community has established concrete understanding of AMOC's multiple equilibria and agree on the response of AMOC due to the changes of hydrological forcing, how the AMOC responds to the detail of forcing remains under-explored. Therefore, in chapter 4, we study the bifurcation of the overturning circulation using the zonally averaged two-slabs ocean model (ZATOM) adapted from Callies and Marotzke (2012), which we extend the buoyancy formulation into the temperature and salinity to apply the mixed boundary conditions.

In chapter 4, we find that the asymmetry of freshwater forcing modulates the existence of bifurcation in ZATOM, meaning this asymmetry parameter is a stability threshold (Weijer, Cheng, Drijfhout, et al., 2019). To understand the physical reason, we developed the extended two-box model in which we allow the two-box model to "feel" the zonal asymmetry of freshwater forcing. We are able to see that larger zonal asymmetry enhances the thermal mode and lower zonal asymmetry enhances the haline mode of the overturning circulation. We also derive a multi-linear relation of the strength of the overturning circulation with respect to the product of mean stratification and mean meridional buoyancy gradient, the east-west difference of the convective mixing, and the asymmetric freshwater forcing. The

zonal asymmetry of freshwater forcing and the linear relationship we developed can be used to understand the stability of AMOC in climate models.

5.2 Outlook

The ocean hierarchy in chapter 2 can be refined depending on the research topic. For example, the thickness of Ekman flow layer is arbitrarily chosen and is constant. There are ways to more objectively decide the thickness so that the Ekman transport response to surface forcing can be more realistic. Similar refinement also applies to the mixed-layer model because we still prescribe its temporal evolution. On the other hand, more processes can be added on top of EMOM such as the background geostrophic flows. A consistent problem across the hierarchy and past efforts is that simplified models cannot accurately reproduce a good sea-ice concentration and thickness, and typically the error is much larger in the southern hemisphere. It requires a deeper understanding of the air-sea interaction over the Southern Ocean so that a better hierarchy can be constructed.

In chapter 3, the fact that we are able to capture the feature of the pattern of the enhanced rainfall and SST over the tropics by including the Ekman flow suggests the possibility to develop a simple coupled model to explore the tropical air-sea interaction. There exist some possible frameworks that can be considered (Davey and Gill, 1987; B. Wang et al., 1995; Nilsson and Emanuel, 1999; Kang, Y. Shin, and Codron, 2018; Song et al., 2018). In particular, we should study the role of the frictional Ekman flow in the coupled dynamics which has received less attention.

In chapter 4, we developed the ZATOM that is currently limited to a single hemisphere. Therefore, to have more relevancy to the real world, its next step should be extending the ocean domain across the equator and connecting it with a re-entrant channel representing the

Southern Ocean. To have a representation of the Southern Ocean where the wind forcing is important, the model should also include momentum boundary condition. An even further step would be developing a simplified atmospheric model to couple with the ZATOM to understand the atmospheric feedback.

Bibliography

Stommel, H. (1959). Wind-drift near the equator. *Deep Sea Research (1953)*, *6*, 298–302.

Stommel, H. (1961). Thermohaline convection with two stable regimes of flow. *Tellus*, *13*(2), 224–230.

Bryan, K., & Cox, M. D. (1972). An approximate equation of state for numerical models of ocean circulation. *J. Phys. Oceanogr*, *2*(4), 510–514.

Keller, H. B. (1977). Numerical solution of bifurcation and nonlinear eigenvalue problems. *Application of bifurcation theory*, 359–384.

Niiler, P. (1977). One-dimensional models of the upper ocean. modelling and prediction of the upper layers of the ocean, eb kraus, ed. *Pergamon Press*, *143*, 172.

Paulson, C. A., & Simpson, J. J. (1977). Irradiance measurements in the upper ocean. *Journal of Physical Oceanography*, *7*(6), 952–956.

Leonard, B. P. (1979). A stable and accurate convective modelling procedure based on quadratic upstream interpolation. *Computer methods in applied mechanics and engineering*, *19*(1), 59–98.

Bryan, F. [Frank]. (1986). High-latitude salinity effects and interhemispheric thermohaline circulations. *Nature*, *323*(6086), 301–304.

Davey, M., & Gill, A. (1987). Experiments on tropical circulation with a simple moist model. *Quarterly Journal of the Royal Meteorological Society*, *113*(478), 1237–1269.

Gaspar, P. (1988). Modeling the seasonal cycle of the upper ocean. *Journal of Physical Oceanography*, *18*(2), 161–180.

Marotzke, J. [Jochem], Welander, P., & Willebrand, J. (1988). Instability and multiple steady states in a meridional-plane model of the thermohaline circulation. *Tellus A: Dynamic Meteorology and Oceanography*, *40*(2), 162–172.

Gent, P. R., & McWilliams, J. C. (1990). Isopycnal mixing in ocean circulation models. *Journal of Physical Oceanography*, *20*(1), 150–155.

Stocker, T. F., Mysak, L. A., & Wright, D. G. (1992). A zonally averaged, coupled ocean-atmosphere model for paleoclimate studies. *Journal of Climate*, *5*(8), 773–797.

Cessi, P. (1994). A simple box model of stochastically forced thermohaline flow. *Journal of physical oceanography*, *24*(9), 1911–1920.

Large, W. G., McWilliams, J. C., & Doney, S. C. (1994). Oceanic vertical mixing: A review and a model with a nonlocal boundary layer parameterization. *Reviews of Geophysics*, *32*(4), 363–403.

Alexander, M. A., & Deser, C. [Clara]. (1995). A mechanism for the recurrence of wintertime midlatitude sst anomalies. *Journal of physical oceanography*, *25*(1), 122–137.

Wang, B., Li, T., & Chang, P. (1995). An intermediate model of the tropical pacific ocean. *Journal of physical oceanography*, *25*(7), 1599–1616.

Vellinga, M. (1996). Instability of two-dimensional themohaline circulation. *Journal of physical oceanography*, *26*(3), 305–319.

Dijkstra, H. A., & MOLEMAKER, M. J. (1997). Symmetry breaking and overturning oscillations in thermohaline-driven flows. *Journal of Fluid Mechanics*, *331*, 169–198.

Marotzke, J. [Jochem]. (1997). Boundary mixing and the dynamics of three-dimensional thermohaline circulations. *Journal of Physical Oceanography*, *27*(8), 1713–1728.

Lee, T., & Marotzke, J. [Jochem]. (1998). Seasonal cycles of meridional overturning and heat transport of the indian ocean. *Journal of Physical Oceanography*, *28*(5), 923–943.

Alexander, M. A., Deser, C. [Clara], & Timlin, M. S. (1999). The reemergence of sst anomalies in the north pacific ocean. *Journal of climate*, *12*(8), 2419–2433.

David, B., Hannay, C., Holland, M., & Neale, R. (1999). *Slab ocean model forcing*. http://www.cesm.ucar.edu/models/cesm1.2/data8/doc/SOM.pdf

Magnusdottir, G., & Saravannan, R. (1999). The response of atmospheric heat transport to zonally-averaged sst trends. *Tellus A: Dynamic Meteorology and Oceanography*, *51*(5), 815–832.

Nilsson, J., & Emanuel, K. (1999). Equilibrium atmospheres of a two-column radiative-convective model. *Quarterly Journal of the Royal Meteorological Society*, *125*(558), 2239–2264.

Alexander, M. A., Scott, J. D., & Deser, C. [Clara]. (2000). Processes that influence sea surface temperature and ocean mixed layer depth variability in a coupled model. *Journal of Geophysical Research: Oceans*, *105*(C7), 16823–16842.

Klinger, B. A., & Marotzke, J. (2000). Meridional heat transport by the subtropical cell. *Journal of physical oceanography*, *30*(4), 696–705.

Miller, A. J., & Schneider, N. (2000). Interdecadal climate regime dynamics in the north pacific ocean: Theories, observations and ecosystem impacts. *Progress in Oceanography*, *47*(2-4), 355–379.

Dijkstra, H. A., Oksuzoglu, H., Wubs, F. W., & Botta, E. F. (2001). A fully implicit model of the three-dimensional thermohaline ocean circulation. *Journal of Computational Physics*, *173*(2), 685–715.

Held, I. M. (2001). The partitioning of the poleward energy transport between the tropical ocean and atmosphere. *Journal of the atmospheric sciences*, *58*(8), 943–948.

Jayne, S. R. [Steven R], & Marotzke, J. [Jochem]. (2001). The dynamics of ocean heat transport variability. *Reviews of Geophysics*, *39*(3), 385–411.

Alexander, M. A., Bladé, I., Newman, M., Lanzante, J. R., Lau, N.-C., & Scott, J. D. (2002). The atmospheric bridge: The influence of enso teleconnections on air–sea interaction over the global oceans. *Journal of climate*, *15*(16), 2205–2231.

Claussen, M., Mysak, L., Weaver, A., Crucifix, M., Fichefet, T., Loutre, M.-F., Weber, S., Alcamo, J., Alexeev, V., Berger, A. et al. (2002). Earth system models of intermediate complexity: Closing the gap in the spectrum of climate system models. *Climate dynamics*, *18*(7), 579–586.

Dommenget, D., & Latif, M. (2002). Analysis of observed and simulated sst spectra in the midlatitudes. *Climate Dynamics*, *19*(3), 277–288.

Vellinga, M., & Wood, R. A. (2002). Global climatic impacts of a collapse of the atlantic thermohaline circulation. *Climatic change*, *54*(3), 251–267.

Chatfield, C. (2003). *The analysis of time series: An introduction*. Chapman; hall/CRC.

Dijkstra, H. A., & Weijer, W. (2003). Stability of the global ocean circulation: The connection of equilibria within a hierarchy of models. *Journal of Marine Research*, *61*(6), 725–743.

Neelin, J., Chou, C., & Su, H. (2003). Tropical drought regions in global warming and el niño teleconnections. *Geophysical Research Letters*, *30*(24).

Chiang, J. C., & Bitz, C. M. (2005). Influence of high latitude ice cover on the marine intertropical convergence zone. *Climate Dynamics*, *25*(5), 477–496.

Dijkstra, H. A., & Weijer, W. (2005). Stability of the global ocean circulation: Basic bifurcation diagrams. *Journal of physical oceanography*, *35*(6), 933–948.

Haarsma, R. J., Campos, E. J., Hazeleger, W., Severijns, C., Piola, A. R., & Molteni, F. (2005). Dominant modes of variability in the south atlantic: A study with a hierarchy of ocean–atmosphere models. *Journal of climate*, *18*(11), 1719–1735.

Held, I. M. (2005). The gap between simulation and understanding in climate modeling. *Bulletin of the American Meteorological Society*, *86*(11), 1609–1614.

Rahmstorf, S., Crucifix, M., Ganopolski, A., Goosse, H., Kamenkovich, I., Knutti, R., Lohmann, G., Marsh, R., Mysak, L. A., Wang, Z. [Zhaomin] et al. (2005). Thermohaline circulation hysteresis: A model intercomparison. *Geophysical Research Letters*, *32*(23).

Schneider, N., & Cornuelle, B. D. (2005). The forcing of the pacific decadal oscillation. *Journal of Climate*, *18*(21), 4355–4373.

Kiehl, J. T., Shields, C. A., Hack, J. J., & Collins, W. D. (2006). The climate sensitivity of the community climate system model version 3 (ccsm3). *Journal of Climate*, *19*(11), 2584–2596.

Cassou, C., Deser, C., & Alexander, M. A. (2007). Investigating the impact of reemerging sea surface temperature anomalies on the winter atmospheric circulation over the north atlantic. *Journal of climate*, *20*(14), 3510–3526.

Hirschi, J., & Marotzke, J. (2007). Reconstructing the meridional overturning circulation from boundary densities and the zonal wind stress. *Journal of Physical Oceanography*, *37*(3), 743–763.

Primeau, F. W., & Newman, D. (2007). Bifurcation structure of a wind-driven shallow water model with layer-outcropping. *Ocean Modelling*, *16*(3-4), 250–263.

Vecchi, G. A., & Soden, B. J. (2007). Global warming and the weakening of the tropical circulation. *Journal of Climate*, *20*(17), 4316–4340.

Alexander, M. A., & Scott, J. D. (2008). The role of ekman ocean heat transport in the northern hemisphere response to enso. *Journal of climate*, *21*(21), 5688–5707.

Kang, S. M., Held, I. M., Frierson, D. M., & Zhao, M. (2008). The response of the itcz to extratropical thermal forcing: Idealized slab-ocean experiments with a gcm. *Journal of Climate*, *21*(14), 3521–3532.

Cessi, P., & Wolfe, C. L. (2009). Eddy-driven buoyancy gradients on eastern boundaries and their role in the thermocline. *Journal of physical oceanography*, *39*(7), 1595–1614.

Cronin, M. F., & Kessler, W. S. (2009). Near-surface shear flow in the tropical pacific cold tongue front. *Journal of Physical Oceanography*, *39*(5), 1200–1215.

Seydel, R. (2009). *Practical bifurcation and stability analysis* (Vol. 5). Springer Science & Business Media.

Smith, R. S., & Gregory, J. M. (2009). A study of the sensitivity of ocean overturning circulation and climate to freshwater input in different regions of the north atlantic. *Geophysical research letters*, *36*(15).

Hunke, E. C., Lipscomb, W. H., Turner, A. K., Jeffery, N., & Elliott, S. (2010). Cice: The los alamos sea ice model documentation and software user's manual version 4.1 la-cc-06-012. *T-3 Fluid Dynamics Group, Los Alamos National Laboratory*, *675*, 500.

Roche, D. M., Wiersma, A. P., & Renssen, H. (2010). A systematic study of the impact of freshwater pulses with respect to different geographical locations. *Climate Dynamics*, *34*(7), 997–1013.

Smith, R., Jones, P., Briegleb, B., Bryan, F., Danabasoglu, G., Dennis, J., Dukowicz, J., Eden, C., Fox-Kemper, B., Gent, P. et al. (2010). The parallel ocean program (pop) reference manual: Ocean component of the community climate system model (ccsm) and community earth system model (cesm). *LAUR-01853*, *141*, 1–140.

Xie, S.-P., Deser, C., Vecchi, G. A., Ma, J., Teng, H., & Wittenberg, A. T. (2010). Global warming pattern formation: Sea surface temperature and rainfall. *Journal of Climate*, *23*(4), 966–986.

den Toom, M., Dijkstra, H. A., & Wubs, F. W. (2011). Spurious multiple equilibria introduced by convective adjustment. *Ocean Modelling*, *38*(1-2), 126–137.

Gent, P. R., Danabasoglu, G. [Gokhan], Donner, L. J., Holland, M. M., Hunke, E. C., Jayne, S. R. [Steve R], Lawrence, D. M., Neale, R. B., Rasch, P. J., Vertenstein, M. et al. (2011). The community climate system model version 4. *Journal of climate*, *24*(19), 4973–4991.

Kwon, Y.-O., Deser, C., & Cassou, C. (2011). Coupled atmosphere–mixed layer ocean response to ocean heat flux convergence along the kuroshio current extension. *Climate dynamics*, *36*(11-12), 2295–2312.

Lawrence, D. M., Oleson, K. W., Flanner, M. G., Thornton, P. E., Swenson, S. C., Lawrence, P. J., Zeng, X., Yang, Z.-L., Levis, S., Sakaguchi, K. et al. (2011). Parameterization

improvements and functional and structural advances in version 4 of the community land model. *Journal of Advances in Modeling Earth Systems*, *3*(1).

Rayner, D., Hirschi, J. J.-M., Kanzow, T., Johns, W. E., Wright, P. G., Frajka-Williams, E., Bryden, H. L., Meinen, C. S., Baringer, M. O., Marotzke, J. [Jochem] et al. (2011). Monitoring the atlantic meridional overturning circulation. *Deep Sea Research Part II: Topical Studies in Oceanography*, *58*(17-18), 1744–1753.

Sévellec, F., & Fedorov, A. V. (2011). Stability of the atlantic meridional overturning circulation and stratification in a zonally averaged ocean model: Effects of freshwater flux, southern ocean winds, and diapycnal diffusion. *Deep Sea Research Part II: Topical Studies in Oceanography*, *58*(17-18), 1927–1943.

Shin, S.-I., & Sardeshmukh, P. D. (2011). Critical influence of the pattern of tropical ocean warming on remote climate trends. *Climate Dynamics*, *36*(7), 1577–1591.

Callies, J., & Marotzke, J. (2012). A simple and self-consistent geostrophic-force-balance model of the thermohaline circulation with boundary mixing. *Ocean Science*, *8*(1), 49–63.

Codron, F. (2012). Ekman heat transport for slab oceans. *Climate Dynamics*, *38*(1-2), 379–389.

Danabasoglu, G. [Gokhan], Bates, S. C., Briegleb, B. P., Jayne, S. R., Jochum, M., Large, W. G., Peacock, S., & Yeager, S. G. (2012). The ccsm4 ocean component. *Journal of Climate*, *25*(5), 1361–1389.

Li, G., & Xie, S.-P. (2012). Origins of tropical-wide sst biases in cmip multi-model ensembles. *Geophysical research letters*, *39*(22).

Nikurashin, M., & Vallis, G. (2012). A theory of the interhemispheric meridional overturning circulation and associated stratification. *Journal of Physical Oceanography*, *42*(10), 1652–1667.

Huang, P., Xie, S.-P., Hu, K., Huang, G., & Huang, R. (2013). Patterns of the seasonal response of tropical rainfall to global warming. *Nature Geoscience*, *6*(5), 357–361.

Hurrell, J. W., Holland, M. M., Gent, P. R., Ghan, S., Kay, J. E., Kushner, P. J., Lamarque, J.-F., Large, W. G., Lawrence, D., Lindsay, K. et al. (2013). The community earth system model: A framework for collaborative research. *Bulletin of the American Meteorological Society*, *94*(9), 1339–1360.

Ma, J., & Xie, S.-P. (2013). Regional patterns of sea surface temperature change: A source of uncertainty in future projections of precipitation and atmospheric circulation. *Journal of climate*, *26*(8), 2482–2501.

Neale, R. B., Richter, J., Park, S., Lauritzen, P. H., Vavrus, S. J., Rasch, P. J., & Zhang, M. (2013). The mean climate of the community atmosphere model (cam4) in forced sst and fully coupled experiments. *Journal of Climate*, *26*(14), 5150–5168.

Deusebio, E., Brethouwer, G., Schlatter, P., & Lindborg, E. (2014). A numerical study of the unstratified and stratified ekman layer. *Journal of fluid mechanics*, *755*, 672–704.

Donohoe, A., Frierson, D. M., & Battisti, D. S. (2014). The effect of ocean mixed layer depth on climate in slab ocean aquaplanet experiments. *Climate dynamics*, *43*(3-4), 1041–1055.

Kostov, Y., Armour, K. C., & Marshall, J. (2014). Impact of the atlantic meridional overturning circulation on ocean heat storage and transient climate change. *Geophysical Research Letters*, *41*(6), 2108–2116.

Marshall, D. P., & Zanna, L. (2014). A conceptual model of ocean heat uptake under climate change. *Journal of Climate*, *27*(22), 8444–8465.

Rose, B. E., Armour, K. C., Battisti, D. S., Feldl, N., & Koll, D. D. (2014). The dependence of transient climate sensitivity and radiative feedbacks on the spatial pattern of ocean heat uptake. *Geophysical Research Letters*, *41*(3), 1071–1078.

Schneider, T., Bischoff, T., & Haug, G. H. (2014). Migrations and dynamics of the intertropical convergence zone. *Nature*, *513*(7516), 45–53.

Trenberth, K. E., Fasullo, J. T., & Balmaseda, M. A. (2014). Earth's energy imbalance. *Journal of Climate*, *27*(9), 3129–3144.

Bony, S., Stevens, B., Frierson, D. M., Jakob, C., Kageyama, M., Pincus, R., Shepherd, T. G., Sherwood, S. C., Siebesma, A. P., Sobel, A. H. et al. (2015). Clouds, circulation and climate sensitivity. *Nature Geoscience*, *8*(4), 261–268.

Hirons, L., Klingaman, N., & Woolnough, S. (2015). Metum-goml: A near-globally coupled atmosphere–ocean-mixed-layer model. *Geoscientific Model Development*, *8*, 363–379.

Huang, P., & Ying, J. (2015). A multimodel ensemble pattern regression method to correct the tropical pacific sst change patterns under global warming. *Journal of Climate*, *28*(12), 4706–4723.

Jackson, L., Kahana, R., Graham, T., Ringer, M., Woollings, T., Mecking, J., & Wood, R. (2015). Global and european climate impacts of a slowdown of the amoc in a high resolution gcm. *Climate dynamics*, *45*(11), 3299–3316.

Lau, W. K., & Kim, K.-M. (2015). Robust hadley circulation changes and increasing global dryness due to co2 warming from cmip5 model projections. *Proceedings of the National Academy of Sciences*, *112*(12), 3630–3635.

Serreze, M. C., & Stroeve, J. (2015). Arctic sea ice trends, variability and implications for seasonal ice forecasting. *Philosophical Transactions of the Royal Society A: Mathematical, Physical and Engineering Sciences*, *373*(2045), 20140159.

Byrne, M. P., & Schneider, T. (2016a). Energetic constraints on the width of the intertropical convergence zone. *Journal of Climate*, *29*(13), 4709–4721.

Byrne, M. P., & Schneider, T. (2016b). Narrowing of the itcz in a warming climate: Physical mechanisms. *Geophysical Research Letters*, *43*(21), 11–350.

Griffies, S. M., Danabasoglu, G. [Gokhan], Durack, P. J., Adcroft, A. J., Balaji, V., Böning, C. W., Chassignet, E. P., Curchitser, E., Deshayes, J., Drange, H. et al. (2016). Omip contribution to cmip6: Experimental and diagnostic protocol for the physical component of the ocean model intercomparison project. *Geoscientific Model Development*, *9*(9), 3231–3296.

Long, S.-M., Xie, S.-P., & Liu, W. (2016). Uncertainty in tropical rainfall projections: Atmospheric circulation effect and the ocean coupling. *Journal of Climate*, *29*(7), 2671–2687.

Newman, M., Alexander, M. A., Ault, T. R., Cobb, K. M., Deser, C. [Clara], Di Lorenzo, E., Mantua, N. J., Miller, A. J., Minobe, S., Nakamura, H. et al. (2016). The pacific decadal oscillation, revisited. *Journal of Climate*, *29*(12), 4399–4427.

Rose, B. E., & Rayborn, L. (2016). The effects of ocean heat uptake on transient climate sensitivity. *Current climate change reports*, *2*(4), 190–201.

Sévellec, F., & Huck, T. (2016). Geostrophic closure of the zonally averaged atlantic meridional overturning circulation. *Journal of Physical Oceanography*, *46*(3), 895–917.

Tomas, R. A., Deser, C., & Sun, L. (2016). The role of ocean heat transport in the global climate response to projected arctic sea ice loss. *Journal of Climate*, *29*(19), 6841–6859.

Trenberth, K. E., Fasullo, J. T., Von Schuckmann, K. [Karina], & Cheng, L. (2016). Insights into earth's energy imbalance from multiple sources. *Journal of Climate*, *29*(20), 7495–7505.

Von Schuckmann, K., Palmer, M., Trenberth, K. E., Cazenave, A., Chambers, D., Champollion, N., Hansen, J., Josey, S., Loeb, N., Mathieu, P.-P. et al. (2016). An imperative to monitor earth's energy imbalance. *Nature Climate Change*, *6*(2), 138–144.

Green, B., & Marshall, J. (2017). Coupling of trade winds with ocean circulation damps itcz shifts. *Journal of Climate*, *30*(12), 4395–4411.

Jeevanjee, N., Hassanzadeh, P., Hill, S., & Sheshadri, A. (2017). A perspective on climate model hierarchies. *Journal of Advances in Modeling Earth Systems*, *9*(4), 1760–1771.

Schneider, T. (2017). Feedback of atmosphere-ocean coupling on shifts of the intertropical convergence zone. *Geophysical Research Letters*, *44*(22), 11–644.

Trenberth, K. E., & Fasullo, J. T. (2017). Atlantic meridional heat transports computed from balancing earth's energy locally. *Geophysical Research Letters*, *44*(4), 1919–1927.

Wang, Y., & McPhaden, M. J. (2017). Seasonal cycle of cross-equatorial flow in the central i ndian o cean. *Journal of Geophysical Research: Oceans*, *122*(5), 3817–3827.

Blackport, R., & Kushner, P. J. (2018). The role of extratropical ocean warming in the coupled climate response to arctic sea ice loss. *Journal of Climate*, *31*(22), 9193–9206.

Byrne, M. P., Pendergrass, A. G., Rapp, A. D., & Wodzicki, K. R. (2018). Response of the intertropical convergence zone to climate change: Location, width, and strength. *Current climate change reports*, *4*(4), 355–370.

Chemke, R., & Polvani, L. (2018). Ocean circulation reduces the hadley cell response to increased greenhouse gases. *Geophysical Research Letters*, *45*(17), 9197–9205.

Cox, P. M., Huntingford, C., & Williamson, M. S. (2018). Emergent constraint on equilibrium climate sensitivity from global temperature variability. *Nature*, *553*(7688), 319–322.

Kang, S. M., Shin, Y., & Codron, F. (2018). The partitioning of poleward energy transport response between the atmosphere and ekman flux to prescribed surface forcing in a simplified gcm. *Geoscience Letters*, *5*(1), 22.

Kang, S. M., Shin, Y., & Xie, S.-P. (2018). Extratropical forcing and tropical rainfall distribution: Energetics framework and ocean ekman advection. *npj Climate and Atmospheric Science*, *1*(1), 1–10.

Lewis, N., & Curry, J. (2018). The impact of recent forcing and ocean heat uptake data on estimates of climate sensitivity. *Journal of Climate*, *31*(15), 6051–6071.

Rind, D., Schmidt, G. A., Jonas, J., Miller, R., Nazarenko, L., Kelley, M., & Romanski, J. (2018). Multicentury instability of the atlantic meridional circulation in rapid warming simulations with giss modele2. *Journal of Geophysical Research: Atmospheres*, *123*(12), 6331–6355.

Screen, J. A., Deser, C., Smith, D. M., Zhang, X., Blackport, R., Kushner, P. J., Oudar, T., McCusker, K. E., & Sun, L. (2018). Consistency and discrepancy in the atmospheric response to arctic sea-ice loss across climate models. *Nature Geoscience*, *11*(3), 155.

Shi, J.-R., Xie, S.-P., & Talley, L. D. (2018). Evolving relative importance of the southern ocean and north atlantic in anthropogenic ocean heat uptake. *Journal of Climate*, *31*(18), 7459–7479.

Song, X., Chen, D., Tang, Y., & Liu, T. (2018). An intermediate coupled model for the tropical ocean-atmosphere system. *Science China Earth Sciences*, *61*(12), 1859–1874.

Sun, L., Alexander, M., & Deser, C. (2018). Evolution of the global coupled climate response to arctic sea ice loss during 1990–2090 and its contribution to climate change. *Journal of Climate*, *31*(19), 7823–7843.

Vallis, G. K., Colyer, G., Geen, R., Gerber, E., Jucker, M., Maher, P., Paterson, A., Pietschnig, M., Penn, J., & Thomson, S. I. (2018). Isca, v1. 0: A framework for the global modelling of the atmospheres of earth and other planets at varying levels of complexity. *Geoscientific Model Development*, *11*(3), 843–859.

Van Roekel, L., Adcroft, A. J., Danabasoglu, G., Griffies, S. M., Kauffman, B., Large, W., Levy, M., Reichl, B. G., Ringler, T., & Schmidt, M. (2018). The kpp boundary layer scheme for the ocean: Revisiting its formulation and benchmarking one-dimensional simulations relative to les. *Journal of Advances in Modeling Earth Systems*, *10*(11), 2647–2685.

Green, B., Marshall, J., & Campin, J.-M. (2019). The 'sticky'itcz: Ocean-moderated itcz shifts. *Climate dynamics*, *53*(1-2), 1–19.

Johnson, H. L., Cessi, P., Marshall, D. P., Schloesser, F., & Spall, M. A. (2019). Recent contributions of theory to our understanding of the atlantic meridional overturning circulation. *Journal of Geophysical Research: Oceans*, *124*(8), 5376–5399.

Lenton, T. M., Rockström, J., Gaffney, O., Rahmstorf, S., Richardson, K., Steffen, W., & Schellnhuber, H. J. (2019). Climate tipping points—too risky to bet against.

Maher, P., Gerber, E. P., Medeiros, B., Merlis, T. M., Sherwood, S., Sheshadri, A., Sobel, A. H., Vallis, G. K., Voigt, A., & Zurita-Gotor, P. (2019). Model hierarchies for understanding atmospheric circulation. *Reviews of Geophysics*, *57*(2), 250–280.

Smith, D. M. [Doug M], Screen, J. A., Deser, C. [Clara], Cohen, J., Fyfe, J. C., Garcıa-Serrano, J. [Javier], Jung, T., Kattsov, V., Matei, D., Msadek, R. et al. (2019). The polar amplification model intercomparison project (pamip) contribution to cmip6: Investigating the causes and consequences of polar amplification. *Geoscientific Model Development*, *12*(3), 1139–1164.

Thackeray, C. W., & Hall, A. (2019). An emergent constraint on future arctic sea-ice albedo feedback. *Nature Climate Change*, *9*(12), 972–978.

Wang, Z. [Zaiyu], Schneider, E. K., & Burls, N. J. (2019). The sensitivity of climatological sst to slab ocean model thickness. *Climate Dynamics*, *53*(9), 5709–5723.

Weijer, W., Cheng, W., Drijfhout, S. S., Fedorov, A. V., Hu, A., Jackson, L. C., Liu, W., McDonagh, E., Mecking, J., & Zhang, J. (2019). Stability of the atlantic meridional overturning circulation: A review and synthesis. *Journal of Geophysical Research: Oceans*, *124*(8), 5336–5375.

Yu, S., & Pritchard, M. S. (2019). A strong role for the amoc in partitioning global energy transport and shifting itcz position in response to latitudinally discrete solar forcing in cesm1. 2. *Journal of Climate*, *32*(8), 2207–2226.

Zhang, R., Sutton, R., Danabasoglu, G., Kwon, Y.-O., Marsh, R., Yeager, S. G., Amrhein, D. E., & Little, C. M. (2019). A review of the role of the atlantic meridional overturning circulation in atlantic multidecadal variability and associated climate impacts. *Reviews of Geophysics*, *57*(2), 316–375.

Zhou, W., Xie, S.-P., & Yang, D. (2019). Enhanced equatorial warming causes deep-tropical contraction and subtropical monsoon shift. *Nature Climate Change*, *9*(11), 834–839.

Afargan-Gerstman, H., & Adam, O. (2020). Nonlinear damping of itcz migrations due to ekman ocean energy transport. *Geophysical Research Letters*, *47*(5), e2019GL086445.

Andersen, J., Andreassen, L. M., Baker, E. H., Ballinger, T. J., Berner, L. T., Bernhard, G. H., Bhatt, U. S., Bjerke, J. W., Box, J. E., Britt, L. et al. (2020). The arctic. *Bulletin of the American Meteorological Society*, *101*(8), S239–S286.

Dong, Y., Armour, K. C., Zelinka, M. D., Proistosescu, C., Battisti, D. S., Zhou, C., & Andrews, T. (2020). Intermodel spread in the pattern effect and its contribution to climate sensitivity in cmip5 and cmip6 models. *Journal of Climate*, *33*(18), 7755–7775.

England, M. R., Polvani, L. M., Sun, L., & Deser, C. (2020). Tropical climate responses to projected arctic and antarctic sea-ice loss. *Nature Geoscience*, *13*(4), 275–281.

Fang, S.-W., & Yu, J.-Y. (2020). A control of enso transition complexity by tropical pacific mean ssts through tropical-subtropical interaction. *Geophysical Research Letters*, *47*(12), e2020GL087933.

Hu, A., Van Roekel, L., Weijer, W., Garuba, O. A., Cheng, W., & Nadiga, B. T. (2020). Role of amoc in transient climate response to greenhouse gas forcing in two coupled models. *Journal of Climate*, *33*(14), 5845–5859.

Kang, S. M. (2020). Extratropical influence on the tropical rainfall distribution. *Current Climate Change Reports*, *6*(1), 24–36.

Meehl, G. A., Senior, C. A., Eyring, V., Flato, G., Lamarque, J.-F., Stouffer, R. J., Taylor, K. E., & Schlund, M. (2020). Context for interpreting equilibrium climate sensitivity and transient climate response from the cmip6 earth system models. *Science Advances*, *6*(26), eaba1981.

Sun, L., Deser, C. [Clara], Tomas, R. A., & Alexander, M. (2020). Global coupled climate response to polar sea ice loss: Evaluating the effectiveness of different ice-constraining approaches. *Geophysical Research Letters*, *47*(3), e2019GL085788.

Tian, B., & Dong, X. (2020). The double-itcz bias in cmip3, cmip5, and cmip6 models based on annual mean precipitation. *Geophysical Research Letters*, *47*(8), e2020GL087232.

Weijer, W., Cheng, W., Garuba, O. A., Hu, A., & Nadiga, B. (2020). Cmip6 models predict significant 21st century decline of the atlantic meridional overturning circulation. *Geophysical Research Letters*, *47*(12), e2019GL086075.

Xie, S.-P. (2020). Ocean warming pattern effect on global and regional climate change. *AGU advances*, *1*(1), e2019AV000130.

Zelinka, M. D., Myers, T. A., McCoy, D. T., Po-Chedley, S., Caldwell, P. M., Ceppi, P., Klein, S. A., & Taylor, K. E. (2020). Causes of higher climate sensitivity in cmip6 models. *Geophysical Research Letters*, *47*(1), e2019GL085782.

Adam, O. (2021). Dynamic and energetic constraints on the modality and position of the intertropical convergence zone in an aquaplanet. *Journal of Climate*, *34*(2), 527–543.

Fox-Kemper, B. [B.], Hewitt, H., Xiao, C., Aalgeirsdóttir, G., Drijfhout, S., Edwards, T., Golledge, N., Hemer, M., Kopp, R., Krinner, G., Mix, A., Notz, D., Nowicki, S., Nurhati, I., Ruiz, L., Sallée, J.-B., Slangen, A., & Yu, Y. (2021). Ocean, cryosphere and sea level change. In V. Masson-Delmotte, P. Zhai, A. Pirani, S. Connors, C. Péan, S. Berger, N. Caud, Y. Chen, L. Goldfarb, M. Gomis, M. Huang, K. Leitzell, E. Lonnoy, J. Matthews, T. Maycock, T. Waterfield, O. Yelekçi, R. Yu, & B. Zhou (Eds.), *Climate change 2021: The physical science basis. contribution of working group i to the sixth assessment report of the intergovernmental panel on climate change* (pp. 1211–1362). Cambridge University Press. https://doi.org/10.1017/9781009157896.011

Mamalakis, A., Randerson, J. T., Yu, J.-Y., Pritchard, M. S., Magnusdottir, G., Smyth, P., Levine, P. A., Yu, S., & Foufoula-Georgiou, E. (2021). Zonally contrasting shifts of the tropical rain belt in response to climate change. *Nature climate change*, *11*(2), 143–151.

Myers, T. A., Scott, R. C., Zelinka, M. D., Klein, S. A., Norris, J. R., & Caldwell, P. M. (2021). Observational constraints on low cloud feedback reduce uncertainty of climate sensitivity. *Nature Climate Change*, *11*(6), 501–507.

Nummelin, A., Busecke, J. J., Haine, T. W., & Abernathey, R. P. (2021). Diagnosing the scale-and space-dependent horizontal eddy diffusivity at the global surface ocean. *Journal of Physical Oceanography*, *51*(2), 279–297.

Yun, K.-S., Lee, J.-Y., Timmermann, A., Stein, K., Stuecker, M. F., Fyfe, J. C., & Chung, E.-S. (2021). Increasing enso–rainfall variability due to changes in future tropical temperature–rainfall relationship. *Communications Earth & Environment*, *2*(1), 1–7.

Good, P., Boers, N., Boulton, C. A., Lowe, J. A., & Richter, I. (2022). How might a collapse in the atlantic meridional overturning circulation affect rainfall over tropical south america? *Climate Resilience and Sustainability*, *1*(1), e26.

Hsu, T.-Y., Primeau, F., & Magnusdottir, G. (2022). A hierarchy of global ocean models coupled to cesm1. *Journal of Advances in Modeling Earth Systems*, e2021MS002979.

Kim, S.-K., Kim, H.-J., Dijkstra, H. A., & An, S.-I. (2022). Slow and soft passage through tipping point of the atlantic meridional overturning circulation in a changing climate. *npj Climate and Atmospheric Science*, *5*(1), 1–10.

Smith, D. M. [D. M.], Eade, R., M., A., H., A., A., C., S., C., C., D., J., D. N., J., G.-S., S., G. L., B., H., L., H., T., J., J., K., X., L., G., M., E., M., D., M., M., M., ... others, W. A. (2022). Robust but weak winter atmospheric circulation response to future arctic sea ice loss. , acceptedthe double-itcz bias in cmip3, cmip5, and cmip6 models based on annual mean precipitation. *Nature Communications*.

Smith, D. M. [Doug M], Eade, R., Andrews, M., Ayres, H., Clark, A., Chripko, S., Deser, C., Dunstone, N., Garcıa-Serrano, J., Gastineau, G. et al. (2022). Robust but weak winter atmospheric circulation response to future arctic sea ice loss. *Nature communications*, *13*(1), 1–15.